UNIVERSITA' DEGLI STUDI DI PARMA

Dottorato di Ricerca in Scienze della Terra

XXIX Ciclo

Ab initio calculations of Raman and IR spectra of orthoenstatite and forsterite:

lattice dynamics and modelling for planetary remote sensing

Coordinatore:
Chiar.mo Prof. Fulvio Celico

Tutor:
Chiar.mo Prof. Mario Tribaudino
Chiar.mo Prof. Mauro Prencipe

Dottorando: Claudia Stangarone

Contents

List of figures

List of tables

INTRODUCTION

The main subject of this thesis are atom vibrations in the crystal lattice. Atomic vibrations can be explained also in terms of lattice dynamics, which is the study of those vibrations as harmonic travelling waves and may be calculated within the framework of quasi-harmonic approximation. (Dove 2011). Lattice dynamics allow to understand some important phenomena: the interaction of the electromagnetic radiation with matter is probably the most important example of the role of lattice dynamics. In fact, the absorption of certain frequencies in the infrared spectral region is directly due to the existence of specific atom vibrations. The spectral region greater than 8μm up to 12μm can be ascribed as thermal infrared (TIR) region; within this range, spectral features of silicate minerals, arise from the fundamental vibrational modes of the material (Salisburry 1987).

Focusing on a silicate TIR spectrum, the primary spectral absorptions (Reststrahlen bands) are due to the stretching and bending motions of the silicon–oxygen anions. Additional absorption features result from metal–oxygen and lattice vibrations. Spectral features such as shapes, maxima or minima, intensities are directly dependent on the relative masses, radii, bond strengths and therefore generally speaking, on all the structural arrangements in a crystal lattice. It follows that, since all minerals, by definition, have unique structures and/or compositions, virtually every mineral has a different suite of vibrational absorption characteristics and thus a unique spectrum in the thermal infrared (Hamilton 2010). Several spectroscopic techniques are capable of measuring the fundamental vibrational modes of minerals, including: transmission, reflection, emission, attenuated total reflection (ATR), and Raman.

The present study will focus on just two techniques: Raman spectroscopy and emission spectroscopy, applied to the investigation of two well-known mineral families: olivine and orthopyroxenes. The motivations and applications of TIR spectral studies, and especially on these two minerals, are wide-ranging, covering fields from astronomy to mantle geophysics; a wide variety of measurement techniques and samples analysis can be found in literature (some of these are listed

and discussed in Chapter 1), so exhaustive that could fill a book. However, in this study we present some innovations in the experimental approach to the subject: the calculation and the modelling of Raman and emission spectra at room and at high temperature of those minerals, by means of *ab initio* (quantum mechanical) calculations. But let us take a step backwards and see the motivations of this approach.

Nowadays a wide variety of properties of minerals can be calculated almost automatically, overcoming the limits of empirical investigations. One of the great achievements in modern sciences has been the development of methods to compute the electron density and properties of matter using quantum mechanics, supported by the decrease of computational cost and the increase of availability of suitable computer codes. (Dovesi et al., 2014). Among the computational methods, *ab initio* calculations are now largely used, which allow the reproduction of properties of crystals, at any pressure and temperature condition, requiring the least possible amount of *a priori* empirical information (which, in turn, is related to the complexity of the systems being investigated, and to the available computational resources). In general, for a successful simulation, it is mandatory no more than prior information such as the chemical composition of the material and an approximated starting structure of the crystal (symmetry; cell parameters; atomic fractional coordinates). Moreover, as it will be shown, the employment of hybrid HF/DFT Hamiltonians to solve the *electron problem* is found to be the best and accurate way to simulate a vibrational pattern, leading to an almost straightforward comparisons with experimental measurements (Zicovich-Wilson et al. 2004; Demichelis et al. 2009; Ungureanu et al. 2010, 2012; De La Pierre et al. 2011; Prencipe et al. 2012; Prencipe 2012; Scanavino et al. 2012, Prencipe et al., 2014).

Therefore, by joining *ab initio* methods and experimental measurements, this thesis aims to show an innovative and rather *user-friendly* employment of quantum mechanics, comparing calculated data with experimental spectroscopic measurements, in order to interpret the results (signals assignment and linking of spectral features to the crystal structures) and to develop reliable applications of the methods.

Two different kinds of case studies will be shown, one focused on Raman spectroscopy and the other one concerning the modelling of emissivity spectra at high temperature.

Before explain with more details the two case of studies, few remarks must be done. Although the calculated/experimental approach has been already dealt for both minerals (literature in Chapter 1), the general goal within the field of Raman spectroscopy is to extend the results to a more

fundamental level linking the calculated results to investigate the structure. The modelling of MID-IR spectra at high temperature is instead, to the author knowledge, a completely new modelling approach with *ab initio* methods and here tested and shown for the first time. In details:

1. Raman mode assignment by quantum mechanical calculation (Chapter 3): two examples (one on olivine and one on orthoenstatite) of Raman mode assignment in experimental spectra driven by the use of the calculated frequencies, which means simulations of Raman spectra compared to the available literature data and to experimental Raman spectra taken at room temperature. The method allows a reliable symmetry assignment of Raman experimentally observed signals. Moreover, isotopic shifts can be easily simulated by changing the mass of the nuclei for each of the symmetry independent species within the unit cell; this allows for the estimation of the contributions of each element to the overall vibration. The aim is to relate the major experimental peaks, not only to specific structural features but also to link them to the Raman shifts observed due to variations of both temperature and composition.
2. Modelling of high temperature TIR spectra for Mercury remote sensing (Chapter 4): is the modelling of the emissivity spectra from low to high temperature, joined with experimental emissivity measurements, in order to simulate the surface environment of the Planet Mercury. As said before, the spectral signatures of minerals are intimately related to the crystal structure (Christiansen et al 2000, Koike 2003); therefore, they could represent a remote sensing model to determine the surface composition of planetary bodies, analysing their spectral reflectance and emission. For the planetary surface of Mercury, which is influenced by extreme environmental conditions, data interpretation must take into account changes in spectral characteristics induced by the high temperatures conditions (Strom and Sprague, 2003). In our approach, we calculate, with *ab initio* methods, IR spectra of olivine and orthoenstatite, which are considered to be component of Mercury's surface (Sprague et al. 2007). The simulation are compared with the measurements of thermal emissivity spectra obtained experimentally at different steps of temperature from 320K to 900K. The aim here is to verify the reliably of this simulation and if it can be used to foresee the trend of spectral features due to temperature. The investigation is mostly focused on the possibility to develop an application of the method on the data that will be acquired by MERTIS, the Mercury Radiometer and Thermal Infrared Spectrometer (MERTIS) (Hiesinger and Helbert 2010) on board of the ESA BepiColombo Mercury Planetary Orbiter spacecraft due in 2018.

The thesis is therefore articulated into two main results chapters, Chapter 3 and Chapter 4, in which the motivations and the results of respectively the Raman mode assignment and the modelling of high temperature TIR spectra for remote sensing, together with their possible applications, are discussed. Such chapters will be preceded by the description of the mineralogical framework of the two minerals investigated, a discussion of the crystal structures, the state of art in matter of experimental and calculations and the characterization of the samples investigated (Chapter 1). Chapter 2 is instead an overview of quantum mechanics calculations methods, discussing the theoretical basis of the approach, the computer code and the computational details employed with preliminary calculated results.

Chapter 1

Mineralogical framework and samples characterization

This introductory chapter aims to draw a mineralogical framework on the minerals, which have been investigated in this study by means of Raman mode assignment and TIR spectra modelling.

The two different minerals we investigated, orthoenstatite $Mg_2Si_2O_6$ and forsterite Mg_2SiO_4, although they belong to different classes of silicates, inosilicate and orthosilicate, share several common features. Both are major constituents in rock forming minerals pyroxene and olivine, both show orthorhombic point *mmm* symmetry, and both are made of Mg, Si and O. Commonly they are found together on the earth upper mantle, and in chondritic meteorites, as well as in rocky planetary bodies.

In the following paragraphs we will discuss their crystal structure and previous experimental and computational spectroscopic investigations, which are preparatory to the discussion of quantum mechanical results. Moreover, the characterization of the two samples of olivine and orthopyroxenes that have been investigated in this study; the chemical and crystallographic experimental data are discussed and reported in paragraph the 1.3.

1.1. Orthoenstatite

Enstatite ($Mg_2Si_2O_6$) is an endmember and a major component of natural pyroxenes. Enstatite forms a solid solution series with ferrosilite ($Fe_2Si_2O_6$) in the mineral orthopyroxene (space group P*bca*), which is a rock forming mineral in mafic and ultramafic assemblages of the Earth crust and upper mantle. Moreover, enstatite is an important constituent of other planetary bodies and meteorites, where a specific class of undifferentiated chondrites takes its name (enstatite chondrites). It is also one of the few silicate minerals that was observed in crystalline form outside

our Solar System, around evolved stars and planetary nebulae (Demichelis et al., 2012). In addition, the enstatite phases are important constituents of steatite ceramics (Reynard et al., 2008).

Enstatite displays a complex polymorphism. Although the orthorhombic phase is the most common, monoclinic $P2_1/c$ clinoenstatite is also found at room temperature, both as a quenched metastable product and as a stable phase below 700°C. At non ambient conditions, clinoenstatite transforms in the high pressure and high temperature HP$C2/c$ and HT$C2/c$ phases, sharing the same space group, but with quite different structure (Angel et al., 1992); orthoenstatite transforms in the *Pbcn* protoenstatite at high temperature and low pressure (Yang and Ghose 1995) and in a HP$P2_1/c$ phase at high pressure (Zang et al., 1997; Zang et al., 2013; Zang et al. 2014). Phase transitions between the enstatite phases have a considerable importance in the thermodynamic and geophysical behaviour of the upper mantle; relations between different polymorphs, their structure, and their vibrational properties have been therefore widely investigated, at room conditions and at high pressure and temperature (Angel and Jackson, 2012).

As a phase belonging to the family of pyroxenes, enstatite is a chain silicate, with tetrahedral chains along the c axis, and two metal sites (M1 and M2) in between. The M1 site is located in a slightly distorted octahedron, whereas the M2 is an irregular polyhedron, hosting cations in six and eightfold coordination. In *Pbca* enstatite, Mg cations occupy both the M1 and the M2 sites in six-fold coordination (see **Figure 1**). In $C2/c$ pyroxenes, the M2 polyhedron is eightfold coordinated, and hosts cations with ionic radius higher than Mg, like Ca and Na.

The different coordination requirements promote a change in the arrangement of the tetrahedral chains. In $C2/c$ pyroxenes, the chains are symmetry equivalent, whereas in the monoclinic $P2_1/c$ symmetry, they are not, since the chains are distorted differently, which means that there are two non-equivalent chains in the unit cell. The orthorhombic enstatite occurs by twinning on (100) of the $P2_1/c$ unit cell, leading to a *Pbca* symmetry and a doubled unit cell volume. Like in the $P2_1/c$, in the *Pbca* enstatite there are two symmetry independent chains, named as chain A or B.

1.1.1. Crystal structure

Each atom in the unit cell of the enstatite is in the general position x, y, z. In enstatite we have then two independent positions for Si, 6 for O and two for Mg. According to the space group *Pbca* (61) each atom is repeated 8 times (**Table 1**).

Independent Si atoms are repeated along the chain, and are named as SiA or SiB. Each Si atom is surrounded by four O atoms, two of them are shared with the previous and the following tetrahedra in the chain. The shared (or bridging) oxygens are named O3, O3A or O3B, according to the chain. The O2 oxygen, together with the bridging O3, forms the basis of the silicate tetrahedron, which at the apex shows the O1 oxygen. The resulting tetrahedra are distorted; the Si-O3 distances are invariably longer than the Si-O1 and O2 distances; moreover in enstatite the average Si-OA distances are shorter than the corresponding Si-OB.

The M1 and M2 atoms are located in structurally different sites also in the C2/*c* symmetry, where they are in special position along the diad axis. In $P2_1/c$ and *Pbca* they are shifted off the pseudo diad axis, in a general position.

Along the *c* axis each tetrahedron is repeated twice in the unit cell, and, as in the orthopyroxene there are 8 chains (symmetrically distinct in four A and four B chains), we have 16 Si atoms, 48 oxygens and 16 Mg atoms, i.e. 80 atoms in the unit cell. There are 10 symmetry independent atoms in general position, which means 30 independent coordinates.

1.1.2. Spectroscopic investigations

In the spectral range of our interest extensive Raman and IR studies were performed. Among Raman investigations, micro-Raman has a special interest, since it analyses on a micrometer scale the polymorphic varieties of enstatite, often mixed together, providing an effective tool for their identification (Ulmer and Stalder, 2001).

Raman spectroscopy has been applied not only as a tool to discriminate between clino-, ortho- and protoenstatite (Reynard et al., 2008; Ulmer and Stalder, 2001) but also to probe the chemical composition of orthoenstatite-orthoferrosilite solid solutions (orthopyroxenes) providing means to determine the orthopyroxene composition (Huang et al., 2000; Wang et al., 2001; Stalder et al., 2009).

The high temperature and high pressure phase transitions were also investigated by Raman (Ross and Reynard 1999; Zang et al., 2013; Zang et al. 2014), and detailed spectra at non ambient conditions were collected to describe the high pressure and high temperature mode behaviours (Lin 2004; Zucker and Shim 2009). Moreover, a number of studies exploited Raman spectroscopy to identify the enstatite phases in rocks and meteorites (Wang et al., 2004).

Infrared spectroscopic studies of pyroxenes in the mid-and far-infrared spectral range have so far been measured for a natural, i.e. terrestrial, enstatite (the Mg-rich variety of the orthopyroxene group) at room temperature (Jager et al. 1998) and a synthetic one at 60 K (Demichelis et al. 2012). Measurements of reflectance spectra have been performed at temperatures between 10K and 928 K to calculate optical based on Lorentz oscillator fits.
(Zeidler et al., 2015). Emissivity measurements of Ca-rich pyroxenes within the TIR range have been always conducted at room conditions (Christensen et al. 2000; Hamilton 2000). Ferrari et al., (2014) measured TIR emissivity spectra in vacuum at high temperature of two Ca-rich clinopyroxenes with a strong different Fe content and similar Ca amount, to provide possible spectral signature changes occurring at the most likely environment of the surface of Mercury. However, to the author knowledge, besides the room temperature emissivity measurements of Hamilton (2000), there is a general lack of thermal emissivity measurements on orthoenstatite sample.
The Raman spectra of clino and orthoenstatite were also simulated by numerical modelling. A pioneering study was performed by Choudhury et al. (1998), who calculated the Raman peak positions of orthoenstatite by means of molecular dynamics, comparing the results with carefully determined experimental spectra in parallel and cross polarization. However, due to the limitation in molecular dynamics, the difference between calculated and experimental positions was quite large (up to 100 cm^{-1}). A more precise fit to the experimental results was obtained in DFT quantum mechanical investigations, where Raman peak positions of ortho- and clinoenstatite were calculated as a by-product of calculations of the energetics and stabilities of the different polymorphs (Yu and Wentzcovitch, 2009). Although these calculations are in closer agreement with experimental data, peak intensities were not computed.

In fact, the high number of allowed Raman peaks (120 in orthoenstatite) makes peak assignment a challenging task, due to overlapping peaks. Therefore, calculation of the intensities is required to provide a correct assignment, i.e. to link a given experimental peak to a calculated one. Most recently, within the Wurm project (Caracas and Bobocioiu, 2011), DFT modelling was

performed systematically over a series of mineral families; intensities and peak positions were calculated and reported for ortho and clino enstatite, however the results were not object of further study. Employing hybrid functionals, the simulation by means of B31LYP conducted by Demichelis et al., (2012) must be quoted, in which the reflectance spectra along the three direction x, y, z of a pure single crystal of orthoenstatite are compared with the calculated spectra at static equilibrium.

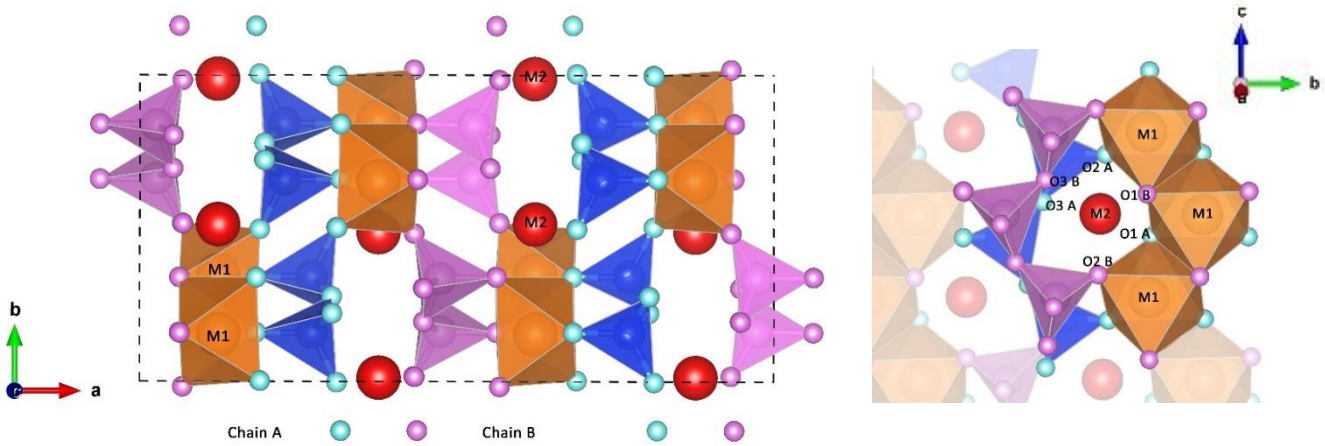

Figure 1: View of the Pbca structure of orthoenstatite, along the [001] axis (on the left) and along the direction normal to it (b); the different bonds of the two Mg cations with the oxygens from A and B chains can be distinguished. The two tethraedral chains have been coloured differently: blue for the chain A and pink for the chain B.

Atom	Wycoff symbol	Representation	Fractional coordinates (Yang &Ghose 1995)		
Mg1	8c	x, y, z	0.376	0.6544	0.8663
Mg2	8c	x, y, z	0.3769	0.4854	0.3609
SiA	8c	x, y, z	0.2716	0.3411	0.0494
SiB	8c	x, y, z	0.474	0.3373	0.7988
O1A	8c	x, y, z	0.1832	0.3386	0.0349
O2A	8c	x, y, z	0.3118	0.5022	0.043
O3A	8c	x, y, z	0.3036	0.2252	-0.1698
O1B	8c	x, y, z	0.5628	0.3382	0.8009
O2B	8c	x, y, z	0.4337	0.4841	0.688

O3B	8c	x, y, z	0.447	0.1961	0.6004

Table 1: atomic coordinates for orthoenstatite Pbca: wycoff positions and fractional coordinates are reported.

1.2. Olivine

Olivines are important rock-forming minerals. On Earth, they are one of the major components of the upper mantle; they are common in many meteorites and have been identified on the surfaces of Mars and some asteroids, in comets, in interplanetary and interstellar dusts, and in the circumstellar regions around some evolved stars (Hamilton 2010). Olivine phases are indicators of low-silica environments, they crystallize at high temperature, and they generally break down readily in the presence of weathering agents such as water. As such, their identification and characterization is a subject of considerable interest to a wide variety of researchers.

The olivine minerals are silicate minerals with orthorhombic symmetry *Pbnm* and have a general formula of X_2SiO_4, where X represents one or more divalent atoms in six-fold coordination with isolated silicate tetrahedra. The most common cations in olivine are Mg^{2+} and Fe^{2+}, forming a solid solution between forsterite (Mg_2SiO_4) and fayalite (Fe_2SiO_4). Compositions in the Mg–Fe series commonly are identified by the molar percentages of forsterite (Fo) and fayalite (Fa), e.g. $Fo_{90}Fa_{10}$ or Fo_{90}.

On Earth, olivine compositions in the forsterite–fayalite (Fo-Fa) series are common in mafic to ultramafic rocks, in which their compositions typically range between $Fo_{85–95}$. Compositions between Fo_{80} and Fo_{50} are typical of gabbroic, peridotitic and basaltic rocks; more Fe-rich compositions are less common, occurring in ferrodiorites, and quartz syenites. They also are present in progressively metamorphosed serpentinites and thermally metamorphosed iron-rich sediments.

1.2.1. The structure

Forsterite is orthorhombic, belonging to the *non-conventional* space group *Pnma* = D_{2h}^{16} (62). It has four formula units per unit cell. The crystal structure of forsterite is built up by SiO_4 and MgO_6 distorted tetrahedra and octahedra, respectively. Si polyhedra share vertices with the Mg ones, but

not with one another. There are two symmetry-independent Mg atoms, named Mg1 (on the inversion centre at 0,0,0) and Mg2 (Hazen 1976). The Mg1 octahedra share edges forming rods parallel to the crystallographic *c* axis, and the Mg2 octahedra are linked laterally to such rods by edge-sharing (**Figure 2**). Si tetrahedra are stuffed in between.

The M2, Si, O1 and O2 atoms are located on mirror planes at 0.25 *z*/*c* and have C_s point symmetry and therefore are in the special x, y, 0.25 positions. The M1 cation is located at the origin of the unit cell and has C_i point symmetry (0,0,0), while O3 oxygens occupy a general positions x, y, z of C_i symmetry. The O3 in general positions are repeated 8 times in the unit cell, whereas the other atoms in general position are repeated four times. Therefore, we have four tetrahedra in the unit cell. The symmetry analysis is reported in **Table 2.** In total there are 28 atoms in the unit cell, 6 of which are symmetry independent, and 11 independent positional variables.

1.2.2. Spectroscopic investigations

A number of IR and Raman spectroscopic investigations have been carried out over the years on both synthetic and natural olivines. The quality of the spectra has improved continuously and the more recent measurements have extended the investigations into the high-temperature and high-pressure regimes. In addition, inelastic neutron scattering studies (Rao et al. 1988; Ghose et al. 1991; Price et al. 1992; Schmidt et al. 1992) have been very useful in interpreting the lattice-dynamic properties of forsterite and fayalite.

Paˆ ques–Ledent and Tarte (1973) made some of the first powder IR and Raman measurements on synthetic end-member forsterite using ^{28}Si–^{30}Si and ^{24}Mg–^{26}Mg isotopic substitution in order to assign the observed bands, but just then, with Kolesov and Geiger (2004) the investigation has been completed with spectra and more detailed discussions on mode assignment.

Hohler and Funk (1973) undertook polarized single-crystal Raman and IR measurements on three different nearly end-member composition olivine-structure phases, which were forsterite-rich ($Fo_{95}Fa_5$), tephroite (Mn_2SiO_4)-rich, and monticellite ($CaMgSiO_4$)-rich, and analysed their lattice-dynamic properties. They observed strong mode mixing at low wavenumbers, and they considered the nature of crystal-field and dynamical splitting of the internal SiO_4 vibrations. Servoin and Piriou (1973) and Iishi (1978) and McMillan (1983) made Raman measurements on different polycrystalline, they concentrated their analysis on the high-wavenumber region and discussed the

nature of mode coupling between internal SiO_4 vibrations. Stidham et al. (1976) measured the single-crystal Raman and IR spectra of synthetic end-member tephroite at 300 and 14 K and confirmed earlier proposals that internal SiO_4 modes do not interact greatly with the low-energy M-site cation vibrations. Chopelas (1991) undertook a single-crystal Raman study of natural and synthetic olivines, including forsterite, fayalite, and monticellite, emphasizing the low-wavenumber modes below 450 cm^{-1}, and she presented new vibrational mode assignments. The most recent single-crystal IR absorption and reflection measurements on forsterite and fayalite were made by Hofmeister (1987, 1997). She also made mode assignments by employing samples of different oxygen isotopic composition. Chopelas (1990) carried out some of the earliest Raman measurements at high pressures in a diamond anvil cell to about 20 GPa on forsterite in order to investigate its thermodynamic properties. Liu and Mernagh (1993) recorded high-pressure Raman spectra to 17 GPa on fayalite and 30 GPa on forsterite. Gillet (1991) undertook a high-temperature Raman study on forsterite to about 1150 K and 10 GPa, and Gillet et al. (1997) made further high-temperature measurements on forsterite up to 2000 K in order to investigate the intrinsic anharmonicity of the Raman-active modes.

Within TIR region studies, more oriented on astronomical simulations in laboratory, previous works (e.g., Bowey et al., 2001; Chihara et al., 2002; Koike et al., 2003) investigated the effect of temperature on the IR spectra of olivine. In particular, Koike et al. (2006) and Chihara et al. (2002) investigated the effect of temperature on the spectra of olivine particles (crystal size 0.1 μm) and, as said for orthoenstatite, Ziedler et al., (2015), must be cited for their investigation at high temperature on a single crystal olivine. Such works were mainly focused on the effect of temperature on circumstellar and interstellar dust and therefore they are out of target, because they are not representative of Mercury surface environment conditions. On a view of the study of Mercury in remote sensing olivine extensive studies have been carried out on the dependence of spectral features on compositions presented by Hamilton (2010) and Lane et al., (2011). On the other hand, investigations conducted by Helbert et al. (2013) show a first approach on the study of emissivity spectra on natural sample of olivine influenced by temperature.

Previous theoretical studies on this compound, as regards both Raman (McKewon et al., 2010) and infrared spectra, the latter both for pure (Li et al., 2007) and H-substituted systems, (Braithwaite et al., 2003, Walker et al., 2006, Shaw et al., 2007). The adopted techniques were molecular dynamics and/or density functional theory. In a previous preliminary investigation of the IR spectrum of

forsterite, (Noet et al. 2006) the B3LYP hybrid functional was adopted (details on hybrid functional in quantum mechanics calculations are discussed in Chapter 2). The same functional was adopted for the study of thermophysical properties of Mg_2SiO_4 polymorphs (Ottonello et al., 2009). Six other hybrid functionals are tested in the latest *ab inito* study (De la Pierre et al., 2011) comparing the relative performances.

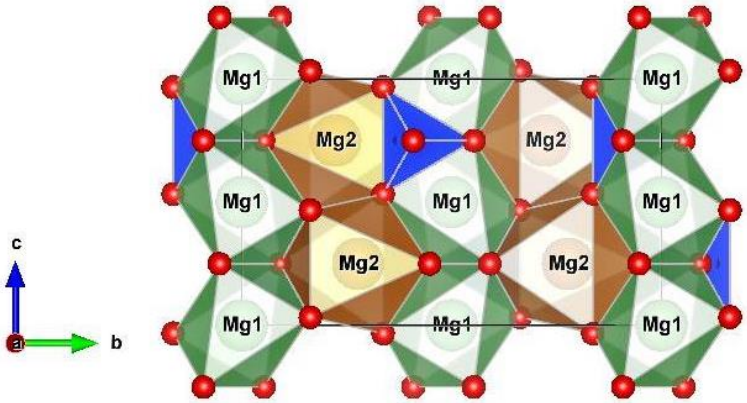

Figure 2: View of the crystal structure of forsterite, Mg2SiO4, along the crystallographic x axis. SiO4 tetrahedra and MgO6 octahedra (corresponding to the two independent Mg1 and Mg2 atoms). Oxygen atoms are shown as spheres

Atom	Wycoff symbol	Representation	Fractional coordinates (Hazen et al. 1976)
Mg1	4a	0, 0, 0	0, 0, 0
Mg2	4c	x, y, ¼	0.9915, 0.2774, 0.25
Si	4c	x, y, ¼	0.4262, 0.0940, 0.25
O1	4c	x, y, ¼	0.7657, 0.0913, 0.25
O2	4c	x, y, ¼	0.2215, 0.4474, 0.25
O3	8d	x, y, z	0.2777, 0.1628, 0.0331

Table 2: symmetry analysis for forsterite. The wycoff positions and fractional coordinates are reported

1.3. Natural olivine and orthopyroxene for TIR investigation: powder diffraction and microprobe analysis

High temperature TIR emission and reflectivity spectra, measured for comparison with calculated spectra, were taken on natural olivine and orthopyroxene belonging to the collection of Planetary analogues of the Institute of Planetary Research, DLR in Berlin. They are both natural samples and their composition is not an endmember composition. They have been named OEN87 and OLIV89, for the orthoenstatite and olivine respectively.

OEN87 is a natural sample of orthoenstatite from Bramble, Norway. The sample appear as multiple single crystals, characterized by a garish colour and a millimetre size.

OLIV89 is a natural sample of olivine, San Carlos quality, Arizona. The sample appear as polycrystalline powder, micrometre grain size, characterized by a pale green colour. Both samples are natural standards widely used in studies preliminary to spectroscopic investigation (Hamilton 2000, Hamilton 2010, Lane et al., 2011, Weber et al., 2014, Zeidler et al., 2015).

The two samples were characterized by X-ray powder diffraction and WDS microprobe analysis. Further spectroscopic characterizations are reported in chapters 3 and 4.

Few powdered grains of the studied samples have been examined by X-ray diffraction (D2 Bruker diffractometer, operating at 30 kV and 10 mA, with a CuKα radiation λ = 1.54178 Å). Intensity measurements were taken in steps of 0.02° over a 2θ range from 10° to 80°, with a counting time of 1 s per step.

No other phase than orthoenstatite for sample OEN87 and olivine for sample OLIV89 was found. The cell parameters were determined by Rietveld analysis, and are reported in **Table 3**. The determination of the unit cell parameters is performed by the Rietveld method with the GSAS-EXPGUI software package. Independent variables for the Rietveld refinement are: zero point, nine coefficients of the shifted Chebyschev function to fit the background, unit cell dimensions and scale factor. A pseudo-Voigt profile function was used, refining one Gaussian (Gw) and two Lorentzian (Lx and Ly) coefficients. The Rietveld analysis is done using structural data from Hazen (1976) for OLIV87 and Yang and Ghose (1995), for OEN87. A good fit of the observed vs calculated patterns is obtained, as $\chi^2 = 1.5$ for OLIV89 and $\chi^2 = 4.2$ for OEN87. The resulting cell parameters are reported in Table 1.

Wavelength-dispersive spectrometer (WDS) microprobe analysis was done on few sample chips embedded in epoxy. The analyses are carried out using a CAMECA CAMEBAX SX50 electron microprobe, with a fine-focused beam (~1 µm diameter), an acceleration voltage of 15 kV and a

beam current of 20 nA, with 10 s counting times for both peak and total background, following the experimental procedures reported in Ferrari et al. (2014). Ten analytical spots are taken and merged for each sample, which proved homogeneous within experimental error.

The resulting formula unit is $Mg_{1.76}Fe_{0.22}SiO_4$ for the sample OLIV87 and $(Ca_{0.01}Mg_{1.73}Fe_{0.25})Si_2O_6$ for sample OEN87, with compositional dispersion below 0.01 a.p.f.u. Cr and Al were found in the orthopyroxene, but with concentration below 0.002 a.p.f.u.

	OLIV89	**Hazen et al. (1976)**	**OEN87**	**Yang and Ghose (1995)**
	$Mg_{1.76}Fe_{0.22}\ SiO_4$	Mg_2SiO_4	$Ca_{0.01}\ Mg_{1.73}\ Fe^{2+}_{0.25}\ Si_2O_6$	$Mg_2Si_2O_6$
a (Å)	4.7615(1)	4.7535(4)	18.2470 (3)	18.21
b (Å)	10.2254(1)	10.1943(5)	8.8430 (2)	8.812
c (Å)	5.9914(1)	5.9807(4)	5.1897 (2)	5.178
V ($Å^3$)	291.72(4)	289.82(25)	837.409 (30)	830.896

Table 3: cell parameters of the samples investigated OLIV89 and OEN87 and their relative endmembers references Hazen et al. 1976 and Yang and Ghose 1995, respectively.

Chapter 2

Quantum Mechanical Calculations

Investigations with quantum mechanical methods means two things: accurate prediction of molecular properties such as structure, stability, electron density etc. and the validation and interpretation of those calculated (or measured) properties in terms of simple models and concepts (Dove 1993). These goals have been actively achieved since quantum chemical methods for calculating atomic and molecular energies with high precision had been developed in parallel to the availability of faster supercomputers.

Nowadays *ab initio* methods are routinely applied with a nearly user-friendly approach, with unique upsides such as physically consistency, accuracy, independence from experimental results and theoretically no limiting conditions.

Practically *ab initio* calculations allow to reproduce properties of a system at any pressure or temperature, with the least possible amount of *a priori* empirical information. It is mandatory an approximated starting structure (i.e. in the case of a crystal structure, symmetry, cell parameters, atomic fractional coordinates are required) as a prior information for a successful calculation, though. The limiting factors are related to the complexity of the system investigated and available computational resources.

This chapter does not stand for a quantum mechanics dissertation; it would go beyond the aims of this thesis and the competence of the author. However, the following paragraphs will be a brief but exhaustive explanation on the principles that allow for the calculation of vibrational frequencies, the best computational approach to simulate a vibrational pattern, the code employed and the computational details.

2.1. The *ab initio* approach

Everything starts from the time independent Schrödinger equation to solve the energy of a system, in this case the ground state energy of a crystal:

$$\mathrm{H}\,\Psi = \mathrm{E}\,\Psi$$

where H is the Hamiltonian operator, Ψ is the wave function, and E is the total energy of the unit cell of the crystal. This dissertation could stop here, because this equation is analytically unsolvable for a system having more than one electron, unless a set of approximations are employed.

The Hamiltonian operator H contains all of the possible energy contributions: kinetic energy of the nuclei; kinetic energy of the electrons; nucleus-electron potential energy; electron-electron potential energy; nucleus-nucleus potential energy (in the above written order and in the following formula):

$$H = -\frac{\hbar^2}{2}\sum_{a}^{N}\frac{1}{M_a}\nabla_a^2 - \frac{\hbar^2}{2m}\sum_{i}^{n}\nabla_i^2 - \sum_{i,a}^{N,n}\frac{z_a\,e^a}{|\overrightarrow{r_i} - \overrightarrow{R_a}|} + \sum_{i,j<i}^{n}\frac{e^2}{r_{ij}} + \sum_{a,b,<a}^{N}\frac{Z_a Z_b e^2}{R_{ab}}$$

where *n* and *N* are respectively the number of electrons and that of nuclei; *e* is the electron charge; M_a and m_a are respectively the mass of the *a*-th nucleus and the mass of an electron; Z_a (or Z_b) is the atomic number of nucleus *a*; *r* and *R* refer to the positions of electrons and nuclei, respectively; $\hbar$ is the Planck's constant divided by 2π.

To solve the Schrödinger equation, the first important and useful approximation is the Born-Oppenheimer (BO) one, which separates the motion of nuclei from that of electrons (the separation is possible, causing a negligible error, due to the large mass difference between the two types of particles). Therefore, it is possible to define an electronic Hamiltonian [$\mathrm{H_{el}}(\vec{R})$] which parametrically depends upon the fixed nuclear coordinates as:

$$H_{el}(\vec{R}) = -\frac{\hbar^2}{2m}\sum_{i}^{n}\nabla_i^2 - \sum_{i,a}^{N,n}\frac{z_a\,e^a}{|\overrightarrow{r_i} - \overrightarrow{R_a}|} + \sum_{i,j<i}^{n}\frac{e^2}{r_{ij}}$$

Resulting a simplified formula for the electron motion only:

$$H_{el}(\vec{R})\Psi(\vec{x};\,\vec{R}) = E_{el}(\vec{R})\,\Psi(\vec{x};\,\vec{R})$$

In this electronic equation, the nuclear positions (specified by the vector $\vec{R}$) appear as a fixed parameter and the calculated energy $\mathrm{E_{el}}$, depends by the specific choice of the nuclear configuration. The coordinates of the electrons have been indicated with the symbol $\vec{x}$ where $\overrightarrow{x} = (\vec{r}; s)$, with $\vec{r}$ being vectors of the spatial coordinates and *s* being the spin coordinates of all the electrons.

The total energy with fixed nuclei (only *static* energy, no kinetic energy of the nuclei) is then immediately recovered by summing the inter-nuclear potential energy term (E_{nn}) to the electronic energy. The static structure at the equilibrium is defined as the nuclear configuration E_{st} that minimizes the function:

$$E_{st}(\vec{R}) = E_{el}(\vec{R}) + E_{nn}(\vec{R})$$

Even if the original equation has been greatly simplified with the recourse to the BO approximation, the *many electron problem* still does not have a solution.

To solve the electronic problem the most common approach in solid state physics is the Density Functional Theory (DFT), named after the fact that the core equations are written in terms of the electron density ρ_0 rather than the electronic wave functions.
In fact, given an *exact* electron density ρ_0, the external potential due to the nuclei (and, hence, the nuclear configuration) is univocally determined (Hohenberg-Kohn's theorem):

$$E_{el}[\rho; \overrightarrow{R}] = \int \rho\varepsilon\,[\rho]d\vec{r}$$

In principles, by *knowing* the $\varepsilon[\rho]$ functional, it is possible to minimize the energy E through a self-consistent field algorithm (SCF).
Since each electron contributes to the electron density in every point of the space, the interaction of each electron with itself is implicitly included. This interaction is the Coulomb contribution and represents the self-interaction problem. This issue is exactly removed at the Hartree-Fock level by the compensating effect of the *exact exchange* term. Within the DFT framework, the exchange functional is approximated, thus an exact compensation does not occur: a residual of this interaction exists and it is called the *self-interaction error* (SIE) that can be partially corrected if the Hamiltonian employed contains a fraction of the HT *exact* exchange (*hybrid Hamiltonian*). Indeed, at variance with the DFT methods, which are focused on the use of the electron density, the HF approach was the chemist's *wave-function* (*one determinant*) method to solve the electronic problem (however, since long time, new approaches have overcame the HF approximation with *polydeterminantal*, or perturbative, or *coupled cluster* techniques)). As wrote above, in DFT, the exchange functionals can be mixed with a fraction of the HF exchange (hybrid functionals) in order to reduce the self-interaction error. The following examples of this study employ just *hybrid* HF/DFT Hamiltonian, where the DFT exchange part is corrected with a percentage of HF exact exchange term. As demonstrated by (letteratura) hybrid HF/DFT functionals can provide very accurate vibrational

frequencies for crystals, which are a fundamental ingredient for simulating thermal and pressure effects on thermo-elastic properties (and thermal expansion) of crystalline solids, as it is discussed in the next section.

2.2. Vibrational frequencies within the quasi-harmonic approximation

For a crystal at the *static equilibrium*, the energy is proportional to the square of the nuclear displacements, with the proportionality factor related to the second derivatives of the static energy with respect to the nuclear coordinates (derivatives evaluated at the equilibrium point in the reciprocal space $\vec{R}$). Under these conditions (*harmonic approximation*), for a finite system (molecule) with *N* nuclei, the nuclear motion is describable as the collection of 3*N*-6 *independent* harmonic oscillators (*N* is the number of nuclei; 6 degrees of freedom describe translations and rotations), each one being characterized by its distinctive frequency v and energy E:

$$E(n,\nu) = \left(n + \frac{1}{2}\right) h\nu$$

where *n* is the *vibrational quantum number* and *h* is the Planck's constant.
For an infinite crystal, having *N* nuclei in the unit cell, the total vibrational energy is given by the expression:

$$E_{vib} = \sum_{i}^{3N} \int_{BZ} [n_i\,(\vec{k}) + \frac{1}{2}] h\nu_i(\vec{k}) d\vec{k}$$

The integral is extended over the Brillouin zone, within the reciprocal space.

The functions $\nu_i(\vec{k})$ are known as dispersion relations; the quantum numbers $n_i(\vec{k})$ depend by the temperature (T) through the Bose-Einstein distribution

$$n_i(\vec{k}) = \frac{1}{e^{h\nu_i(\vec{k})/KT} - 1}$$

where K is the Boltzmann's constant. In the *quasi-particle* framework, the vibrational quantum excitations are called phonons, and each *n* is the number of phonons with a definite frequency

(normal mode), at a given temperature. From this perspective, at 0 K there are no phonons in the crystal but, as the temperature is increased, a phonon gas is created which is confined within the crystal.

The vibrational frequencies of a *purely harmonic* crystal are invariant with respect to the *rescaling* of the unit cell volume: indeed, the frequency of a harmonic oscillator is independent by the amplitude of the oscillator itself.

In a *real* crystal, the Born-Oppenheimer (BO) surface, over which the nuclei move, can be considered *harmonic* only in a small neighbourhood of the equilibrium nuclear configuration ($\vec{R}_{st}$) at any given unit cell volume *V*). If the cell volume is significantly changed (for instance by means of an applied external pressure), a new equilibrium configuration is reached, which is characterized by different values of the vibrational frequencies. This is called the *quasi-harmonic* approximation and frequencies depend on the volume of the crystal.

As a direct consequence of the frequencies variation with the cell volume, also the vibrational energy changes or, more correctly at finite temperature, the Helmholtz free energy *F* changes; since pressure is defined as the derivative of *F* with respect to *V*, at constant *T* (with sign reversed), a *vibrational pressure* can be defined through the relation

$$P_{vib}(V,T) = -\left(\frac{\partial F_{vib}(V,T)}{\partial V}\right)_T$$

P_{vib} can be decomposed in the sum of a zero point pressure (P_{zp}; at 0K there are no phonons, however the energy of the fundamental level of each vibrational mode is not zero, and changes with the volume V) and a thermal pressure (P_{th}) due to the phonon gas. At the equilibrium, the sum of the static (P_{st}), the zero point and thermal pressures must equal the applied external pressure (P_{ext}), and this condition is realized at a particular value of the unit cell volume: the volume at the equilibrium (V_{eq}):

$$P_{ext} = P_{zp}(V_{eq}) + P_{th}(V_{eq}) + P_{st}(V_{eq})$$

As the temperature is increased, the (normally positive) thermal pressure of the phonon gas increases (mainly due to the increased number of phonons, following the Bose-Einstein statistic).

To maintain the equilibrium, P_{st} must decrease, and therefore the unit cell volume must increase. Such phenomenon is known as thermal expansion.

2.3. CRYSTAL code and the algorithm to calculate vibrational frequencies

The calculations in this work have been carried out with the CRYSTAL code.

CRYSTAL is a quantum-mechanical code, which performs ab initio calculations of the ground state energy, energy gradients, electronic wave function along with structural, elastic and vibrational properties of periodic systems. This quantum mechanics program computes the electronic structure of periodic systems within the Hartree–Fock (originally) and density functional theory (DFT). In comparison to other quantum mechanical codes, this code employs *localized* atomic functions (AO: *atomic orbitals*) and therefore is very *convenient for employing hybrid* HF/GGA-DFT Hamiltonians. Crystal orbitals are expanded as linear combinations of atom-centered Gaussian-type functions. Normally when a DFT approach is used, the electron density is build with plane waves (PW), which are greatly inconvenient to evaluate the Hartree-Fock exchange, since it requires a great computational cost; therefore HF exchange is usually not evaluated when PW are employed. The whole procedure is known as LCAO (Linear Combination of Atomic Orbitals). All-electron ab initio calculations for all phases have been performed in the framework of hybrid functional, as already expressed.

The code is capable to extensively exploit the symmetry of the system to achieve computational efficiency.

Chosen a level of theory and the model (more details on the hybrid Hamiltonian, the basis set and the computational parameters employed will be listed in appendix) and solved the ground state energy of the system investigated, the extraction of physical properties (observables) are obtained by partial derivations of the total-energy: structural, vibrational and elastic properties of crystalline solids can be determined, almost automatically as set in the input.

However, some brief remarks on the algorithm carried out to perform vibrational frequencies calculations must be given. For a detailed discussion of the method, please refer to a previous paper (Pascale et al., 2004).

To summarize, these steps lead to the calculations of vibrational frequencies at Γ point of the first Brillouin Zone (BZ):

- first of all, a local minimum on the potential energy surface (PES) is localized through a geometry optimization procedure, hence by the analytical calculation of energy gradients;
- the nuclei are then displaced from their equilibrium positions within the limits of the harmonic approximation (finite displacement method), and the second derivatives of the energy, with respect to such displacements, are numerically calculated as first derivative of the analytical first derivative of the energy(Hessian or dynamical matrix);
- finally, phonon frequencies are evaluated as the eigenvalues of the weighted Hessian matrix by diagonalization.

Phonon frequencies calculated at Γ point of the first Brillouin Zone (zone-center phonons) represent the optic modes and they can be directly compared with the experimental values measured by IR and Raman spectroscopy.

As a relatively new feature of the code (CRYSTAL14 release), IR and Raman spectra can be fully simulated, thanks to the introduction of analytical computation of the peak intensities. Thus, one can simulate a spectrum that can be directly compared with experiments.

2.4. Remarks on simulations of IR and Raman spectra

More information on the computational details used to carried out the simulations in this study are given in the paragraph of computational details, where are discussed the main computational parameters (Hamiltonian, basis sets), computational tools (mass substitution and building unit decomposition) and a focus regarding the issues on high temperature calculations.

Taking for granted the theoretical background behind the two spectroscopic phenomena, the intent here is to simply remark that once the phonon frequencies has been computed, as seen before, to calculate IR and Raman intensities, Born charge and the second rank polarizability tensor must be analytically evaluated. Follow some details on the simulations of vibrational spectra.

2.4.1. IR spectra

Once the vibrational frequencies and the dielectric tensor have been calculated, the infrared spectra can be calculated at almost zero computational cost. Atomic Born tensors, the oscillator strengths, the longitudinal optic mode and transversal optic mode splitting (LO/TO splitting) and the static

dielectric tensor are the key quantities for the calculation of the IR intensities, which are computed through Coupled-Perturbed Hartree-Fock/Kohn-Sham approach, entirely analytically.

The key quantity is the complex dielectric tensor $\epsilon(\nu)$, which is computed for each inequivalent polarization direction on the basis of a classical Drude-Lorentz model:

$$\epsilon_{ii}(\nu) = \epsilon_{\infty,ii} + \sum_{p} \frac{f_{p,ii}\nu_p^2}{\nu_p^2 - \nu^2 - i\nu\gamma_p}$$

Where *ii* indicates the polarization direction ϵ_∞ is the optical dielectric tensor, ν_p, f_p and γ_p are the TO frequencies, oscillator strength and damping factor for the p^{th} vibrational mode, respectively. The real and imaginary parts of $\epsilon(\nu)$ are computed; the maxima of the latter function correspond to the TO frequencies. The imaginary part of $1/\epsilon(\nu)$ is computed as well, whose maxima correspond to the LO frequencies. Moreover the real and the imaginary parts of the refractive index *n*(ν) are obtained for each inequivalent polarization direction.

A simulated reflectance curve $R_{tt}(\nu)$ along the hypothetical tt direction can be obtained by means of the Fresnel formula:

$$R_{tt}(\nu) = \left| \frac{\sqrt{\epsilon_{tt}(\nu) - sin^2(\theta)} - \cos(\theta)}{\sqrt{\epsilon_{tt}(\nu) - sin^2(\theta)} + \cos(\theta)} \right|^2$$

where θ is the incidence angle of the IR beam with respect to the normal to the surface and $\varepsilon_{tt}(\nu) = \varepsilon_{1,tt}(\nu) + i\varepsilon_{2,tt}(\nu)$ is the *tt*th component of the complex dielectric function. The maxima of $\varepsilon_2(\nu)$ and of $Im(-1/\varepsilon(\nu))$ (Loss Function) correspond to the transverse optical (TO) and longitudinal optical (LO) frequencies, respectively. Note that, when the symmetry of the system is orthorhombic as for orthoenstatite and forsterite, ε(ν) is a diagonal tensor, so that only the xx, yy, and zz components of the tensor are not equal to zero.

2.4.2. Raman spectra

Raman intensities are computed using a fully analytical approach. It combines analytical gradients (Doll et al. 2001) with solutions of first-order and second-order coupled perturbed Hartree–Fock/Kohn–Sham equations (Ferrero et al. 2008) for the linear and quadratic orbital responses to electric fields in the different Cartesian directions. For the linear response, there are three directions

to consider, whilst for the quadratic response, there are six pairs corresponding to the six independent components of the polarizability tensor.

When simulating the experimental Raman spectrum of a real crystal, a number of factors must be taken into account. For an oriented single-crystal the Raman Stokes scattering intensity associated with, for instance, the xy component of the polarizability tensor corresponding to the *i*-vibrational mode of frequency ω_i may be calculated as:

$$I_{xy}^{i} \propto C \left(\frac{\alpha_{xy}}{\partial Q_i}\right)^2$$

Where Q_i is the normal mode coordinate for mode i.

The prefactor C depends (Veithen et al. 2005) on the laser frequency ω_L and on the temperature T:

$$C \sim \left(\omega_L - \omega_p\right)^4 \frac{1 + n\left(\omega_p\right)}{30\omega_p}$$

with the Bose occupancy factor $n(\omega_p)$ given by

$$1 + n\left(\omega_p\right) = \left[1 - \exp\left(-\frac{\hbar\omega_p}{k_B T}\right)\right]^{-1}$$

In the cases showed in the next chapters the polycrystalline (powder) spectrum can be computed by averaging over the possible orientations of the crystallites (Prosandeev et al., 2005).

2.5. Computational details

2.5.1. Computational parameters

As previously said in the *ab initio* approach paragraph**,** the theoretical framework is the *hybrid* HF/DFT Hamiltonian one. In the following case studies (Chapter 3 and 4), the hybrid Hamiltonian WC1LYP has been employed, where the DFT exchange part (GGA) is corrected with a percentage of HF exact exchange term (16% HF exchange). The DFT exchange part is non-empirical (Wu and Cohen, 2006) and provides better results with respect to PBE functional. The correlation is described by the LYP functional (Lee et al., 1988).

It must be remarked that the following basis sets and computational parameters here reported has been applied for both simulations of forsterite and othoenstatite.

The utilized all-electron Gaussian-type basis set are 8-511d1G for Mg, 88-31G* for Si and 8-411d11G for O, the basis sets where taken from http://www.crystal.unito.it/basis-sets.php. Since the

chemistry of the two systems investigated is made of Mg, Si and O, but of course in different arrangements (forsterite Mg_2SiO_4, orthoenstatite $Mg_2Si_2O_6$ for more details about the mineralogical framework, please refer to Chapter 1), the same basis sets have been employed for both.

Going into details of the computational parameters, the level of accuracy in evaluating the Coulomb and Hartree–Fock exchange series is controlled by five parameters (Dovesi et al. 2013), defined by the TOLINTEG keyword in CRYSTAL. These 5 parameters were set to 8, 8, 8, 8, 18 (see the CRYSTAL manual and the works of Dovesi et al. 1983 and Causà et al. 1988). The threshold on the total energy for convergence of the self-consistent field was set to 10^{-8} hartree for the orbital optimizations and to 10^{-10} hartree for the construction of the Hessian (by numerical differentiation of analytical gradients). Reciprocal space was sampled using a regular sublattice with shrinking factor of 4, corresponding to 24 independent ***k*** vectors in the irreducible part of the Brillouin zone. The exchange-correlation contribution to the Fock matrix was evaluated by numerical integration over the unit cell volume. Radial and angular points for the integration grid were generated through Gauss–Legendre radial quadrature and Lebedev two-dimensional angular point distributions. In the present work, a pruned grid with 75 radial and 974 angular points was used (see XLGRID keyword in the CRYSTAL manual. Details about the grid generation, the number of points in reciprocal space, and their influence on the accuracy and cost of calculation, can be found in theworks of Pascale et al., 2004 and Zicovich-Wilson et al., 2008.

The crystal structures were optimized on the basis of analytical energy gradients with respect to fractional atomic coordinates and unit cell parameters (referring to Doll 2001, Civalleri et al. 2001). Default values were chosen for convergence of gradient components as well as nuclear displacements. The calculated equilibrium lattice parameters of the two optimized structures are reported here in Table 4 and **Table 5** and discussed in Chapter 3 and Chapter 4.

Vibrational wavenumbers and normal modes were calculated within the limit of the harmonic approximation, by diagonalizing a mass weighted Hessian matrix, whose elements are the second derivatives of the full potential of the crystal with respect to mass weighted atomic displacements. The first derivatives of the energy with respect to the atomic positions are calculated analytically, whereas second derivatives are calculated numerically by setting to 0.003 Å the nuclear displacements with respect to the equilibrium positions. Relative Raman and IR intensities were computed using a fully analytical approach previously discussed and which are invoked in CRYSTAL14 by appropriate keywords (for more details CRYSTAL14 user's manual). All the Raman

and IR frequencies calculated for orthoenstatite and olivine are reported in table in the Appendix Tables 1 to 4.

2.5.2. Investigation tools at zero computational cost

Once the Hessian matrix H is calculated, frequency shifts due to mass substitutions can readily be obtained by simply changing the masses in the matrix. This allows the calculation of the isotopic-shifts at no computational cost.

The contribution of a given atom to the overall vibration can be assessed by means of mass substitution. In the Raman mode assignment case of study (Chapter 3), in both cases of orthoenstatite and forsterite, mass substitutions were performed, substituting Fe atomic mass for Mg mass in the M2 and M1 sites, separately and together, and of ^{18}O and ^{30}Si isotopes for the oxygen and silicon respectively in order to assess the mass contribution. These calculations are activated by the keyword ISOTOPES, which allows the modification of the atomic mass of a specific atom defined by input. With ISOTOPES calculations, the atomic mass of one atom can be modified, without any modification of the electronic wave function or geometry optimization, since the mass of the atoms are not present in the single particle electronic Hamiltonian. This has the advantage to separate the contributions due to the changing mass of the vibrating atoms, with those due to the interatomic force constants. More details about the results can be found in the paragraph of Isotopes shifts and mode assignment in Chapter 3.

Moreover eigenvectors are also used for the graphical representation of the atomic motion in the modes employing graphical interface software as Moldraw (for more details please check http://www.moldraw.unito.it/_sgg/f10000.htm)

2.5.3. Calculation at high temperature: a standard statistical-thermodynamics approach

As said in the Introduction, one of the goals of the present study is to foresee the trend of spectral features due to temperature and, as it will be described in Chapter 4, to study which features are more influenced by an increase of temperature in order to simulate the situation that occurs on the Mercury's surface during the day. To do so, calculations must be performed by evaluating the vibrational frequencies of the unit cell at different volumes: volume increases as a consequence of an increasing temperature, following a a standard statistical-thermodynamics approach, within the

limit of the quasi-harmonic approximation. More details about the procedure can be found in Prencipe et al. (2011); here, a brief overview on the procedure and on the parameters which have been (or have not) taken into account, is presented This procedure will be applied for the considered phases: ortho-enstatite and forsterite for the modelling at high temperature of emissivity spectra for remote sensing. Follow a quick overview of the procedure scheme.

Zero point and thermal pressures (see the above paragraph 2.2) are calculated by following a standard statistical-thermodynamics approach, within the limit of the quasi-harmonic approximation, and added to the static pressure at each volume, to get the total pressure (P) as a function of both temperature (T) and cell volume (V). The resulting P(V, T) curves are fitted by appropriate EoS', to get bulk modulus (K_0) and its derivative (K'), at different temperatures. In this study,in order to fit the P,V points at any given temperature, a third order Birch-Murnaghan equation has been employed. The calculated data will be compared with the available experimental data from literature concerning compressibility at room temperature and the low values observed for the thermal expansion coefficient (see tables in paragraph 2.6). All these parameters were obtained in the limit of the quasi-harmonic approximation (Anderson 1995), through the evaluation of the unit cell volume dependence of the frequencies of the vibrational normal modes (mode-γ Grüneisen's parameters) at the Γ point.

Dispersion effects in the phonon spectra at various pressures were not taken into account as the large volume of the unit cell makes it impossible the required calculation of the vibrational frequencies in the case of super-cells, due to limitation of the available computational resources. On the other hand, the Grüneisen's parameters corresponding to the zone-centre vibrational modes can reasonably be considered representative of the whole set of parameters, due to their large number which depends upon the number of atoms in the unit cell. Indeed, as demonstrated by other authors (Ottonello et al. 2008, 2009, 2010), highly reliably estimations of thermo-elastic and thermodynamics quantities can be obtained by neglecting dispersion effects, even in case of systems having relatively small unit cells. This is consistent with the general observation that thermodynamic properties, which are obtained as averages over the relevant quantities at the atomic level, can reliably be derived even without a detailed knowledge of the phonon density of state (Kieffer 1979a).

Intrinsic anharmonic effects (Oganov and Dorogokupets 2004) were not taken into account, though they could play a role in determining frequencies and Grüneisen's parameters of the lower frequency modes, especially at very high temperatures. At the not extremely high temperatures of our calculation (max temperature 1000 K), they are, however, expected to be small (Oganov and Dorogokupets 2004).

The procedure's reliability has been estimated from previous works already published for the calculation of thermo-elastic properties of minerals (see for instance: Ungureanu et al. 2010; Prencipe et al. 2011; Scanavino & Prencipe 2013; Belmonte et al. 2014).

2.6. Calculated cell parameters and Equation of State (EoS) results for orthoenstatite and forsterite

The calculated equilibrium lattice parameters optimized at the WC1LYP level (static values: no *zero point* and thermal effects included; see below in the text) are reported in **Table 4** and **Table 5**. There, zero point and thermal pressures at 0K, 300K and 1000K and their impact on the calculated structure of orthoenastatite and forsterite are estimated by calculating the full vibrational spectrum at the Γ point at different unit cell volumes, according to the procedure previously described.

The bulk modulus (K_0), its first derivative (K') and the volume (V_0) calculated at the static equilibrium and at the three different considered temperatures 0K, 300K and 1000K including zero point effects are listed in **Table 6** and **Table 7.**

For forsterite, the calculations successfully reproduce the available experimental data especially at room temperature. In **Table 6** are reported experimental data at 300K according to Finkelstein et al. (2014), who measured K_0 at 130.0 (9) GPa, to be compared with the calculated K_0 of 131.1 GPa; $\partial K/\partial T$ = 0.0217 GPa/K according to a linear fit within the range of 300-800K. Thermal expansion at 300K is 2.43 K^{-1}; according to the value found by Bouhifid et al. (1996), the calculated thermal expansion shows a good agreement at 400K, where we calculate 2.80 K^{-1} which is the same experimental value.

The calculated data for orthoenstatite shows a minor agreement with the experimental data in literature (**Table 7**), especially considering thermal expansion. In fact the calculated thermal expansion at 300K is evaluated as 9.64 x 10^{-6} K^{-1}, while data from Jackson et al. 2003 shows at 300K a thermal expansion of 34.5(17) x 10^{-6} K^{-1}.

	This sample	Yang and Ghose (1995)	calculated $Mg_2Si_2O_6$			
	$Ca_{0.01}\ Mg_{1.73}\ Fe^{2+}_{0.25}\ Si_2O_6$	$Mg_2Si_2O_6$	Static eq	0K	300K	1000K
a (Å)	18.2470 (3)	18.21	18.285	18.322	18.306	18.385
b (Å)	8.8430 (2)	8.812	8.285	8.871	8.884	8.898
c (Å)	5.1897 (2)	5.178	5.225	5.231	5.236	5.247
V ($Å^3$)	837.409 (30)	830.896	846.8	850.2	851.6	858.6

Table 4: Lattice parameters and unit cell volume of: the sample studied, of the reference from Yang and Ghose (1995) and of calculated orthoenstatite computed with CRYSTAL14.

	This sample	Hazen et al. (1976)	Calculated Mg_2SiO_4			
	$Mg_{1.76}Fe_{0.22}\ SiO_4$	Mg_2SiO_4	Static equilibrium	0 K	300 K	1000 K
a (Å)	4.7615(1)	4.7535(4)	4.76648	4.76667	4.7808	4.8064
b (Å)	10.2254(1)	10.1943(5)	10.18197	10.18279	10.23989	10.33828
c (Å)	5.9914(1)	5.9807(4)	5.97715	5.97742	6.00483	6.05119
V ($Å^3$)	291.72(4)	289.82(25)	290.084	290.132	293.966	300.683

Table 5: Lattice parameters and unit cell volume of: the sample studied, of the reference from Hazen et al., 1976 and of calculated forsterite computed with CRYSTAL14.

	Static equilibrium	0 K	300 K	300 K Finkelstein et al. (2014)	1000 K
V_0	290.149 ($Å^3$)	292.909 ($Å^3$)	293.972 ($Å^3$)	290.1(1) ($Å^3$)	300.701 ($Å^3$)
K_0	138.2 GPa	134.6 GPa	131.1 GPa	130.0(9) GPa	116.1 GPa
K’	4.01	3.99	4.08	4.12	4.3

Table 6: calculated and experimental volume cell V_0, bulk modulus an K_0 and K’ for forstesrite.

	Static equilibrium	300 K	300 K Angel & Jackson (2002)
V_0	847.611 (Å^3)	851.62 (Å^3)	832.89 (11) (Å^3)
K_0	90.91 GPa	88.6 GPa	105.8 (5) GPa
K’	10.86	10.9	8.5 (3)

Table 7: calculated and experimental volume cell V_0, bulk modulus an K_0 and K’ for orthoenstatite.

Chapter 3

Raman mode assignment by quantum mechanical calculation

The main subject of this thesis are the vibrations of atoms in the crystal lattice. The atomic vibrations can be described in terms of lattice dynamics, which consider those vibrations as harmonic travelling waves (Dove 2011) and, as it was previously demonstrated in Chapter 2, considering a real crystal lattice, they can be calculated within the framework of the harmonic approximation.

Lattice dynamics allows to understand some important phenomena: the interaction of light with matter is probably the most important example of the role of lattice dynamics. The absorption of certain frequencies in the infrared spectral region is directly due to the existence of specific atomic vibrations. Moreover, lattice dynamics leads to the derivation of fundamental thermodynamics properties, and predict e.g phase transitions, thermal conductivity and thermal expansion for a given phase.

Developments in the study of lattice dynamics come from new generation instruments for neutron scattering, particularly with the ability to collect data over wide ranges of scattering vector and energy simultaneously. More improvements come either from simulations; experiments coupled with software able to simulate the outputs of experimental results and, of course, the calculations of phonon frequencies by means of quantum mechanics, represent the more consistent tool of analysis.

The following case studies (one dedicated to orthoenstatite and the other one to forsterite) are examples of lattice dynamics by means of *ab initio* calculations, employing hybrid HF/DFT approach for its accuracy and reliability in the calculation of vibrational frequencies. This approach has been carried out by means of the computer code CRYSTAL14, which enable a reliable simulation of a full vibrational pattern as it has been shown in the previous Chapter.

In the two case studies here discussed, the aim is to show the importance of a proper Raman mode assignment into a vibrational pattern, in order to study the structure of a mineral and to link the most sensitive peaks to pressure and temperature, to the structure, studying the Raman shifts.

Raman mode assignment is frequently complicated by several factors i.e. a great number of peaks due to the number of vibrational modes (e.g. 240 normal modes for orthoenstatite, 120 of which are Raman active) or, as in forsterite, the combination of modes and the low intensity of peaks at low wavenumbers, which hinders their assignment. In this study the comparison with experimental Raman measures, from this work or from literature, coupled with the calculations of vibrational frequencies and relative intensity enable a consistent symmetry attribution, which is the first step to unravel the whole vibrational pattern.

The mode assignment in both cases has been performed, attributing a motion to each active mode, a graphical representation and the weight of that mode into the overall vibration. This was done with tools at zero computational cost, just inspecting the eigenvalues of the Hessian matrix calculated.

The following results and discussions have been partly published for the orthopyroxene on Journal of Raman Spectroscopy and can be found at this link: DOI 10.1002/jrs.4942 as Stangarone et al., 2016. Data for olivine have been recently submitted on Journal of Raman Spectroscopy as weel and are currently on minor revisions.

3.1. Orthoenstatite case study

Abstract

Raman spectra of orthoenstatite have been computed from first principles, employing the hybrid Hamiltonian WC1LYP (Wu and Cohen 2006). The calculated data show excellent agreement with the experimental data from literature with an absolute average difference of ~5 cm^{-1}. The quantum mechanical simulation allowed the assignment of Raman features to specific vibrational modes. This enabled to assess quantitatively the contributions of internal (tetrahedral stretching) and external (tetrahedral chains and M1 and M2 cations) vibrations. Moreover, the mass substitution of ^{56}Fe for ^{24}Mg in the M1 and M2 sites and of ^{30}Si and ^{18}O for the ^{28}Si and ^{16}O sites, pointed out the relative contributions of the cations to each mode within different sites.

The description of the Raman modes enabled to relate the major experimental peaks to specific structural vibrations, and to link the changes in crystal structure to those modes with pressure, temperature and composition.

The results provide new clues to identify most suitable peaks for the investigation of the intracrystalline ordering of Fe and Mg in the M1 and M2 sites, and of Al in the tetrahedral and octahedral sites. Moreover it was possible to identify those peaks which are related to structural features, like tetrahedral bond distances.

3.1.1. Results

3.1.1.1. Mode analysis

The orthoenstatite Raman spectrum is one of the most complex in pyroxenes, being the result of as much as 120 Raman active modes; it can be described better comparing it with other enstatite polymorphs and their structure. Orthoenstatite has eight formula units ($Mg_2Si_2O_6$) per unit cell, i.e. 80 atoms requiring 240 vibrations (3n, where n is number of atoms per unit cell). At the centre of the Brillouin zone, the symmetry assignment of the 240 normal modes of orthoenstatite is:

$$\Gamma = 30A_g + 30B_{1g} + 30B_{2g} + 30B_{3g} + 30A_u + 30B_{1u} + 30B_{2u} + 30B_{3u}$$

There are therefore 120 Raman active modes ($30B_{1g}$, $30B_{2g}$, $30B_{3g}$ and 30 A_g), 87 IR active modes ($29B_{1u}$, $29B_{2u}$ and $29B_{3u}$), 30 'silent' A_u modes; three 3 modes, corresponding to pure translations have B_{1u}, B_{2u} and B_{3u} symmetry. The most frequent peak found in literature compared with calculated are listed in Table 8, more discussion in the text.

In C2/c pyroxenes factor group analysis gives rise to 30 Raman active modes: most of them can be experimentally identified, in polarized light experiments (Prencipe et al., 2012; Prencipe et al., 2011). In the $P2_1/c$ symmetry, there are 60 Raman active modes, of which 30 can be observed in parallel polarization (A_g) and 30 in cross polarization (B_g).

The unit cell, doubled in *Pbca* orthoenstatite, with respect to the monoclinic $P2_1/C$ cell, doubles also the number of the modes. The A_g symmetry modes are the most intense and useful for the purpose of mineral identification and spectroscopic analysis: unpolarised spectrum consists almost completely of A_g modes (Figure 3). The B_g modes are generally weaker and can be identified by the analysis of spectra in cross polarization configuration (Choudhury et al., 1988; Chopelas 1999). However, the high number of modes hinders a careful experimental analysis due to overlap in close peaks. In addition, the simple description of the modes in terms of definite structural vibrations is difficult: the pyroxene structure has little crystallographic constrains, due to its low symmetry, and

allows significant polyhedral deformation. In their investigation on polarized spectra of orthoenstatite, Choudhury [18] managed to measure and to identify successfully all the A_g and some of the B_{1g} and B_{3g} modes, but none of the B_{2g}.

In previous papers (Huang et al., 2000; Wang et al., 2001; Choudhury et al., 1988), three different kind of vibrations were identified: 1) vibration of cations in M1 and M2 polyhedron, occurring with varying contribution from the tetrahedral chains; 2) bending of the tetrahedral chains, involving both or one of the two symmetry equivalent chains; 3) stretching into the SiO_4 tetrahedron, with minor contribution from the M1 and M2 cations. They were identified to specific group of wavenumbers, i.e. group 1 for wavenumbers between 200 and 400 cm^{-1}, group 2 between 400 and 800 cm^{-1}, and tetrahedral stretching to higher wavenumbers. However, although the above assignment can provide a preliminary information, mode assignment is more complex, since previous quantum mechanical investigation on the *C2/c* pyroxenes showed that a combination of the above vibrations might contribute to the same mode (Prencipe et al., 2014; Prencipe 2012). As described in the following, it has little meaning to say that a mode is due e.g. to M1-O bending, as long as it will likely have a significant contribution in bending and stretching from the tetrahedral chain. Instead, the description of a given mode should enlighten the prevailing mechanism, and account for the different contributions.

To unravel the different contributions of the atomic vibrations, we have performed a *building unit decomposition* analysis (see the CRYSTA Users Manual, Dovesi et al., 2014) of the vibrational modes: they are decomposed in terms of internal and external motions of some defined units. The external motions correspond to rotations and translations of the units behaving as rigid blocks, while the internal motions refer to the relative movements of the constitutive atoms in each unit. In pyroxenes, the internal contributions come from the bending or stretching of the tetrahedral units, while the external contribution comes from the vibration of the tetrahedral chains without an internal deformation; the vibrations of the M2 and M1 atoms fall in the range of the external contribution (formally, such units are built by a single atom, so there cannot be an *internal* contribution). The results, in terms of numbers and percentages are summarized in Table 8 and will be discussed later.

The contribution of a given atom to the overall vibration was also assessed by means of isotopic substitution of Fe atomic mass for Mg mass in the M2 and M1 sites, separately and together, and of ^{18}O and ^{30}Si isotopes for the oxygen and silicon respectively. These calculations are

activated by the keyword ISOTOPES, which allows the modification of the atomic mass of a specific atom defined by input. With ISOTOPES calculations, the atomic mass of one atom can be modified, without any modification of the electronic wave function or geometry optimization, since the mass of the atoms are not present in the single particle electronic Hamiltonian. Moreover, if a frequency calculation is performed with standard atomic mass, new wavenumbers with different atomic masses for selected atoms can be computed from the Hessian already computed. This has the advantage to separate the contributions due to the changing mass of the vibrating atoms, with those from the interatomic force constants. The choice of the much heavier Fe mass, instead of a Mg isotope, was performed in order to assess the mass contribution for the Fe-Mg substitution in the Raman spectra of enstatite-ferrosilite orthopyroxenes. The contributions of the building units from enstatite can be found for each vibrational mode in Table 9.

In the following general trends are discussed, in order to identify the vibrational behaviour prevailing in a given wavenumber range.

3.1.1.2. Building unit decomposition

As expected from the results in *C2/c* clinopyroxenes (Prencipe et al., 2012), we find that also for orthopyroxene most modes are a combination of internal and external contributions (Figure 5 and Figure 4, Table 9). The majority of modes showing predominat internal contributions are most at higher wavenumbers, where they account almost completely for the description of the Raman mode intensities, and decrease with decreasing wavenumbers. This is quite similar for both A_g and B_g vibrations. The external contribution is complementary, but it must be further subdivided into tetrahedral vibrations contribution and Mg in the M1 and M2 sites vibration.

Within the internal contribution (Figure 5: Building unit decomposition of the 120 Raman vibrational modes. Here is plotted the contribution of the internal tetrahedral vibrations to the overall vibration for each mode.) five ranges can be identified, that we also reported in Fig. 2, where ranges are reported as R1 to R5: 1) below 150 cm^{-1}, where the internal contribution is less than 10%; 2) between 150 and 350 cm^{-1} where it is below 20%; 3) between 350 and 600 cm^{-1} where it linearly increases between 20 to more than 80%; 4) between 600 to 800 cm^{-1}, where it is between 75 and 80% and 5) for higher energy wavenumbers where it is more than 80%. Purely internal contribution is never found (Table 9). Tetrahedral contribution dominates the overall vibration from wavenumbers above 750 cm^{-1}. A contribution of Mg in M1 and M2 atoms is present at the lower

wavenumbers, mostly between 200 and 400 cm^{-1}, but tetrahedral internal and external contributions generally prevail.

3.1.1.3. Mass and isotopic substitutions

3.1.1.3.1. M1 and M2 mass substitution

The isotopic substitution of Fe in the M1 and M2 sites induces a downshift of the peak positions for modes below 760 cm^{-1} (Figure 4).

In the substitution of Fe for Mg in the M1 site, the downshifting is maximum at 250 cm^{-1}; between 250 to 400 cm^{-1} the wavenumber downshifts by an amount between 20 and 40 cm^{-1}. The downshifting is lower at higher wavenumbers and is not present for wavenumbers higher than 760 cm^{-1}. The same substitution for the M2 site shows a similar trend, but with the maximum shift observed in few modes at lower energy, at about 200 cm^{-1}.

The complete Fe isotopic substitution in M2 and M1 sites decreases the wavenumber by 40 to 60 cm^{-1} between 200 to 400 cm^{-1}. The maximum downshift increases up to 200 cm^{-1} and decreases from 400 to 760 cm^{-1}, showing a pronounced linear trend.

3.1.1.3.2. Si and O isotopic substitution

The isotopic substitution was calculated for each of the two Si atoms of A and B chains separately and for each of the six symmetry independent oxygens; eight separate calculations were performed (Figure 6).

Oxygen isotopic substitution downshifts the wavenumbers for most modes, whereas the Si isotopic substitution affects significantly the calculated wavenumbers only above 600 cm^{-1}. In fact, oxygens are involved also in vibration due to the M1/M2-O, even if the internal tetrahedral contributions are less significant. The isotopic substitution changes the wavenumbers by more than 5 cm^{-1} only for the O1A and B and the O2A and B, for some modes between 400 and 600 cm^{-1} and above 900 cm^{-1}, and for the O3A and B, between 600 and 900 cm^{-1}. At wavenumbers higher than 900 cm^{-1} the contribution for the O1 and O2 atoms is maximal, especially O2 oxygens at the highest wavenumbers, whereas the O3 contribution becomes not significant.

3.1.2. Discussion

3.1.1.4. Mode assignment

Combining the results of isotopic substitution and building units decomposition, we outlined the prevailing vibrational pattern for each wavenumber range. Details for each range can be found in Table 9 where we analyse the more intense and diagnostic peaks, reported by Lin (2003), compared with our calculated data. Moreover, the motion has been described by means of the graphic interface software Moldraw (http://www.moldraw.unito.it/_sgg/f10000.htm), which implements the vibrational pattern of each mode, by analysing the eigenvectors.

The range defined as (R1) is from 79 cm^{-1}, first mode, to 150 cm^{-1}. It shows stiff external lattice movements, without an internal deformation of tetrahedra. The mode with the highest intensity in this group is found at 79 cm^{-1} (A_g), where tetrahedra oscillate stiffly along the b axis and where the contribution of chain A prevails; here both Mg cations are dragged by tetrahedra, but at a greater extent for the Mg in the M2 site. This mode has often been overlooked as most Raman spectra have been measured from 100 cm^{-1}, but it is diagnostic for the identification of the orthopyroxene phase [2]. The motion for the mode at 127 cm^{-1} (A_g) is rather similar to the one at 79 cm^{-1}, but here the contribution of the B chain is predominant. Modes at 81 cm^{-1} and 108 cm^{-1} are respectively of B_{2g} and B_{3g} symmetry, as reported by Lin (2003) . They are again stiff lattice oscillations, where chains vibrate onto the (001) plane. At higher wavenumbers, the vibration of Mg in the M2 sites becomes significant.

In the second range (R2) we recognized two subranges:

a) from 150 to 300 cm^{-1}, where M2 contributions are predominant with respect to other cations. The peak with higher M2 contribution is at 248 cm^{-1} (B_{2g}). In this range, both chains are involved in the vibration, but the motion can be different for the two chains. For example at 206 cm^{-1} (A_g), the A chain performs a Si-O3-Si bending, whereas the B chain swings rigidly onto the (001) plane. On the other hand it has been observed that at 161 cm^{-1} (B_{1g}), 236 cm^{-1} (A_g) and 277 cm^{-1} (A_g), the chains vibrate with the same tilting motion along the a axis, but with a different percentage;

b) in the second subrange, from 300 to 350 cm^{-1}, the contribution of Mg in the M1 site increases consistently, reaching its maximum at about 325 cm^{-1} (A_g). Here the B chain is almost stationary and the A chain vibrates for the bending of the O2 atom with Mg in the M2 site. There is also a contribution of the internal deformations of the tetrahedra (Table 3). The most intense peak in our unpolarised calculated spectra is the one at 343 cm^{-1} (A_g), where the motion is characterized by the tilting of both tetrahedral chains, due to O1 and O2 vibrations. Both the M2 and M1 cations vibrate, but the isotopic contribution from the M2-O vibration is higher.

The range between 350-600 cm^{-1} (R3) is characterized by an almost equal percentage of both rigid movements of the lattice and internal strains of the tetrahedra. The contribution from the internal tetrahedral vibration increases steeply and, in some modes, the isotopic contribution from the oxygens may be significant. In this range a lower but significant contribution from the M1 and, to a lesser extent, from M2 is still present. Also here the range can be further divided into two sub-ranges: a first one (R3a) between 350 and 470 cm^{-1}, with balanced internal and external contribution, and a second one (R3b), where the internal contribution begins to prevail and the contribution of the M2 and M1 cations starts to decrease gradually. The R3a range is characterized by low intensity doublets and triplets (see Figure 3), whereas in R3b few peaks are measured experimentally. In the R3a subrange both chains vibrate, but with different movements and the vibration of Mg in the M1 site gives the highest contribution. The triplet consisting of three A_g modes at 387 cm^{-1}, 406 cm^{-1} and 426 cm^{-1} is noteworthy. The motion of the chains for the first mode is a prevailing stretching of O1 inside the A tetrahedron; for the second mode both chains vibrate, O1 oxygen swinging along the a axis in the B chain and the tetrahedra tilting above and below the b axis. For the last mode of the triplet, at 426 cm^{-1}, the vibration involves both chains, but more the A chain, where the motion of tetrahedra is mainly due to the O1 oxygen. In general, in the R3 range, analysing the oxygen mass substitution, it seems that most of the contribution to the vibration comes for O1 and O2 atoms, i.e. those having shorter bonds with M1 and M2 cations, respectively. In the second subrange (R3b) few significant peaks experimentally observed,are present. An exception is the one at 594 cm^{-1} (B_{1g}) which was ascribed to a O2-Si-O1 bending in the A chain combined by the vibration of the O2 together with the two Mg in M1 and M2.

A fourth range (R4) in the spectrum occurs between 600 and 760 cm^{-1}, where the most intense peaks are those at 660 and 680 cm^{-1}, both A_g modes. This range was defined as bending zone [11], where the contribution to the overall vibration consists of internal vibrations of the tetrahedra, with the characteristic bending of O3-Si-O3. The peak at 660 and 680 cm^{-1} shows different contributions from the A and B chains.

In a fifth range (R5) the M2 and M1 cations contribution is less than 1%. The modes in this final part of the spectrum are characterized by internal strains of the tetrahedra, and by a different contribution of the two chains to the overall vibration. This range can be further divided in two subranges. Within R5a, modes are characterized with a higher contribution from the O3 oxygen, the most intense is the A_g mode at 866 cm^{-1} and the doublet, not very intense, consisting of two A_g

modes at 924 cm^{-1} and 933 cm^{-1}. For R5b subrange, the higher contribution comes from Si-O1 and O2 stretching within the tetrahedron. In this last subrange, we find the final triplet at wavenumbers higher than 1000 cm^{-1}, which is described as symmetric and asymmetric stretching of Si-O within the tetrahedra.

The above observations can be easily related in terms of bond distances and crystal chemical requirements (Appendix, Table 5). The average bond distances are longer in the M1 and M2 polyhedra than in the Si centred tetrahedra: it means that the modes with higher contribution from the M1 and M2 sites are the ones with the lower wavenumber. The same goes within the tetrahedron bond distances: the Si-O3 distances are the longest and the Si-O3 stretching modes are those with the lower energy among Si-O stretching modes. The high intensity and high wavenumber A_g doublet at 1012 cm^{-1} and 1027 cm^{-1} is most related to Si-O2 vibrations and the Si-O2 distances are the shortest in the tetrahedron.

In terms of crystal chemistry (Camero et al., 1973; Mantovani et al., 2013; Mantovani et al., 2014; Gori et al.; 2015) the O3 oxygens are overbonded, since they are bridging between tetrahedra and receive their charge contribution from the two Si atoms and the M2 atoms, whereas the O2 and, less, the O1 are underbonded. Tetrahedral bond distances change consequently and a change in the reduced mass for O1 and O2 promotes a higher shift in the highest energy modes. Moreover, only the O1 and O2 atoms are bonded to the M1 cations (Figure 1, Chapter 1), which accounts for the contribution in some modes between 350-500 cm^{-1} of the O1 and O2 oxygens, but not of the O3. The contribution of the O3 to the modes involving the M2 and M1 atoms is quite small, since they are the chain bridging atoms. In fact their contribution to the vibration becomes significant in modes related to chain bending within the 600-700 cm^{-1} range.

3.1.1.5. Fe-Mg substitution and orthopyroxene composition by Raman spectroscopy

In the partial substitution of Fe^{2+} for Mg^{2+} both cations have the same charge, therefore the space group does not change along the whole composition range of the solid solution series enstatite-ferrosilite. Fe^{2+} has a higher mass and a larger size than Mg^{2+}, thus Mg and Fe do not enter randomly the two cationic site M1 and M2, but Fe enters preferentially the more distorted (and slightly larger) M2 polyhedron (Domeneghetti et al., 1985)

The intracrystalline distribution coefficient:

$$K_D = [Fe_{M1}]*[Mg_{M2}]/[Fe_{M2}]*[Mg_{M1}]$$

is temperature dependent (Tarantino et al., 2002a; 2002b; Wang et al. 2005), and varies in volcanic and metamorphic orthopyroxenes between 0.2 to 0.02. It is an important marker for the cooling history in meteoritics, volcanics and slowly cooled terranes (Tribaudino et al., 1992; Domeneghetti et al. 1995; Stimpfl et al., 2005).

In Figure 7, we report the Raman shift vs composition of several peaks along the $Mg_2Si_2O_6$ - $Fe_2Si_2O_6$ series. The expectation is that the increased mass of Fe decreases the energy of the modes, at least those where a significant contribution from the M1 and M2 cation exists. This is observed for the peaks up to 800 cm^{-1}, but the experimentally measured peak wavenumbers decrease with Fe content more than calculated by simple isotopic substitution of Fe with the lighter Mg.

Actually, the mode wavenumbers depend not only on the mass, but also on the force constants, which are in turn related to the bonding type and bond lengths. The higher ionic radius of Fe promotes longer bond lengths and lower coulombic contributions to the oxygen bonding: it promotes a further contribution to decrease the energy of the modes when Fe exchanges for Mg. Apparently the contribution from mass, which can be modelled by our isotopic substitutions (Figure 6), and that for the changing structure, are comparable (Figure 7).

The above considerations do not hold for modes at higher wavenumbers (> 800 cm^{-1}), which are ascribed to the internal vibrations of the tetrahedra. Actually, the peaks at 866 and 933 cm^{-1} do show an increase in wavenumbers with Fe content, whereas the peak at 1010 cm^{-1} shows higher wavenumbers in Mg richer orthopyroxenes. Again, changes in tetrahedral bond distances along the $Mg_2Si_2O_6$-$Fe_2Si_2O_6$ series, must be taken into account. In orthoenstatite endmember the two O1 and O2 atoms are closely bound to Si, whereas the O3-Si bridging oxygen distances are longer. As Fe increases, the bond distances in the tetrahedron come closer together: the distance of Si with the O3 decreases, while O1 and O2 increase (Appendix, Table 5) (Mantovani et al., 2015). To note, on average, the tetrahedral size does not change. As shown by isotopic substitution in Figure 4 the modes at 866 and 933 cm^{-1} are most affected by the O3 atomic vibrations, and, decreasing the Si-O3 bond distance with increasing Fe, it is not surprising that the mode wavenumber increases too. The mode at 1010 cm^{-1}, mainly due to vibrations involving O2, coherently decreases its wavenumber with the increasing Si-O bond distance, according to a higher content of Fe.

Isotopic analysis predicts also that Fe-Mg ordering can have a significant effect on Raman peak positions. As it comes out from the observed site partitioning, in natural intermediate orthopyroxenes Fe is almost completely confined into the M2 site, and Mg in the M1 site (Tribaudino

et al., 1992); Fe occupies at a larger extent the M1 site only in Fe richer orthopyroxenes. In the isotopic modelling of the partitioning between M1 and M2, the configuration in which Mg fully occupies the M1 site, is an ordered model, close to the experimental observation, whereas when Fe occupies M1 and Mg M2, is an anti-ordered one. According to our calculations in most of the modes the discrepancy between the ordered and anti-ordered models is very small (Figure 7), but in the relatively strong peak at 302 cm^{-1} a marked difference between ordered and anti-ordered configuration is found. This mode could be a candidate to reveal differences within Fe-Mg ordering, since the substitution of Fe in M1 downshifts the peak much more than that of Fe in M2. The few experimental available data for the peak at 302 cm^{-1} can be better fitted in the ordered model (Figure 7), confirming that the mode at 302 cm^{-1} is a potential probe for Fe-Mg intracrystalline ordering. At the author knowledge, no experimental investigation was performed to verify the effect of Fe-Mg cation ordering on Raman active modes. According to changes among the degree of cation ordering in orthopyroxenes, a sensitive peak was found by Tarantino et al. (2002), by means of IR spectroscopy technique.

Among other important cation substitutions in orthopyroxenes, like Ca for Mg into M2 site and Al for Mg and Si into M1 and T sites, there are a few experimental results (Zhang et al., 2013; Huang et al., 2000; Wang et al.; 2001), but no systematic investigation devoted specifically to the analysis of the effect on Raman spectra on Ca and Al entrance in orthopyroxenes. However with this approach we can provide some suggestion on the expectable changes. For instance, the entrance of Al into the tetrahedral sites will mostly affect the tetrahedral stretching modes at higher wavenumbers, as Al increases the tetrahedral bond strenght (Sharma and Simons 1983; Tribaudino et al., 2012). Instead, the entrance of Al in the M1 site will affect the modes involved with M1 vibrations: we can foresee that an increasing amount of Al goes into the M1 site, which has shorter bonding, higher charge and lower mass and therefore can shift the vibrations more affected by the M1 site to higher energy. Although Raman data on natural Al-rich orthopyroxenes are also lacking, the presence of tetrahedral Al is expected to be experimentally significant. In C2/c pyroxenes, the highest energy peak at 1010 cm^{-1} in diopside decreases to 953 cm^{-1} in the Ca-Tschermak pyroxene ($CaAl_2SiO_6$), where half of the tetrahedral sites are occupied by Al (Periotto et al., 2012). Likewise, we can expect that the Ca for Mg exchange downshifts the wavenumber of the peak related to the M2 site vibration. In fact this effect was observed, beyond the effect of phase transitions, in the $CaMgSi_2O_6$-$Mg_2Si_2O_6$ pyroxenes (Okamura et al., 1974).

3.1.1.6. Raman modes and structure: relations with HP/HT Raman behaviour

The above discussion shows that changing mass and bond parameters provide a clue to interpret and, potentially, predict the mode behaviour in response to changing composition, once the mode assignment has been performed correctly. Furthermore, this approach can be extended conveniently to analyse the behaviour of HP/HT Raman modes in comparison with HP/HT structural data. For this purpose, enstatite is a good candidate, since a number of in situ high quality single crystal XRD data are available and only bond distances are modified by pressure and temperature changing. Here we just take into account high temperature/pressure behaviour of the doublet at 664/686 cm^{-1}, here calculated at 668/693 cm^{-1} (Figure 8), which is intense and well resolved, and therefore potentially useful for diagnostic purposes (Huang et al., 2000; Wang et al., 2004; Okamura 1974).

The doublet at 664/686 cm^{-1} is described as a bending of the tetrahedral chains (Angel and Jackson 1992). However, according to our calculations performed with isotopic substitution Figure 4, a contribution from M1 and M2 atoms is also present. The split of the doublet occurs as only one of the two symmetry independent tetrahedral chains is in turn involved in the mode vibrations: the mode at 664 cm^{-1} involves a vibration of the B chain, whereas that at 686 cm^{-1}, the A chain. In C2/c pyroxenes a single mode at 670 cm^{-1} is present, and the transition from *C* to *P* pyroxenes is marked by the peak split at 664/686 cm^{-1} of the formerly unique peak at 665 cm^{-1} (Mantovani et al., 2015; Okamura et al., 1974). The higher energy of the vibration from the A chain can be related taking into account the tetrahedral bond distances. In fact within the tetrahedron, Si A bond distances are shorter than the Si B (on average 1.629 vs 1.640 Å and in particular the O3 bridging oxygen, which most contributes within this vibration 1.653 vs 1.675 Å). Moreover, the shorter distance between M1 and any atom of the tetrahedral chain, i.e. the M1-O2 distance, is less between M1-O2A than between M1-O2B (2.001 vs 2.053 Å). This distance, which is the shortest between M1/M2 cations, together with tetrahedral oxygens, is supposed to affect significantly the tetrahedral chain vibration.

In Figure 9, is plotted the wavenumbers of the peaks at 664/686 cm^{-1} vs the bond distance of the shorter M1-O2 distance in the M1 polyhedron (a) and vs the average T-O distance (b). The plot was carried out with the M1-O2a and average TA-O distances for the peak at 686 cm^{-1} and with the. M1-O2b and average TB-O distances for the peak at 664 cm^{-1}. Each of the Raman data in Figure 9 was plotted against structural parameters taken at the same experimental conditions: every point

corresponds to a given P-T condition. The Raman peak positions at high pressure and temperature were interpolated from Lin (2003) and Zucker et al. (2009) to the P-T conditions of the in situ single crystal measurements (Tribaudino 1996). A single linear trend with pressure and temperature is clearly observed with the M1-O distances; the same could be observed, but with higher dispersion of the data points, from the average tetrahedral bond distance (Figure 9 a and b). The larger distribution likely comes from the higher relative experimental uncertainty in structural determination, in turn related to lower changes in bond distances with pressure and temperature in the tetrahedron. Therefore the mode changes are determined mostly by bonding with the M1 cation and by intratetrahedral stretching, rather than by the chain rotation. We can therefore expect that these modes, quite strong and well measureable, will be very sensitive to any structural substitution in the M1 site.

Table 8: Comparison between the 120 calculated Raman peak positions and the experimental data from literature. Δν is the difference between ν calculated (this work) and experimental (from literature). In the statistics given at the bottom of the table, N is the number of peaks considered, <|Δ|> is the mean absolute difference, in wavenumber, and max Δν is the maximum absolute difference, min Δν is the minimum absolute difference. In the Lin spectrum, the intensities are classified as strong s, medium m, weak w and shoulder h.

This work		Lin, 2003			Stalder et al. 2009		Chopelas 1999		Zhang et al. 2013	
ν cm^{-1}	Symm	ν cm^{-1}	I	Δν	ν cm^{-1}	Δν	ν cm^{-1}	Δν	ν cm^{-1}	Δν
79	(A_g)	83	s	-4			83	-4		
81	(B_{2g})	106.8	w	-26						
108	(B_{3g})	115.4	w	-8			115	-7		
127	(A_g)	134.3	ms	-7	133.8	-6.8	134	-7	137.4	-10
159	(A_g)	155.3	wm	4			153	6		
161	(B_{1g})	161.5	vw	-1						
166	(B_{3g})	166.7	w	-1			166	0	170.2	-4
184	(B_{1g})								190.1	-6
195	(B_{1g})	196.9	wm	-2	197.5	-2.6	197	-2	196.5	-2
201	(A_g)								201.1	0
206	(A_g)	206.5	wsh	-1	206.4	-0.5			208.3	-2
236	(A_g)	238.2	ms	-2	239	-2.7	237	-1	240.1	-4
238	(B_{2g})						239	-1	241.1	-4
248	(B_{2g})	244.8	msh	3			245	3	246.3	2
270	(A_g)						261	9	260.8	9
277	(A_g)	278.2	w	-1					271.6	6
296	(B_{3g})								286.5	10
305	(A_g)	301.5	w	3	302.5	2.3	302	3	303.2	2
325	(A_g)	323.3	wsh	2						
327	(B_{3g})	327.7		-1						
341	(B_{2g})								340.3	1
341	(B_{1g})								342.9	-2
343	(A_g)	343.5	svs	0	343.9	-0.5	343	0	345.4	-2
379	(B_{1g})								374	5
387	(A_g)	383.8	wm	3	385.2	1.9			381	6
406	(A_g)	402.1	m	4	402.8	3.5	402	4	402.6	4
426	(A_g)	421.7	m	4	422.7	2.9	422	4	424.2	1
451	(A_g)	445.5	w	6	445.9	5.5	446	5	445.4	6
458	(B_{1g})								448	10
458	(A_g)	458.8	vw	0			457	1	458.6	0
474	(B_{2g})	472.9	vw	1					478.7	-5
481	(A_g)						487	-6	488.3	-7
536	(A_g)	524.9	m	11	527	8.6	519	17	528.1	7
542	(B_{3g})				540.8	0.9	540	2	541.9	0
552	(A_g)	551.5	m	0	553.5	-1.5	553	-1	554.5	-3
566	(B_{3g})	580.3	m	-14			580	-14	582.1	-16

594	(B_{1g})	594.5	vw	-1	581	13				
668	(A_g)	663.8	svs	5	664.8	3.6	665	3	664.9	4
693	(A_g)	686.1	vs	7	687.1	5.7	687	6	687.7	5
760	(B_{2g})	750.7	w	9					752.7	7
866	(A_g)	851.1	m	15	853.2	12.6	886	-20	851	15
924	(A_g)	926.6	m	-2	927.9	-3.4	927	-3	929.6	-5
933	(A_g)	935.2	w	-2	936.5	-3.1	937	-4		
1012	(A_g)	1011.3	vs	0	1013.2	-1.6	1014	-2		
1027	(A_g)	1032.9	svs	-6						
1039	(A_g)				1034.7	4.7	1034	5		
	<|Δ|>			5		4		5		5
	maxΔν			-26		13		-20		15.8
	min Δν			0		0		0		0

Table 9: building unit decomposition of the vibrational modes: they are decomposed in terms of internal (INT) and external (EXT) motions of some defined units. The external motions correspond to rotations and translations of the units behaving as rigid blocks, while the internal motions to the relative movements of the constitutive atoms. For a) and b) column, refer to Fig. 2

	Calculated	Symmetry	Motion		int+ext contribution of T		Tetrahedra vibration		Cations		
	ν (cm^{-1})		EXT	INT	chain A	chain B	A int	B int	M1	M2	
Range 1	79	(A_g)	98.2	1.8	59.5	16.7	0.2	1.6	9.4	14.5	
	81	(B_{2g})	98.6	1.4	77.4	4.8	0.2	1.1	6.7	11.0	
	108	(B_{3g})	97.5	2.6	23.6	59.2	0.4	2.2	2.4	14.8	
	127	(A_g)	96.5	3.5	17.0	77.5	0.4	3.1	0.9	4.6	
Range 2	159	(A_g)	94.6	5.4	80.5	10.4	4.2	1.2	5.8	3.4	a)
	161	(B_{1g})	96.3	3.7	58.6	32.5	2.2	1.4	4.6	4.2	
	166	(B_{3g})	89.9	10.1	52.2	18.2	5.0	5.2	15.0	14.5	
	195	(B_{1g})	98.8	1.2	24.6	57.3	1.0	0.2	1.1	17.0	
	206	(A_g)	98.3	1.7	49.2	24.6	0.7	1.0	1.7	24.5	
	236	(A_g)	91.0	9.0	24.6	57.8	2.0	7.0	13.8	3.8	
	248	(B_{2g})	85.7	14.3	29.2	21.2	6.9	7.4	11.0	38.6	
	277	(A_g)	89.2	10.8	20.3	53.1	1.4	9.4	10.2	16.3	
	305	(A_g)	78.3	21.7	35.6	26.3	7.4	14.3	28.4	9.7	b)

	325	(A_g)	81.3	18.7	37.8	9.8	13.8	5.0	46.2	6.1	
	327	(B_{3g})	79.2	20.8	31.9	16.2	13.0	7.8	43.0	8.7	
	343	(A_g)	87.1	12.9	39.8	49.4	5.4	7.5	3.4	7.3	
Range 3	387	(A_g)	63.9	36.1	39.8	40.6	20.6	15.5	16.9	2.9	a)
	406	(A_g)	59.1	40.9	40.2	39.8	22.2	18.7	12.5	7.5	
	426	(A_g)	40.0	60.0	55.0	31.4	34.2	25.8	10.0	3.5	
	451	(A_g)	58.7	41.3	30.6	50.1	17.7	23.7	10.6	8.7	
	458	(A_g)	55.3	44.7	66.6	14.5	35.6	9.2	17.5	1.4	
	474	(B_{2g})	24.9	75.1	49.0	41.8	37.6	37.5	6.6	2.4	
	536	(A_g)	15.9	84.1	12.6	83.0	11.0	73.1	2.2	2.1	b)
	552	(A_g)	14.6	85.5	37.9	54.6	32.2	53.3	3.8	3.7	
	566	(B_{3g})	22.3	77.7	32.6	50.5	30.9	46.9	4.2	12.8	
	594	(B_{1g})	16.1	83.9	88.5	3.3	81.8	2.1	3.7	4.6	
Range 4	668	(A_g)	27.1	72.9	2.1	89.6	2.0	71.0	3.9	4.4	
	693	(A_g)	21.0	79.0	90.9	2.1	77.2	1.8	3.7	3.4	
	760	(B_{2g})	17.0	83.0	26.3	73.0	21.9	61.0	0.3	0.5	
Range 5	866	(A_g)	14.2	85.8	0.1	99.9	0.1	85.7	0.0	0.0	a)
	924	(A_g)	10.7	89.3	67.4	31.6	58.4	31.0	0.4	0.5	
	933	(A_g)	10.6	89.4	67.4	32.2	57.9	31.5	0.2	0.3	
	1012	(A_g)	6.5	93.5	61.6	37.7	58.2	35.2	0.2	0.4	b)
	1027	(A_g)	4.1	95.9	9.6	90.2	9.0	86.8	0.1	0.1	
	1039	(A_g)	4.5	95.5	94.3	5.5	90.3	5.1	0.2	0.1	

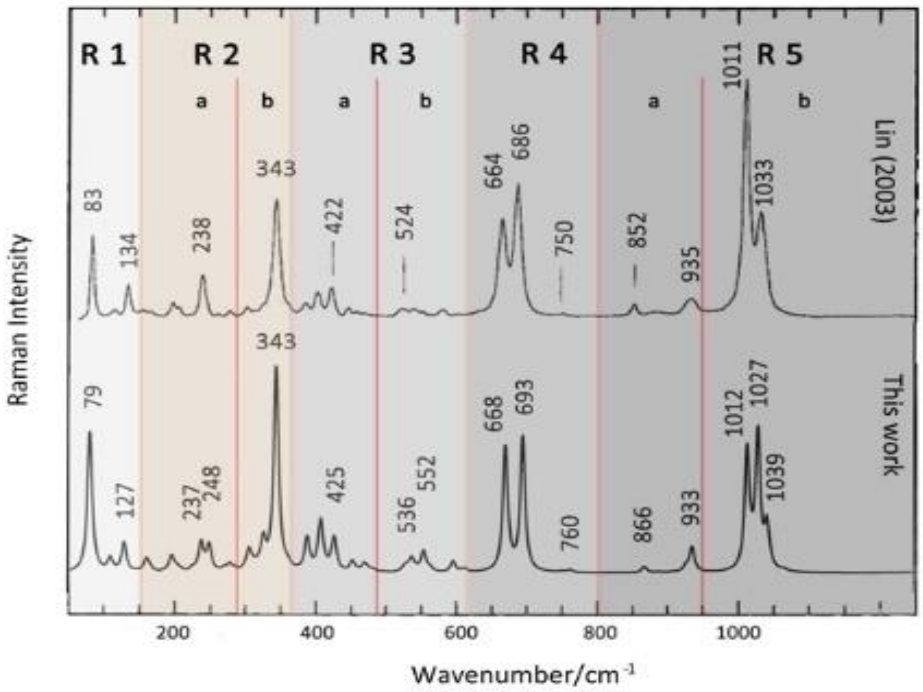

Figure 3: comparison between (top) the experimental Lin (2003) and calculated (bottom) non-polarized spectrum of orthoenstatite. The Raman pattern has been devided into fiv ranges (R1 to R5) and six subranges (a and b), following the discussion in the text.

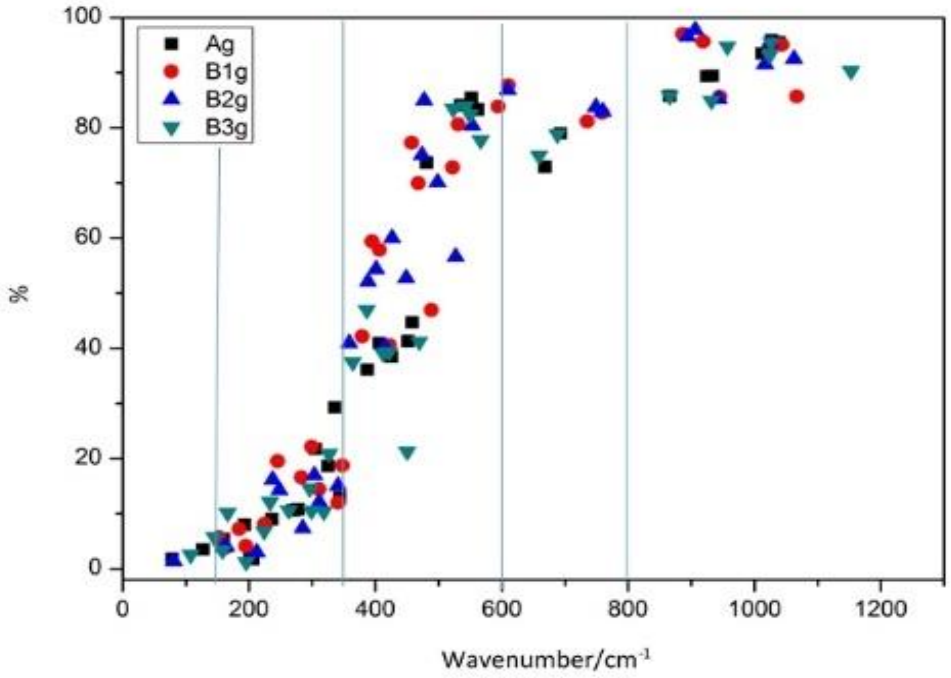

Figure 5: Building unit decomposition of the 120 Raman vibrational modes. Here is plotted the contribution of the internal tetrahedral vibrations to the overall vibration for each mode.

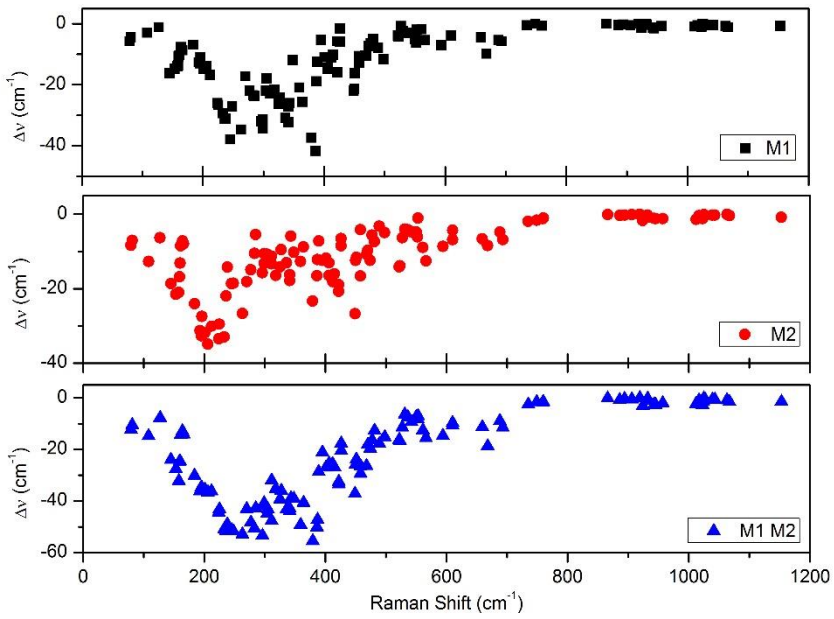

Figure 4: Shift of the Raman wavenumbers for the isotopic substitutio of an atom with the mass of 56Fe for Mg, in M1, M2 and M1 + M2 sites. All the 120 Raman active modes have been considered, as in Figure 2.

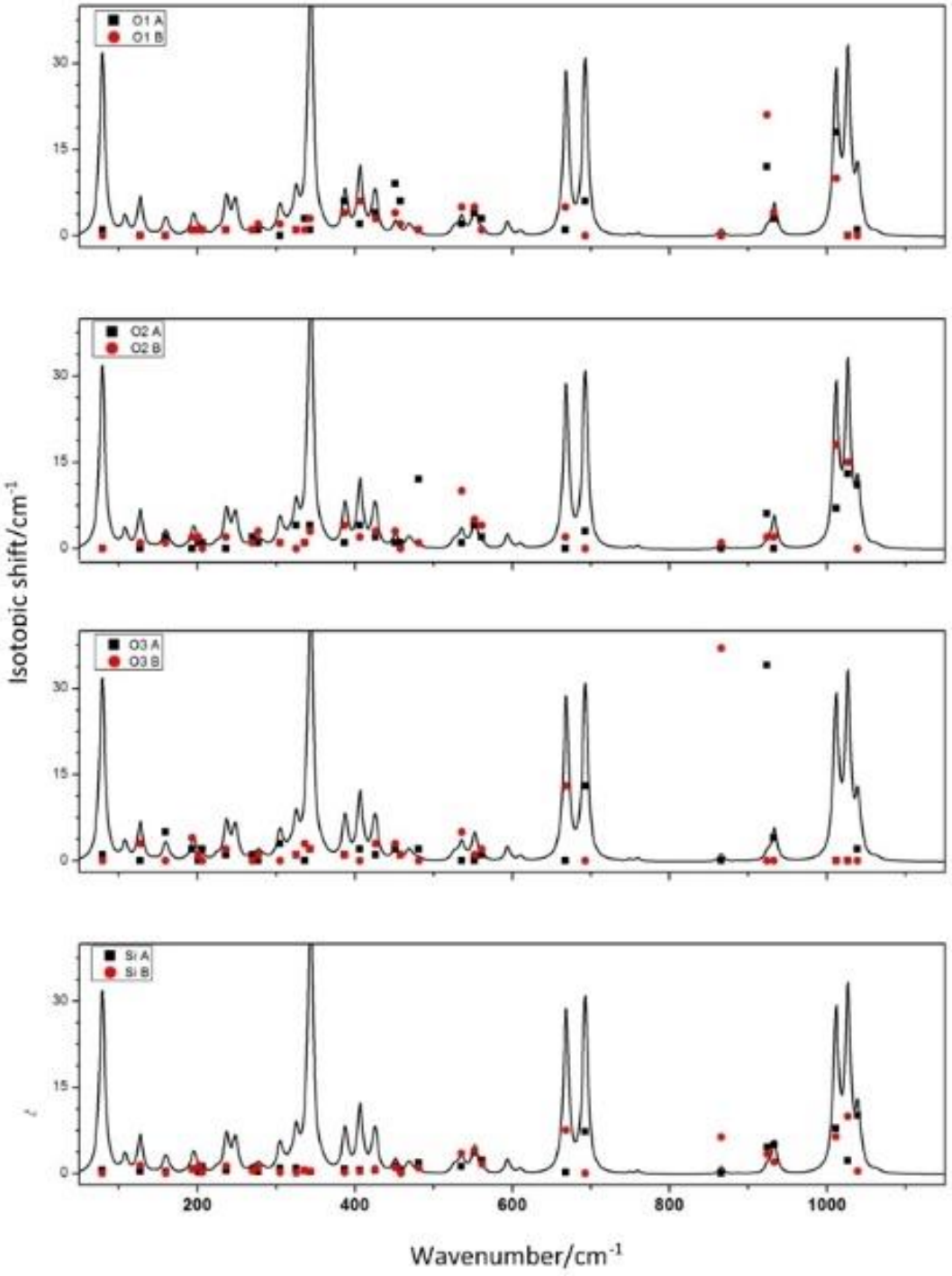

Figure 6: Isotopic shift for oxygen and silicon. The different contribution for the oxygen in the A and B chains calculated by the difference from the position of the peak in orthoenstatite before and after isotopic substitution is reported.

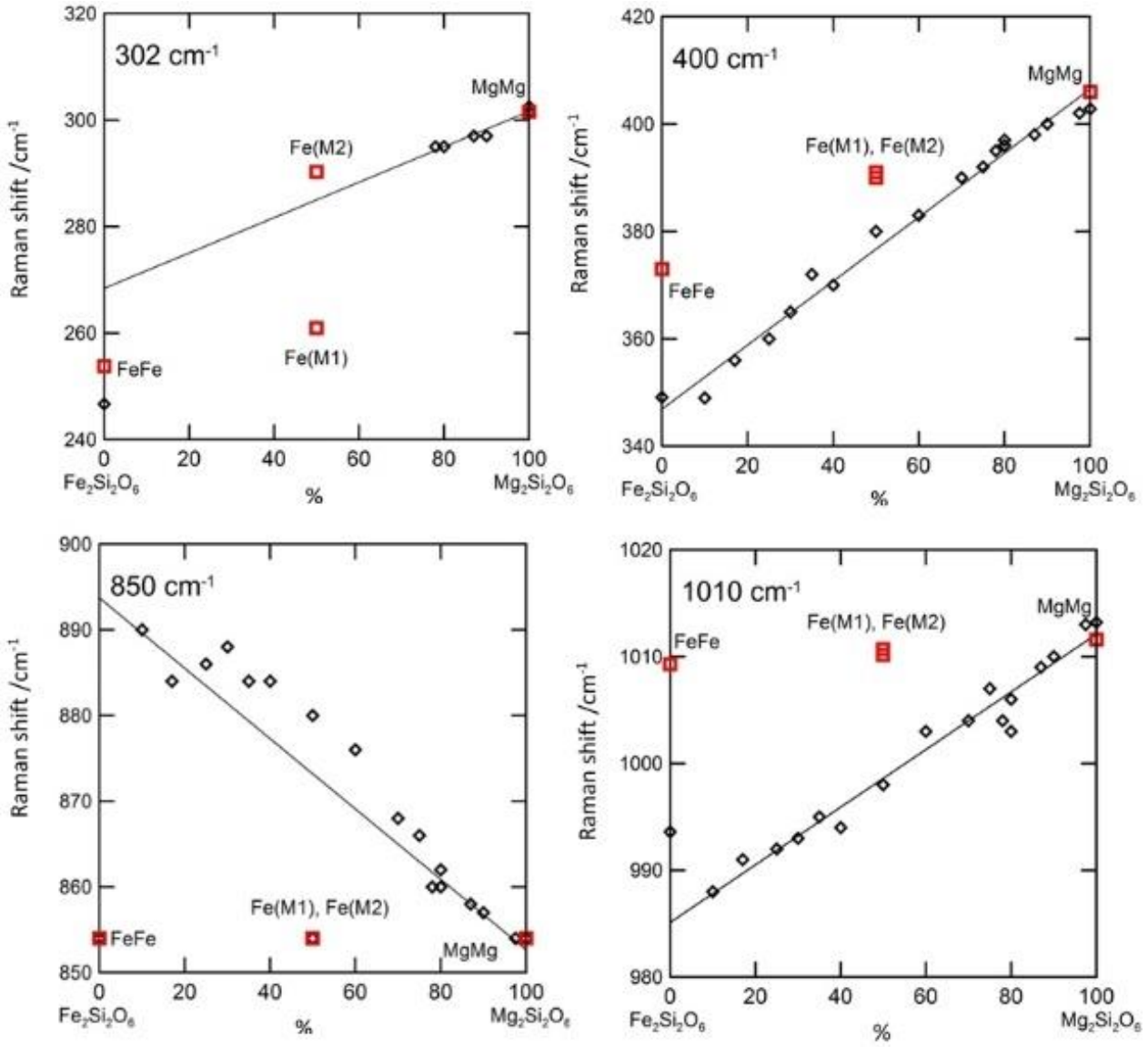

Figure 7: Raman shift versus composition of several modes along the Mg2Si2O6–Fe2Si2O6 series. Squares are the results of mass substitution; diamonds are experimental Raman data.

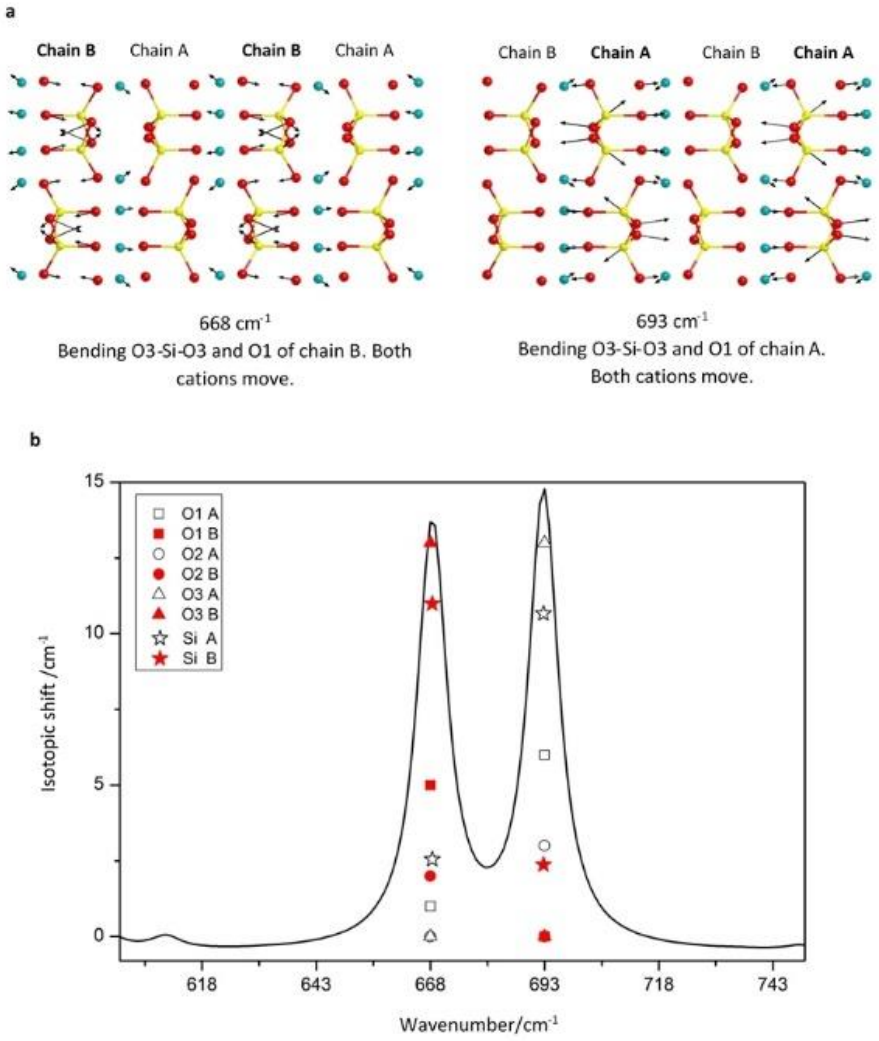

Figure 8: a) Graphical representation of the vibrations for the modes at 668 and 693 cm-1 on [001] plane; b) detailed isotopic contribution for the splitmodes at 668 and 693 cm-1.

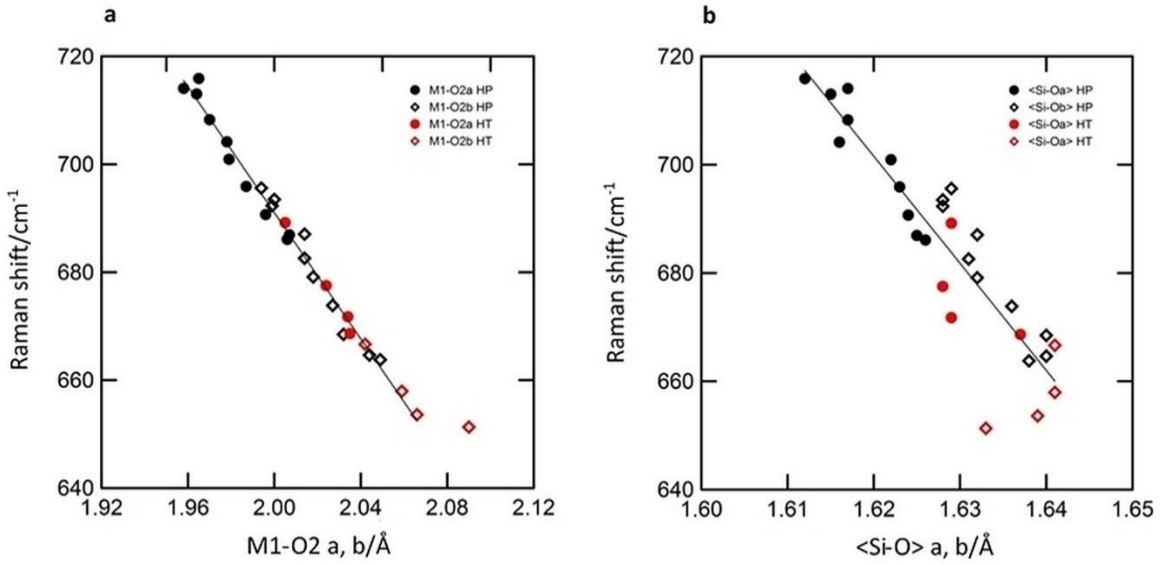

Figure 9: Raman shift and bond distances and angles for the peaks at 664–686 cm-1 with pressure and temperature in orthoenstatite. a) Raman shift versus M1—O2a, b bond distances; b) Raman shift versus<Si—O>a, b tetrahedral distances.

3.2. Forsterite case study

Abstract

In this case of study the full Raman vibrational spectrum of forsterite (Mg_2SiO_4) is computed from first principles, employing a hybrid HF/DFT Hamiltonian (WC1LYP) as implemented in the CRYSTAL14 code, at static equilibrium and at the temperatures of 0K, 300K and 1000K. The simulations are compared to the available literature data, confirming the accuracy of the calculations and also to experimental Raman spectra taken at room temperature on a natural sample of forsterite ($Mg_{1.76}$ $Fe_{0.22}$ SiO_4), in order to test the reliability of the method on a slightly different composition. The comparison with the experimental data at room temperature shows a very good agreement (an average discrepancy of 7 cm^{-1}) and it allows a reliable symmetry assignment of Raman signals to specific vibrational modes.

Spectra are also simulated by changing the mass of the nuclei for each of the six symmetry-independent species within the unit cell in order to quantify the contributions of each elements to the overall vibration. The aim is to relate the major experimental peaks, not only to specific structural features but also to link them to the Raman shifts observed due to both temperature and composition variation.

3.1.3. Results and discussion

The primitive unit cell of forsterite, Mg_2SiO_4, contains 28 atoms, giving rise to 84 normal modes, three of which correspond to pure translations. Under the *Pbnm* space group (n. 62) of the crystal, the vibrational representation Γ_{tot} at the centre of the Brillouin zone may be reduced as follows:

$$\Gamma_{tot}= 11A_g + 11B_{1g} + 7B_{2g} + 7B_{3g} +10A_u + 10B_{1u} + 14B_{2u} +14B_{3u}$$

where the three translations are not taken into account. The 36 Raman active modes have either A_g or B_{1g}, B_{2g} and B_{3g} symmetry. All the calculated frequencies with their relative symmetry are listed in Table 10, where are also reported frequencies and symmetry of volume cells calculated at 0K, 300K and 1000K including zero point effects (for calculations at high temperature see further in the discussion paragraph about Raman shifts due to temperature).

3.2.1.1. Comparisons and symmetry assignment

Forsterite has been extensively investigated by means of Raman spectroscopy, nonetheless, uncertainty about symmetry and mode assignments remain an open issue (more about previous Raman spectroscopy investigations in Chapter 1, paragraph 1.2.2). Data from literature are listed in

Table 11. Here are reported three data sets of wavenumbers taken from previous Raman studies taken on synthetic forsterite from Chopelas (1991), Gillet et al. (1991) and Kolesov and Geiger (2004),in the fourth column are reported wavenumbers from the experimental measurements on the sample studied. Next to each column is reported the Δv (cm^{-1}) resulting from the comparison with the calculated wavenumbers for forsterite, listed in the fifth column. The last five columns report the calculated mass isotopic shifts for Mg in M2 site and isotopic shift of Si and the three O.

The assignment was done by comparing peak positions and intensities, which improves previous assignments based only on the calculated wavenumber, especially for modes at low wavenumbers. The experimental spectrum of forsterite ($Fo_{\#89}$) powder sample is shown in Figure 10, where is compared with the calculated endmember. The box within the figure emphasizes wavenumbers within 150 to 500 cm^{-1}, where a correct comparison can be done with calculations. To note, the spectra modelled is a perfect virtually infinite crystal, and the simulation of an unpolarised spectrum of a powder sample of forsterite will not take into account preferential orientations or grain size effects which could occur in an experimental measure. Peak at 304 cm^{-1} is an example: in measurements, it occurs with higher intensities compared to calculations. This could be due to several reasons, such as crystal powder preferential orientation, compositions or lattice defects.

Concerning literature data, the maximum discrepancies on absolute average is about 7 cm^{-1}, which is within the range of experimental error for each set of experimental data considered. The maximum discrepancy is about -33 cm^{-1}, for the mode at 378 cm^{-1}. However, it is possible to claim a correct assignment of the mode, since the enlarged box in Figure 10 shows a correspondence between the two peaks, taking into accounts intensity, too.

Moreover, it is possible to notice that the general discrepancies are comparable for each set at the same wavenumbers for example: the first wavenumber generally found in literature (Chopelas 1991, Gillet et al., 1991), and also in this study, is about 183 cm^{-1}. In

Table 11, where all of the 36 computed Raman wavenumbers are listed, wavenumbers of about 183 cm^{-1} are indeed calculated, but it has a different symmetry. In literature it is assumed that the first wavenumber found in forsterite has an A_g symmetry, therefore the correct comparison with calculated data will be with the first A_g mode, which is foreseen at 191 cm^{-1}. Another example is certainly the diagnostic peak that is frequently found experimentally around 824 cm^{-1}, but which is calculated at 819 cm^{-1}.

3.2.1.2. Isotopic shift and mode assignment

The spectra after isotopic substitution of the six symmetry-independent atoms in the unit cell were calculated after substitution of ^{56}Fe for ^{24}Mg within the M2 and M1 sites, ^{30}Si for ^{28}Si, and three ^{18}O for the three ^{16}O within the tetrahedron. As remarked in the computational details section, the mass substitution does not involve a recalculation of the energy second derivatives with respect to the positions of the nuclei: indeed, frequencies are recalculated by just changing the masses used to construct the weighted Hessian matrix.

The results, expressed as Raman shift (cm^{-1}), are represented numerically in

Table 11 and graphically in Figure 11 (a and b) the spectra have been divided into two parts to emphasize the peaks at low wavenumbers). By doing so, participation of the substituted atom to the vibration movement; vice versa is signalled by the corresponding frequency shift of the mode itself; a zero frequency shift indicates that the substituted atom is not participating to the mode. It must be noticed that in both table and figures Mg1 is not taken into accounts: cations in M1 do not participate to Raman-active modes. According to selection rules for the corresponding space group of forsterite, Pnma (n.62), listed in Table 12, Mg1, which has the 4a Wycoff position and such position does not contribute to any Raman-active mode.

With this tool is possible to establish the nature of each atomic motion in a given mode. For example, by looking at

Table 11 and in particular the Mg2 column, forsterite spectra can be divided quantitatively in three possible regions, confirming what it is already extensively remarked in literature (for clarity, from now on we are going to refer to calculated wavenumbers). A first one that goes from 191 cm^{-}

^{1} to 351 cm^{-1}, where the Mg (within the M2 site) mainly vibrates with small contributions from oxygens and a negligible contribution from silicon (confirming what in literature is defined as a region of rigid rotation and translation of the lattice, due to SiO_4 and M2 translation) The highest motion of Mg2 is calculated at 351cm^{-1}. Other three high Raman shifts are calculated respectively at 228 cm^{-1}, 304 cm^{-1} and 324 cm^{-1}. These data overlap with Kolesov and Geiger (2004) that, in their experimental isotopes substitution of ^{26}Mg for ^{24}Mg, found the biggest shifts at peak at 304 cm^{-1} and 329 cm^{-1}.

The second region starts about at 400 cm^{-1} up to 644 cm^{-1}. As it could be seen in parallel from Figure 11 a and

Table 11, there is a decrease in the quantity of motion of Mg2 and an increase of oxygens motion. The contribution of silicon remains negligible until around 600 cm^{-1}. In this region, as it is remarked also in literature, motions are mixed, characterized mainly by bending of Mg2 with the oxygens. However, by knowing exactly which element is mainly contributing to the motions and, together with its representations, may lead to a correct assignment of the mode.

The third region, from about 800 cm^{-1} up to about 1000 cm^{-1} is known to be as the part of the spectrum where the tetrahedron SiO_4 has its internal motions, with a negligible contributions of from Mg2 or however negligible. In fact, peak here calculated at 929 cm^{-1}, shows a slight contribution from the Mg2 within the overall motion (Figure 11 b)

In this region, at higher wavenumbers, silicon participates with oxygens at the characteristics symmetric and asymmetric stretchings. By combining the results of isotopic substitution with the direct inspections of the eigenvectors, it is possible to describe the nature of the motion and understand the direction of the motions. As an example, the motions of the characteristic double peak of forsterite, here calculated at 819 cm^{-1} and 857 cm^{-1} is known to be as a stretching of Si-O. By means of the graphic interface software Moldraw

(http://www.moldraw.unito.it/ sgg/f10000.htm) it can been described as a symmetric Si-O2 stretching between Si-O2 for the former peak and as an asymmetric Si-O3 stretching between Si-O3 for the latter one. Some examples and description of the motions of some representative wavenumbers are shown in Figure 12.

3.2.1.3. Si-O stretching modes and Si-O bond distances

Peaks at high wavenumbers seem to be sensitive to temperature and pressure, thus can be linked to the crystalline structure studying Raman shifts. Bond distances of Si-O1, Si-O2 and Si-O3, taken from Kudoh et al. (1985), measured at increasing pressure (here considered from 1bar to 80 kbar), plotted against Raman shifts calculated from Chopelas at the same pressures, are shown in Figure 13. In the figures are shown the trends of just three peaks at high wavenumbers, which are diagnostic for forsterite and in this work are calculated at ambient conditions at 819 cm^{-1}, 857cm^{-1} and 929 cm^{-1} (in figure plotted as stars). The linear fits of the three trends show slightly different slopes for the first two linear fits at 819cm^{-1} and 857cm^{-1} and a much more tilted slope for the peak at 920 cm^{-1}. The reason may be found in bond distances between Si and O within the tetrahedral for forsterite. At ambient conditions we have from Kudoh et al. [33] that the distances are respectively for Si-O2 1.654 Å, for Si-O3 1.635 Å and for Si-O1 1.614 Å.

Those three peaks are shown in Figure 13 and are characterized by the highest contributions in the motion of oxygens, which are respectively O2 for 819 cm^{-1}, O3 for 857cm^{-1} and O1 for 920 cm^{-1}. Therefore, what can be assessed is that shorter bond lengths correspond to higher wavelengths and thus a higher energy, if compared to longer bond distances which are set at shorter wavelengths and thus lower energy.

Table 10 The 36 Raman active modes for forsterite and relative symmetry calculated at static equilibrium and 0 K, 300 K and 1000 K including zero point effects. In the last column are the temperature derivatives.

Static equilibrium		0 K		300 K		1000 K		$(\Delta\nu_j/\Delta T)$
cm^{-1}	symmetry	cm^{-1}	symmetry	cm^{-1}	symmetry	cm^{-1}	symmetry	cm^{-1}/K
191	A_g	191	A_g	187	A_g	181	A_g	-0.010
234	A_g	234	A_g	232	A_g	229	A_g	-0.006
315	A_g	315	A_g	307	A_g	292	A_g	-0.022
336	A_g	335	A_g	328	A_g	313	A_g	-0.022
351	A_g	351	A_g	344	A_g	333	A_g	-0.018
432	A_g	432	A_g	423	A_g	409	A_g	-0.023
556	A_g	556	A_g	553	A_g	548	A_g	-0.008
616	A_g	616	A_g	611	A_g	603	A_g	-0.014
819	A_g	819	A_g	812	A_g	801	A_g	-0.018
857	A_g	857	A_g	851	A_g	841	A_g	-0.016
974	A_g	974	A_g	964	A_g	949	A_g	-0.024
228	B_{1g}	228	B_{1g}	224	B_{1g}	217	B_{1g}	-0.011
263	B_{1g}	263	B_{1g}	259	B_{1g}	250	B_{1g}	-0.013
324	B_{1g}	323	B_{1g}	316	B_{1g}	303	B_{1g}	-0.020
372	B_{1g}	372	B_{1g}	365	B_{1g}	354	B_{1g}	-0.018
392	B_{1g}	393	B_{1g}	389	B_{1g}	383	B_{1g}	-0.009
448	B_{1g}	447	B_{1g}	440	B_{1g}	427	B_{1g}	-0.020
594	B_{1g}	593	B_{1g}	588	B_{1g}	580	B_{1g}	-0.014
644	B_{1g}	644	B_{1g}	638	B_{1g}	628	B_{1g}	-0.016
834	B_{1g}	834	B_{1g}	827	B_{1g}	816	B_{1g}	-0.019
867	B_{1g}	867	B_{1g}	861	B_{1g}	850	B_{1g}	-0.017
986	B_{1g}	985	B_{1g}	976	B_{1g}	961	B_{1g}	-0.024
194	B_{2g}	195	B_{2g}	189	B_{2g}	179	B_{2g}	-0.016
304	B_{2g}	304	B_{2g}	301	B_{2g}	296	B_{2g}	-0.008
327	B_{2g}	327	B_{2g}	320	B_{2g}	308	B_{2g}	-0.018
388	B_{2g}	388	B_{2g}	380	B_{2g}	365	B_{2g}	-0.023
424	B_{2g}	424	B_{2g}	417	B_{2g}	408	B_{2g}	-0.015
605	B_{2g}	605	B_{2g}	601	B_{2g}	594	B_{2g}	-0.011
929	B_{2g}	929	B_{2g}	923	B_{2g}	913	B_{2g}	-0.016
182	B_{3g}	183	B_{3g}	181	B_{3g}	178	B_{3g}	-0.005
257	B_{3g}	257	B_{3g}	251	B_{3g}	242	B_{3g}	-0.015
331	B_{3g}	331	B_{3g}	323	B_{3g}	308	B_{3g}	-0.023
378	B_{3g}	378	B_{3g}	373	B_{3g}	364	B_{3g}	-0.014
455	B_{3g}	455	B_{3g}	447	B_{3g}	434	B_{3g}	-0.021
603	B_{3g}	603	B_{3g}	599	B_{3g}	593	B_{3g}	-0.009
886	B_{3g}	886	B_{3g}	880	B_{3g}	869	B_{3g}	-0.017

Table 11: Comparison of wavenumbers ν (cm-1) from literature with calculated (at static equilibrium) and relative discrepancies Δν (cm-1). In the last five columns are listed the calculated isotopic shifts for the six symmetry-independent elements within the unit cell. Mg1 is not taken into accounts, because it is not Raman active (see text table 5 and text for explanations). At the bottom are reported the mean values of the absolute discrepancy <|Δν|>, the maximum discrepancies Δνmax and the minimum Δνmin

Chopelas (1990)		Gillet (1991)		Kolesov & Geiger (2004)		this work experimental		this work calculated		Calculated isotopic shift cm^{-1}				
ν (cm^{-1})	Δν	ν (cm^{-1})	Δν	ν (cm^{-1})	Δν	ν (cm^{-1})	Δν	ν (cm^{-1})	Symmetry	Mg2	Si	O1	O2	O3
183	8	183	8	184	7	187	4	191	A_g	46	1	1	0	4
227	1	232	-4	227	1	225	3	228	B_{1g}	51	3	2	1	2
244	-10	244	-10	243	-9	240	-6	234	A_g	43	3	0	2	4
306	-2	307	-3	304	0	304	0	304	B_{2g}	46	1	1	9	6
-	-	-	-	316	-1	317	-2	315	A_g	29	2	4	5	1
-	-	-	-	329	-5	326	-2	324	B_{1g}	46	2	3	0	8
331	5	334	2	-	-	-	-	336	A_g	20	0	1	0	6
341	10	341	10	-	-	-	-	351	A_g	59	1	6	0	4
376	-4	376	-4	373	-1	372	0	372	B_{1g}	12	0	11	1	9
411	-33	414	-36	409	-31	409	-31	378	B_{3g}	17	0	15	4	2
424	0	426	-2	421	3	419	5	424	B_{2g}	11	0	6	12	15
434	-2	-	-	434	-1	434	-1	432	A_g	0	1	2	0	7
441	7	443	5	-	-	-	-	448	B_{1g}	16	0	1	15	24
545	11	548	8	544	12	544	12	556	A_g	2	3	5	3	18
585	9	585	9	588	6	587	7	594	B_{1g}	13	2	5	4	19
-	-	593	10	-	-	-	-	603	B_{3g}	8	2	7	13	10
609	-4	610	-5	608	-3	607	-2	605	B_{2g}	1	1	6	13	10
826	-7	825	-6	824	-5	824	-5	819	A_g	0	7	5	31	5
-	-	-	-	838	-4	-	-	834	B_{1g}	1	8	5	30	7
856	1	856	1	856	1	856	1	857	A_g	0	4	9	0	28
-	-	-	-	866	1	-	-	867	B_{1g}	3	4	11	0	25
884	2	882	4	882	4	882	4	886	B_{3g}	0	13	0	0	27
922	7	920	9	920	9	919	9	929	B_{2g}	3	14	1	0	26
966	8	967	7	966	8	962	12	974	A_g	0	14	21	1	5
<|Δν|>	7		8		6		6							
max Δν	-33		-36		-31		-31							
min Δν	1		1		0		0							

Table 12: Symmetry analysis of the normal modes for forsterite, space group Pbnm.

Atom	Wycoff symbol	Representation	Fractional coordinates (Hazen et al. 1976)	A_g	B_{1g}	B_{2g}	B_{3g}
Mg1	4a	0, 0, 0	0, 0, 0	·	·	·	·
Mg2	4c	x, y, 1/4	0.9915, 0.2774, 0.25	2	1	2	1
Si	4c	x, y, 1/4	0.4262, 0.0940, 0.25	2	1	2	1
O1	4c	x, y, 1/4	0.7657, 0.0913, 0.25	2	1	2	1
O2	4c	x, y, 1/4	0.2215, 0.4474, 0.25	2	1	2	1
O3	8d	x, y, z	0.2777, 0.1628, 0.0331	3	3	3	3

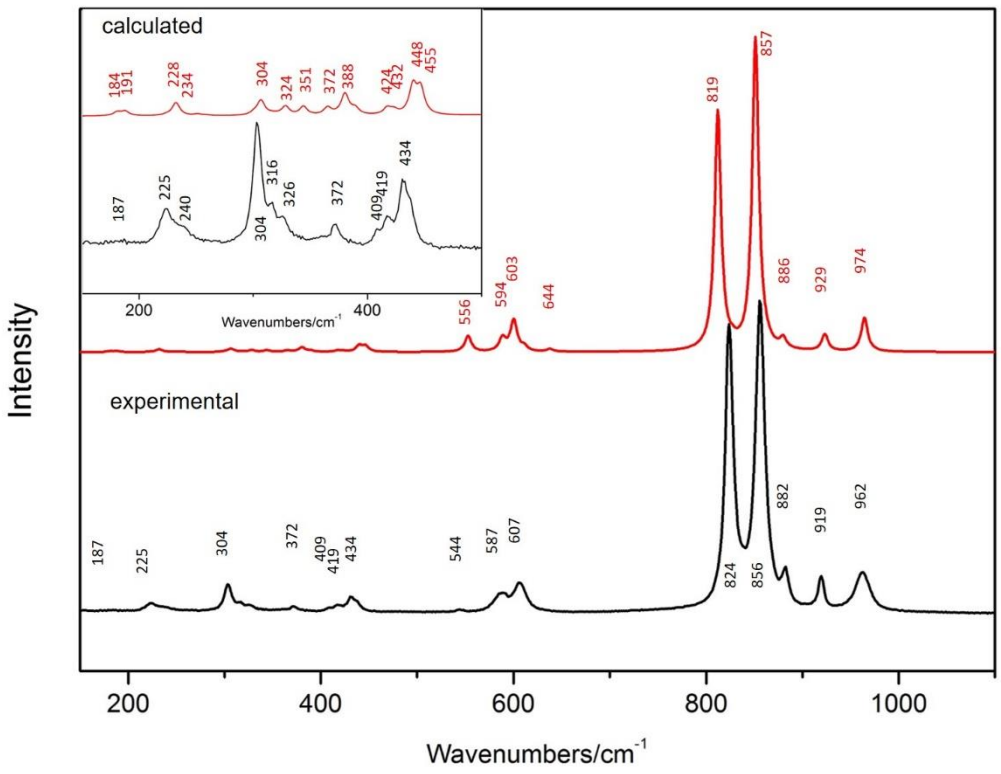

Figure 10: Comparison between a natural sample of forsterite (Fo#89) unpolarized Raman spectrum (bottom) and a calculated forsterite Mg2SiO4 by means of CRYSTAL14 (top). The box at the top on the left is an enlargement of wavenumbers from 150 to 500 cm-1 to emphasize peaks at low-wavenumbers.

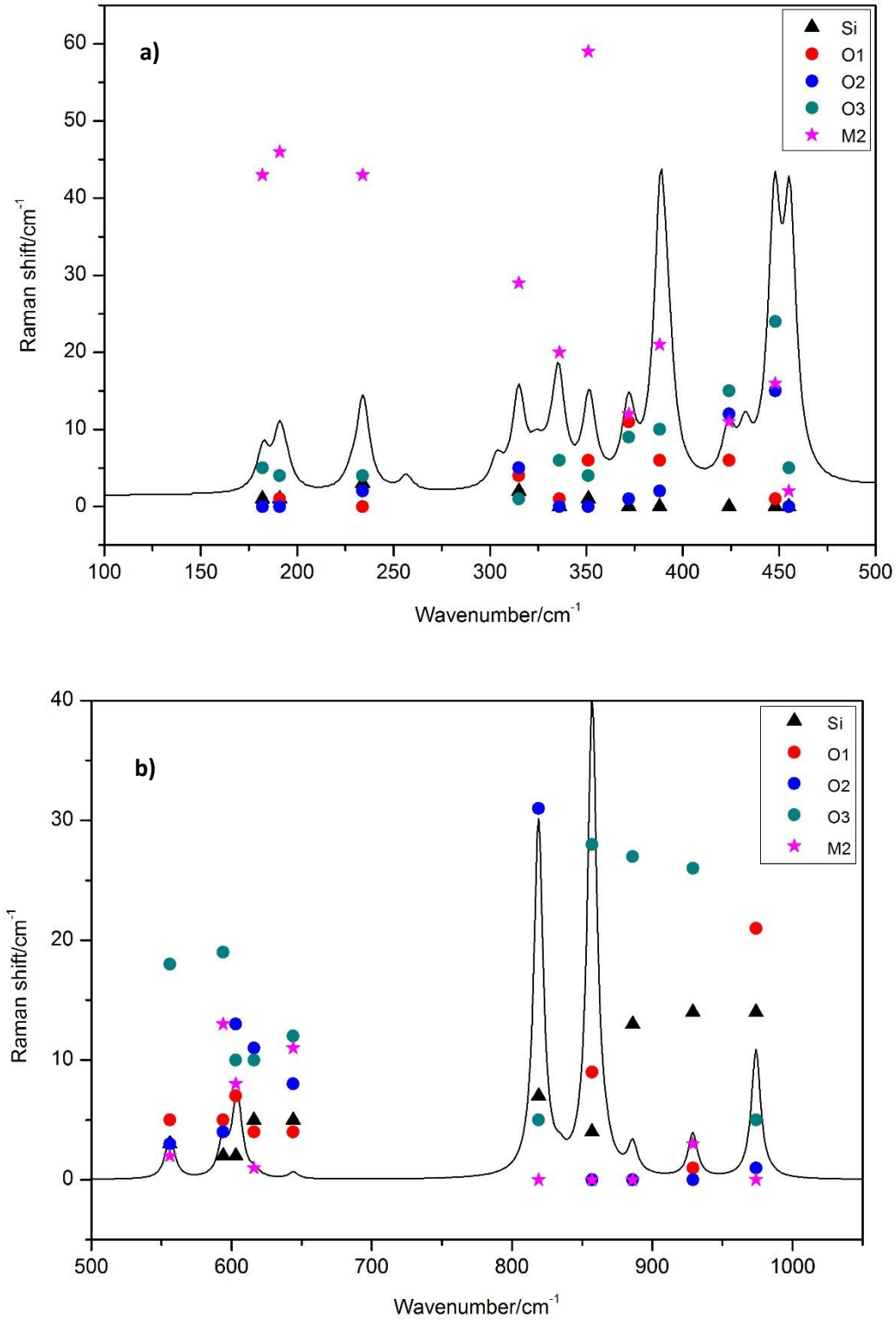

Figure 11: Mass and isotopic shifts of the six symmetry independent ion of the unit cell (56Fe for 24Mg within the M2 and M1 sites, 30Si for 28Si, and 18O for three 16O within the tetrahedron). The larger shift the larger is the contribution of the element to the overall vibration. The spectrum has been divided in two a) to emphasize shifts at low wavenumbers from 150 cm-1 to 500 cm-1, b) from 500 cm-1 to 1050 cm-1.

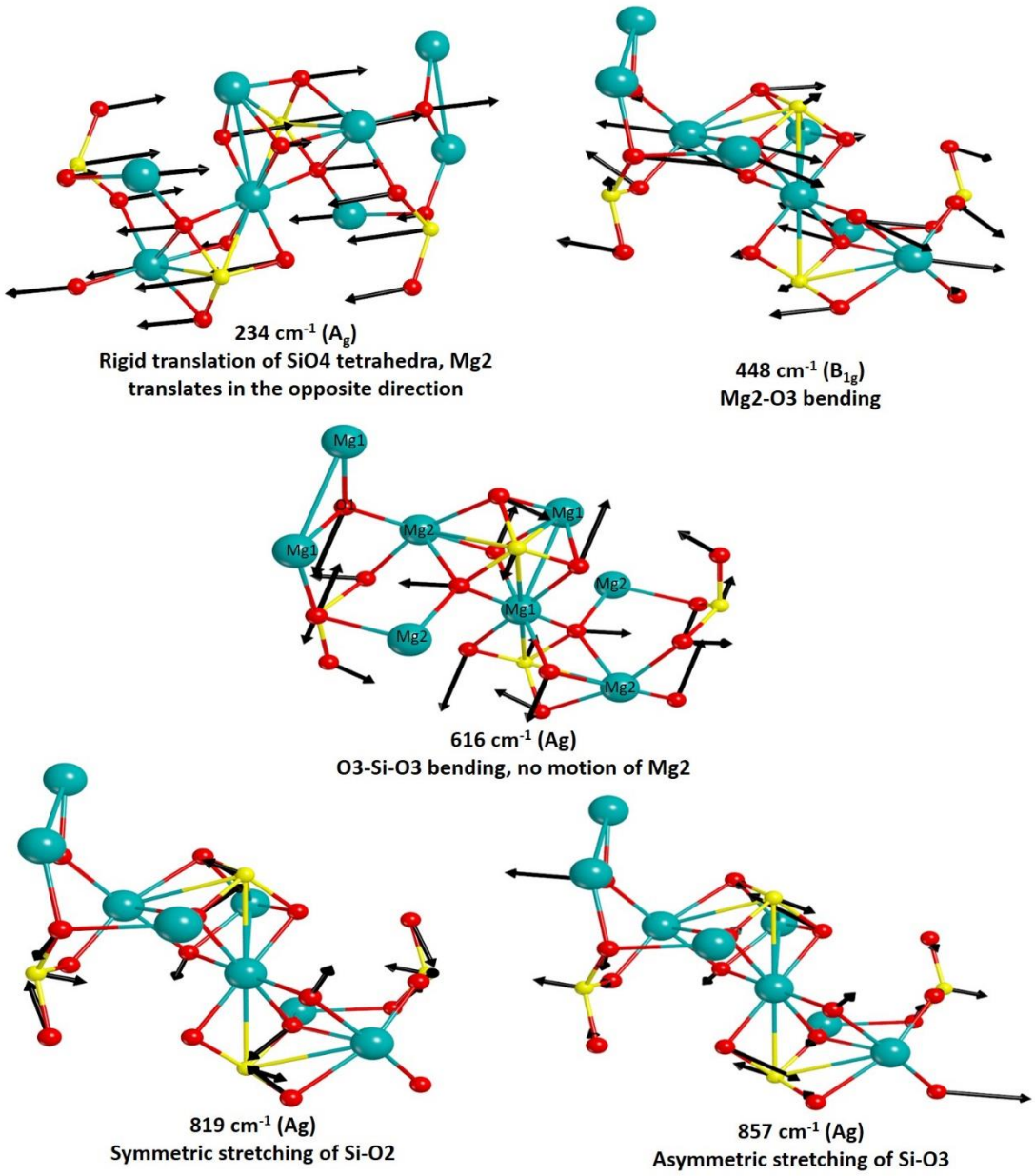

Figure 12: Graphical representation of the direct inspection of the eigenvectors of the calculated phonon frequencies by means of the graphic interface software Moldraw (http://www.moldraw.unito.it/_sgg/f10000.htm). It has been possible to attribute to the most frequently observed peaks of fosterite a mode assignment.

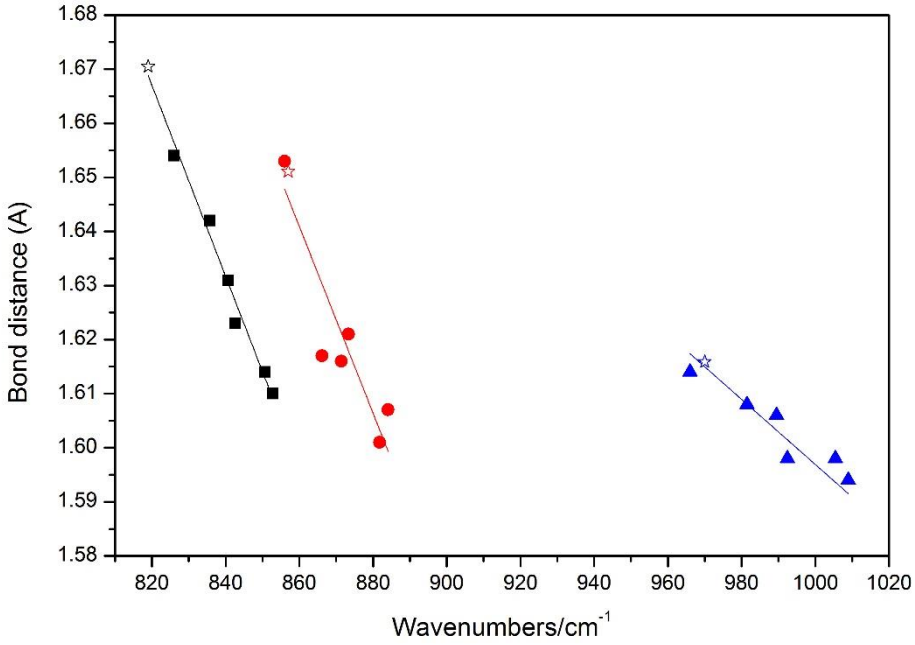

Figure 13: Linear fits of Bond distances of Si-O1, Si-O2 and Si-O3, taken from Kudoh et al. [33], measured at increasing pressure (here considered from 1bar to 80 kbar), plotted against Raman shifts calculated from Chopelas at the same pressures. Here are shown the trends of just three peaks at high wavenumbers, which are diagnostic for forsterite and in this work are calculated at ambient conditions at 819 cm-1, 857cm-1 and 99299 cm-1 (in figure plotted as stars).

3.3. Conclusions

The simulation of the Raman spectra provided by HF/DFT hybrid Hamiltonian, is very close to the experimental spectrum, both in peak position and intensities. It shows that quantum mechanical modelling can be used to interpret the observed experimental spectra and find links between crystal structure and spectroscopic feature. Further, the simulation provides a theoretical framework in which it is possible to model the observed spectra, especially in complex cases such as that of orthoenstatite.

We have shown that quantum mechanical calculations, combined with a careful description of the modes and exploiting some computational tools of CRYSTAL14 (i.e. isotopic substitution or building units decomposition), enable to assess the correlation of bond distances and cation masses with the frequency of a given mode. Therefore, we could relate the structural changes with pressure, temperature and composition to those observed at the same conditions for some interesting modes.

On the other hand, atomic masses and bond distances are related to the composition and provide a preliminary clue for the modes most affected by cation substitution. For instance, we have found that in orthopyroxenes there are peaks most sensitive to the exchange of Fe and Mg between the M1 and M2 sites, which orthoenstatite the peak at 866 cm^{-1}, even relatively minor changes in the tetrahedral bond distances, (T-O3) between enstatite and ferrosilite, promote significant changes in Raman peak positions. This again, can be related to atomic composition, for instance makes Raman spectroscopy a potential probe for a site specific compositional determination, i.e. a probe for intracrystalline ordering.

Moreover, as seen in the case of olivine where the combinations of modes hinder a proper mode symmetry attribution, the simulation of the spectra could be a reliable tool for mode assignment of experimental spectra, even if the composition of the sample measured is not the one of the endmember calculated.

We believe that our approach of combining experimental structural data and *ab initio* calculation can be employed also in other minerals and mineral families, providing theoretical basis and hints for future experimental Raman investigations and applications to mineral sciences.

Chapter 4

Modelling of high temperature TIR spectra for Mercury remote sensing

This chapter is dedicated to a possible application of the calculated-experimental approach to planetary spectroscopy and in particular to remote sensing spectroscopy. As said previously, *ab initio* calculations can simulate extreme temperature variations, which could be very common studying rocky planets or asteroids. Considering a rocky planet like Mercury, which is the closest planet to the Sun, an extremely wide range of temperature affects the planetary surface. The closeness to the Sun and the slow rotational motion makes a given point heated for as much as 88 days. This causes, together with the lack of stabilizing atmosphere, a temperature variation that can go from 70 to about 700K, at different latitudes (Strom and Sprague, 2003).

The change in temperature induces a variation in the density of the rocks on the surface of the planet, in turn related to changing bond distances and angles of the minerals (Christiansen et al 2000, Koike 2003). A significant change in the vibrational behaviour is therefore observed with temperature. The interpretation of thermal emissivity spectra becomes then extremely challenging, unless the effect of temperature is properly modelled.

In the following paragraphs, experimental thermal emissivity spectra are studied with an innovative approach: modelling TIR spectra, with *ab initio* methods, one of the two main mineral families (olivine and orthoenstatite) that presumably compose the surface of Mercury and then comparing the calculated TIR spectra with the high temperature laboratory measurements. The aim is to compare the experimental data with modelled TIR spectra at high temperature, to understand which IR frequencies are influenced by temperature that occurs during the insolation of the surface and which not, and to provide a theoretical background for the systematic interpretation of the experimental data, (laboratory and remote sensing). A further goal is to interpolate and link the band shifts due to temperature to the mineralogical structure, on view of the interpretation of the data that will be acquired by MERTIS instrument (Hiesinger and Helbert 2010).

This chapter starts with a quick overview on spectroscopy applied to planetary science and in particular to remote sensing for Mercury's surface investigation. Then the focus will be on the methodological procedure that allows the modelling of high temperature TIR spectra, and on the comparison between modelling with experimental measurements; results, strengths and weaknesses of the approach will be discussed with the aim of a possible application in the next space mission to Mercury.

To the author knowledge, this study represent a first example of simulated IR spectra at high temperature and a comparison with emissivity spectra.

4.1. Remote sensing and thermal emissivity spectroscopy

The identification of minerals that constitute the planet surface is the basis for any geological map of the planet, and it is a step required to unravel the story of the planet, its formation and dynamics. Virtually everything we know about the surfaces of the various bodies of the solar system comes to us through remote sensing. Most spacecraft missions are flybys, and even landers, manned or unmanned, can sample only very small portions of the surface of the body they are investigating. Also, the study of processes on the surface of the Earth includes remote sensing: the study of the Earth from balloons, aircraft, and satellites. (Hapke, 1993)

To give a simplified definition of remote sensing for a planetary surface, we can say that it is the study of how light is emitted and scattered by particulate media, such as planetary regoliths, clouds, or even powders in the laboratory. Being more formal, remote sensing can be define as a spectroscopy that investigates the diffuse scattering and thermal emission of electromagnetic radiation which interact with discrete particles. Those particles may differ in composition, associated with distinct spectral characteristics. The minerals and the chemical content of solid matters can be determined by the analysis of their spectral features, as the spectral signatures of minerals are intimately related to the crystal structure and they represent a remote sensing mode to determine the surface composition.

Fundamental vibrations of atoms in the crystal lattices of most minerals absorb incident electromagnetic energy at frequencies which coincide with the middle, or thermal IR portion of the electromagnetic spectrum (greater than 5 μm). Within this wavelength range, virtually all minerals have a unique set of spectral absorption features that allow them to be distinguished. Thus, the

Thermal IR (TIR) region of the spectrum is excellent for examining pure samples as well as mineralogically complex geologic materials (i.e., rocks). (Salisbury et al., 1987, Hamilton 2000)

In the analysis of TIR spectra one should know whether they come from a reflection or emission process.

Reflection refers to a process whereby incident light is returned from a material's surface. In reflection spectroscopy, the material of interest, typically an optically thick particulate or solid sample, is illuminated with an infrared light source; the ratio of the amount of reflected to incident light yields a spectrum, reflectance, with maxima in the locations associated with molecular vibrations. Reflectance, depends on the thickness of the material, usually the percentage of light reflected from an optically thick material is described most accurately as its reflectivity. However, in much of the spectroscopy literature such spectra are presented as percent reflectance.

Emission refers to the energy radiated from a material. Measurements of emission do not utilize an external light source, but instead passively measure the wavelength-dependent emitted infrared radiance of the sample (i.e., the sample is the source), which may be a particulate or solid.

Emissivity is defined as the ratio of the energy emitted from a material to that of a blackbody (perfect emitter) at the same temperature and has unit less dimensions from 0 to 1. The emission is reduced at frequencies where the material is strongly absorbing and the features of interest in an emissivity spectrum are minima (emissivity is the term most commonly used in the literature and it is used here). (Hamilton 2010, Lane 2011).

Reflectance and emittance are close within TIR region. In **Figure 14** the spectrum of sunlight reflected from a surface with a diffusive reflectance of 10% is compared with the spectrum of thermal emission from a black body in radiative equilibrium with the sunlight, at various distances from the sun. Clearly, thermal emission can be ignored at short wavelengths, and reflected sunlight at long, but at intermediate wavelengths in the mid-infrared the radiance received by a detector viewing the surface includes both sources. (Hapke, 1993)

Reflectance and emissivity spectra are inverses of each other (E=1–R), according to Kirchhoff's law (Nicodemus, 1965). However, this is strictly true only for cases where the reflectance spectra are measured such that the solid angle of the measurement is low enough to exclude grazing and near-grazing angles (angle between the incident light and the surface also known as glancing angle) of incidence and collection. Grazing angles may be physically blocked (Salisbury et al., 1991a) or they

can be avoided by the use of an integrating sphere that permits the measurement of directional hemispherical reflectance (Salisbury et al., 1991a).

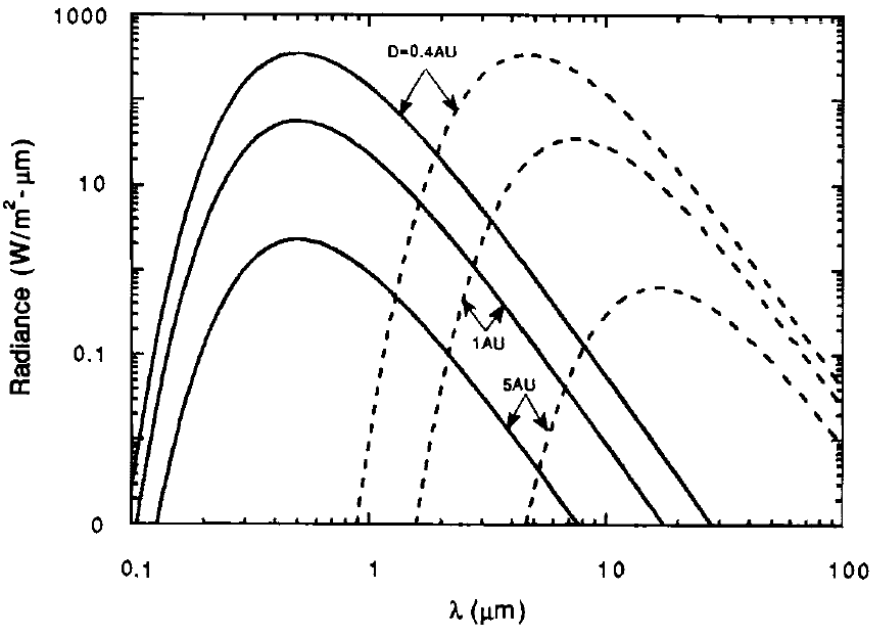

Figure 14: comparison of sunlight reflected (solid line) from a surface with a diffusive reflectance of 10% (albedo of 0.1) with the radiation emitted (dashed lines) from a surface with an IR emissivity of 1.00 for three different distances from the sun. (From Hapke 1993)

4.2. Temperature factor

In most remote-sensing measurements absorptions bands can be detected only through their effects on the radiation that is thermally emitted by the planetary surface being studied. (Hapke, 1993)

Considering a planet as Mercury, an extremely wide range of temperature variations affects the surface. An increase in temperature up to 625K can be locally found: the closeness to the Sun and the slow rotational motion makes a given point heated for as much as 88 days and on the night side for the same period. This causes, together with the lack of stabilizing atmosphere, a temperature variation that can go from 70 to about 700K, at different latitudes (Strom and Sprague, 2003). These temperature variations significantly affect the crystal structure and density of minerals and, at the same time, affect the TIR spectral signature of each single mineral present on the surface of the

planet. This behaviour has been recently demonstrated for plagioclases and olivines, which show significant TIR spectral signature changes under the typical temperature variation of the surface of Mercury (**Figure 15**) (Helbert and Maturilli 2009; Helbert et al. 2013), and could be predicted for other silicates. From a structural point of view, these temperatures changes induce variations of bond distances and angles of the minerals, and of the density rocks on the surface of the planet. A significant change in the vibrational behaviour is also observed.

The thermal behaviour of solids, in fact, is closely related to the vibrational frequencies: the thermal expansion can be viewed as the consequence of the pressure exerted by the gas of phonons that is created in a crystalline solid, according to the temperature.

The temperature variation also affects the interpretation of thermal emissivity spectra, which appear extremely challenging to unravel, due to the broadening of the bands which is observed at high temperature.

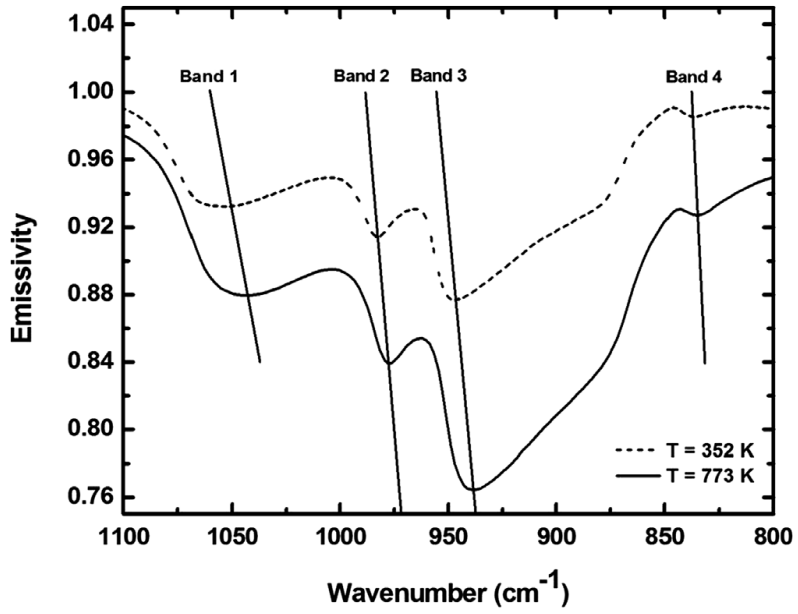

Figure 15: Emissivity TIR spectra for Fo_{92} olivine between 1000 and 800 cm^{-1} collected invacuum at two different temperatures: dashed curve at 352K and solid curve at 773K; straight lines capture the positions of the emissivity minima and display their

4.3. Mercury's mineralogical framework

Mercury is the innermost and the more peculiar planet of Solar system. Even if it is not extremely far for space explorations, it is not yet completely known. Since ancient times, its closeness to the Sun complicated its observations from Earth. Nonetheless, it was already known from the past that

its synodic period is 115 days long, that its spin velocity around the sun is high and that it shows phases, like the moon and Venus.

A new era of planet explorations started in the 1960, when modern ground based telescope allowed to draw the first detailed map of the planet. Until now just two space explorations have been devoted to Mercury: the spacecrafts Mariner10 in 1973, and MESSENGER in 2004, both Americans. The next mission is due on 2018 and it will be the mission BepiColombo, a collaboration between JAXA and ESA for, aimed to provide the answerless questions that are still around the planet.

The outcomes of previous ground-based MIR observations revealed that the surface of Mercury is heterogeneous even at a low resolution. Emissivity spectra show the presence of Fe-poor pyroxenes and olivine and feldspars. In particular, with the aid of comparisons with experimental laboratory measurements, it was possible to detail the presence of Mg-rich olivine, Ca-rich feldspars, augite, hyperstene, diopside and enstatite (Sprague et al., 1994; Sprague & Roush, 1998; Emery et al., 1998; Cooper et al., 2001, Sprague 2008). However, the lack of instruments capable of covering the TIR range prevented an accurate investigation of the mid-IR wavelengths.

Among the instruments on board of BepiColombo, there will be the Mercury Radiometer and Thermal Infrared Spectrometer (MERTIS) (Hiesinger and Helbert 2010), which will allow to detect thermal emissivity spectra (TIR) within the range of 7 to 14 µm (1400-700 cm^{-1}) and a spectral resolution ranging from 9 to 20 cm^{-1}. Such resolution will allow measuring the typical band features of silicates and to reveal not only those changing with composition, but also those that are strongly influenced by temperature (Helbert et al., 2013). In fact, the presence of a radiometric channel on MERTIS can provide an independent measure of the surface temperature imaged by the spectroscopic channel.

4.4. Experimental

In the next two subparagraphs the methodological procedure (experimental and calculated) carried out in this case of study is explained in order to compare the experimental thermal emissivity spectra with the calculated ones at high temperature.

4.4.1. Thermal emissivity measurements

Emissivity data have been measured at the Planetary Emissivity Laboratory (PEL) within the Planetary Spectroscopy Laboratory (PSL), at the Institute for Planetary Research of the German Aerospace Center (DLR) in Berlin (Maturilli et al. 2008). At Planetary Spectroscopy Laboratory (PSL) emissivity and reflectance measurements are performed to identify mineral structures in the IR spectral region between 50 and 1400 cm^{-1}, which is the fundamental range for distinguish spectral absorption features of silicate, as we said previously (Hamilton 2010).

PSL is currently equipped with two Fourier transformed evacuable Bruker Vertex 80V spectrometers. One of them is connected to a planetary simulation chamber that has the unique capability to heat samples in vacuum to temperatures up to 1000K. The instrument used is a Bruker Vertex 80V, with a liquid nitrogen cooled HgCdTe detector plus a KBr beamsplitter to cover the 1 to 16 µm spectral range, and a DTGS detector plus a Mylar multilayer beamsplitter from 16 to 200 µm. The spectrometer is coupled to an evacuated planetary simulation chamber, having an automatic sample transport system to maintaining the vacuum while changing the samples. Radiance is collected by an Au-coated parabolic 90° off-axis mirror and reflected to the spectrometer entrance port. The sample is heated via a copper induction pancake coil while staying always under 1 mbar of pressure (Maturilli et al., 2016). The instruments setup is shown in **Figure 16**. The calibration body is measured at exactly the same surface temperature as the sample, by having a temperature sensor in contact with the emitting skin layer for each measured sample. Details on the calibration procedure can be found in Maturilli et al., 2016 and references therein.

The emissivity measurements in this have been performed at different temperatures, from 320K up to 900K, with temperature steps of 100K in order to simulate the typical diurnal equatorial temperature variation of the Mercury surface.

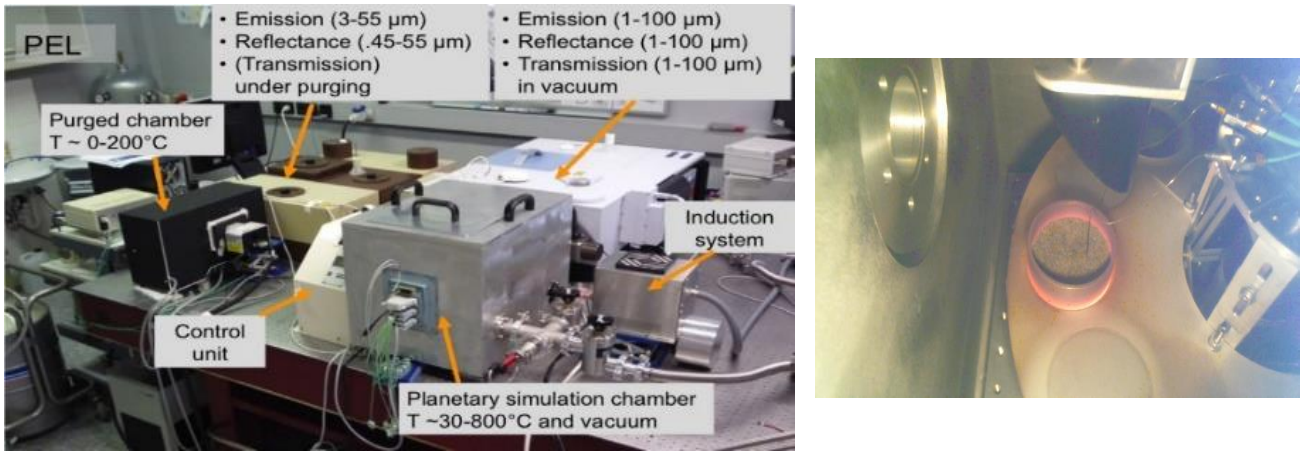

Figure 16: (on the left) PSL instruments setup, (on the right) inside the planetary simulation chamber at 700 K

4.4.2. Samples preparation

The two samples, OLIV89 and OEN87, described and characterized in Chapter 1, have been reduced in a jaw crusher and then sieved under 250µm, allowing us to work very close to the presumable size of Mercurian regolith. The selected particle ranges (125-250µm; <25µm) cannot be totally immune to thermal gradient effects and volume scattering in the TIR range, which should be remarkable in the finest particles (<25µm) of the surface of Mercury proposed in the literature (e.g., Maturilli et al. 2006). These two selected ranges currently represent the most likely particle range identifiable by space mission on the surface of Mercury.

This study just focused on the two extreme grain sizes (125-250µm; <25µm), in order to study the effect due to volume scattering of particles on the measured spectra and mostly to verify which of the two ranges is better comparable with the modelled data.

For these measurements are used 3 to 4 grams of material are used for each size. After the sieving, the produced particulates have been placed into specific stainless steel cups, with a 50 mm internal diameter, 5 mm thick bottom, and 20 mm in height, filling the cups for the first 2 mm, and then

heated in oven at 325 K for almost 12 h, to minimize the presence of intragrain water. The cups were at last placed in a dryer chamber.

The measured emissivity spectra at different steps of temperature and in the two grain sizes are shown in **Figure 18** for the sample OLIV89 and in Figure 22 for sample OENT87, discussions in the text.

4.4.3. Modelled TIR spectra calculated at high temperature

As it has been showed in Chapter 2 with CRYSTAL14 it is possible the simulation of full IR reflectance spectra (for more details on the simulation please go to Chapter 2, paragraph 2.4)
Before showing the results, here are discussed few remarks that enable the comparison of the calculated IR reflectance spectra with a measured emissivity spectra.
First of all, from a mathematical point of you the key quantity for an IR spectra is the complex dielectric tensor $\epsilon(\nu)$. It is a function in which both the real and imaginary parts of $\epsilon(\nu)$ are computed. It can be demonstrated as well that even emission spectroscopy measures both the real and imaginary parts of the complex refractive index (Hamilton 2010). Secondly, as said before, according to Kirchhoff's law ε=1-R, where ε is emissivity and R is reflectance, it is possible to compare IR reflectance with emissivity spectra. According to these statements, the comparison can occur simply transforming the calculated reflectance spectrum into reflectance minus one (1-R).
Of course this is an approximation and usually it is applied to isothermal samples and to samples at the same temperature of the background to which it radiates (Salisbury 2004), a condition that is rarely found. However, Kirchhoff's law is widely used to replace emissivity with reflectance or to compare the two measurements, since reflectance measurements are much easier to obtain than emissivity ones. Recent investigation showed that the approximation holds in bulk samples with larger grain size (Maturilli et al., 2015), becoming less accurate at lower grain size.
In Chapter 2 it has been also shown that, in order to simulate a reflectance spectra, the LO-TO splitting must also be computed. The program allows only the simulation of the IR reflectance of a single crystal along the x, y and z orthogonal directions of a chosen (by the program) cartesian frame. Since emissivity measurements are performed on powder samples, as we have remarked previously, the comparison of the calculate spectra with the experimental emissivity measureshas been performed by doing the weighed mean average of the emissivity spectra calculated for the three x,

y and z directions. This is another approximation, which assume that no preferential orientations are present in the sample simulated. In **Figure** 17**17** three spectra (respectively a calculated, a measured 1-R and a measured emissivity spectrum at room temperature of a natural sample of olivine) are shown with just the intent to remark the reliability of what has been assumed.

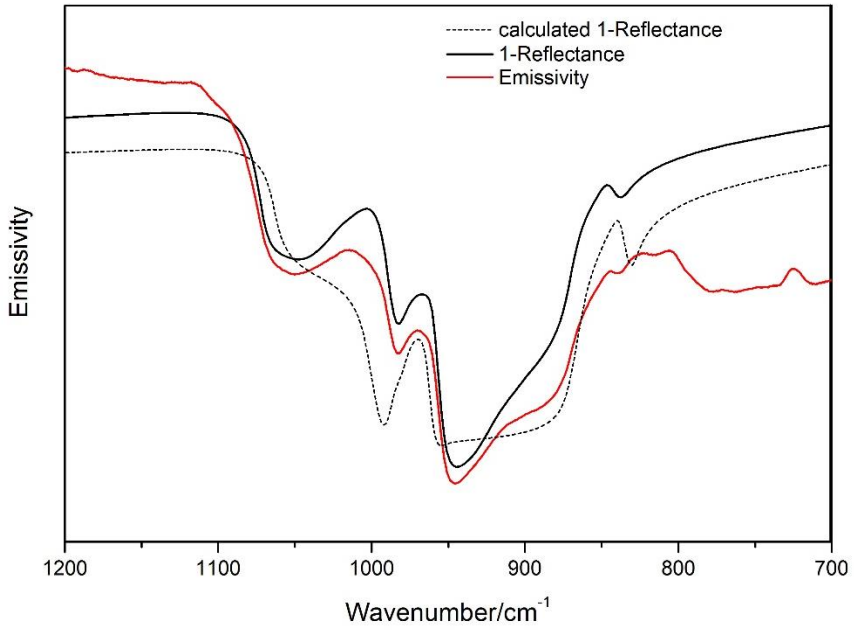

Figure 17: comparison between calculated IR reflectance spectrum, experimental reflectance spectrum and emissivity spectrum of olivine at room temperature applying Kirchhoff's law. Taken from this study.

This procedure has been applied to both the systems investigated, forsterite and orthoenstatite, whose details can be found in Chapter 2. The calculated spectra at different temperature are plotted in **Figure 19** for the former and in **Figure 23** for the latter

4.5. Olivine case study

The approach has been firstly tested on olivine, for three major reasons:

Olivine is a major phase on the surface of Mercury, as Sprague et al. (2009) assumed by means of ground-based mid-infrared spectroscopic measurements of Mercury. Moreover, the presence of

olivine was considered in several petrological models of Mercury (Brown and Elkins-Tanton, 2009; Riner et al., 2010; Sprague et al., 2009; Warell et al., 2010).

Olivine was already extensively investigated by IR spectroscopic studies on single crystal (Servoin and Piriou 1973; Hohler and Funck 1973; Iishi 1978; Hofmeister 1987; Hofmeister et al. 1989; Reynard 1991). Moreover, emissivity and IR reflectance studies regarding the influence of composition as in Hamilton 2010, Lane et al. 2011, have been a precious starting point for this study. Several studies address the temperature effects too, however most of them are focused on the effects at low temperature as in Koike 2006, Koike 2003, Chihara 2001, Bowey 2001.

Forsterite, the Mg endmember of olivine, has been already investigated by means of *ab initio* HF/DFT calculations (Noel 2006, Ottonello 2009, De la Pierre 2011) and pure DFT (Li 2007).

Following as a guideline a previous paper on the high temperature behaviour of a Mg-rich olivine (Helbert et al. 2013), we examine a chemically similar sample (San Carlos, Arizona, $Mg_{1.76}Fe_{0.22}SiO_4$, $Fo_{89}Fa_{11}$). The emissivity is measured for a coarse grain size (250-125 µm) and for a fine grain size (<25 µm) at different steps of temperature (from 320K to 900K).

The IR reflectance spectra of forsterite end-member (Mg_2SiO_4) has been simulated using the Hybrid HF/DFT Hamiltonian WC1LYP, by means of CRYSTAL14, a program for the application of *ab initio* methods to crystalline phases With such methods it is also possible to compute the longitudinal optical-transverse optical (LO-TO) splitting, and hence to simulate reflectance oriented IR spectra of forsterite Mg_2SiO_4 along the *x*, *y* and *z* directions. IR vibrational frequencies have been calculated at 0K, 300K and 1000K, in order to abundantly cover Mercury extreme environment conditions.

Here we discuss a first comparison between calculated and experimental data. We also provide some consideration regarding the emissivity response of the material due to temperature and grain size, in view of remote sensing data interpretation.

4.5.1. Results and discussions

The vibrational frequencies calculated at Γ point at the first Brillouin zone are compared with the existing experimental measures on forsterite (Servion & Piriou 1973, Iishi 1978, Hofmeister 1987, Reynords 1991). In the cited experimental investigations, the positions for the splitting LO-TO peaks are measured on single crystals, allowing a straightforward comparison with our calculated data. The difference between calculated and experimental wavenumbers is on the average of 8-13 cm^{-1}, depending on literature data. The calculated differences in peak position are in most cases due

to a higher value in the calculated spectra; therefore, the most apparent difference is a slight general shift in peak positions. The compared wavenumbers are listed in Table 6, in Appendix section.

No comparison with high temperature peak positions has been done. The only literature data on the peak positions at high temperature on olivine are reported in Ziedler (2015), but the author did not provide information on the LO-TO splitting, necessary for a proper comparison with our calculated ones.

However, the good agreement with the calculated thermal expansion compared with data found in literature (see Table 3, paragraph 2.6, Chapter 2) suggests that our calculation at high temperature is accurate as well.

In **Figure 20**, the experimental spectra at room conditions for the sample with different grain sizes are compared with the spectrum calculated at 300K. Comparing spectral profiles, the differences between experimental data at different grain size are apparent, whereas the calculated spectrum is very similar to the experimental one at coarser grain size (125-250 μm). Moreover, the agreement between the experimental and the calculated spectra remains also at high temperature.

A difference between calculated and experimental spectra exists in band positions, which are downshifted by about 10-15 cm^{-1} below 600 cm^{-1} in the experimental spectrum for each step of temperature. It is likely that this discrepancy is partly or completely due to the compositional difference between the measured $Fo_{\#89}$ sample, and the calculated Mg_2SiO_4 forsterite.

Taking into account the wavelength range (7-14 μm) which will be investigated by MERTIS, we can easily identify in both calculated and experimental spectra six prominent spectral features, whose evolution with temperature can be predicted and modeled. These features are diagnostic within mid-infrared range and can be found in literature (Hamilton 2010, Lane et al. 2011, Helbert et al. 2013). In this work, we can see how these bands shift due to temperature: bands minima shift to higher wavelength (lower wavenumbers) with the increasing temperature and this behavior can be observed in experimental measurements **(Figure 18)** as well as in simulated spectra **(Figure 19).** As shown in **Figure 21** the bands shift trend is rather similar in the experimental and calculated features.

The slope and intercept of the above features are calculated from a linear fit of the frequencies vs temperature of the experimental data, and connecting the calculated 300 and 1000 cm^{-1} data **(Table 13)**. Although a one-to-one relation is not observed, again possibly for the different composition of the experimental sample, the slopes may be compared since they are of the same

order of magnitude, and on average rather close (2.3 vs 1.6×10^{-3} cm^{-1}/K in experimental and calculated spectra).

In this study, for the first time a full IR reflectance spectrum at high temperature of a major phase in planetary bodies, i.e forsterite, is obtained by *ab initio* methods. The calculated spectra match closely with the experimental ones. The compositional differences between our calculated and experimental data can be clearly observed, as well as bulk and grain size effects. The "chameleon-like" effect of olivine, already reported in the previous cited work by Helbert et al. (2013), i.e. the changes in temperature of the spectra similar to those in composition, could be here observed also in the calculated spectra. The spectral features found in IR spectra are foreseen and reproduced in the calculated ones.

The present results show that combined spectral modelling by *ab initio* methods with experimental investigation, provides results, which are both accurate and physically consistent: this method, together with improvements and more precise measurements, may be used as a tool for a better interpretation of data acquired in remote sensing and may lead to the development of new and better models for spectra analysis.

a)

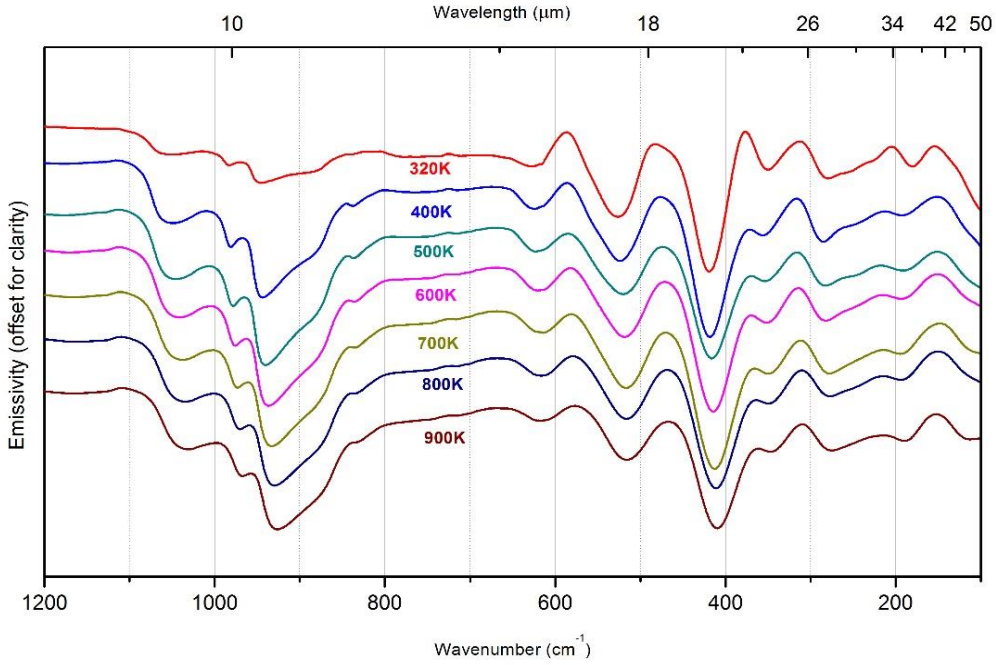

b)

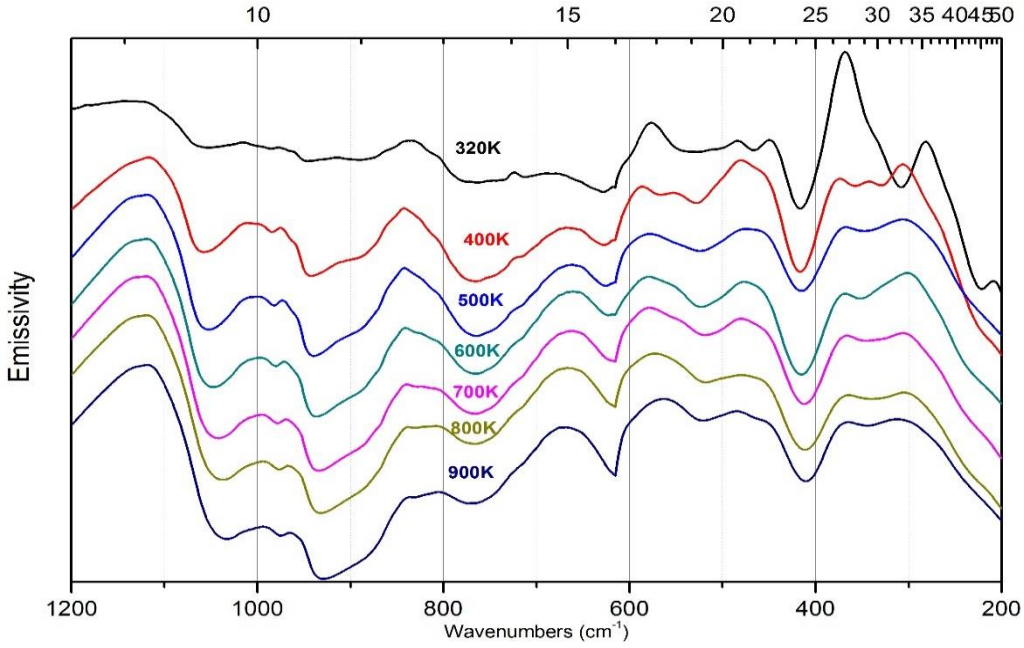

Figure 18: emissivity TIR spectra for Fo89 in both grain sizes: a) 125-250 µm, b) <25 µm

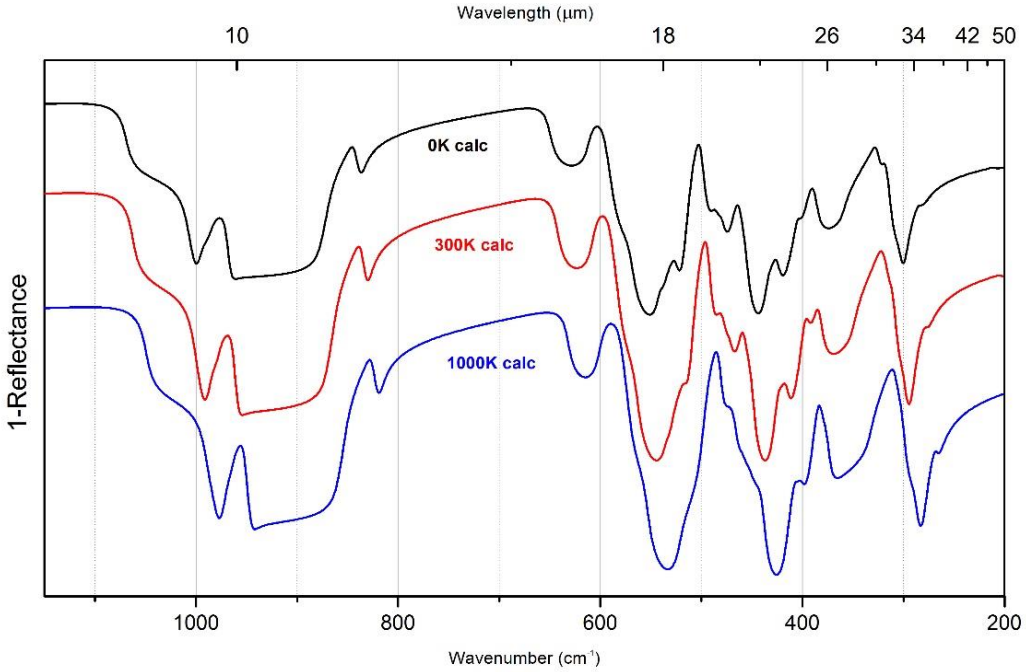

Figure 19: Simulated Reflectance spectra of forsterite calculated at different T (extreme situations). The spectra are the weighted mean average of the three direction x, y and z calculated. More details about calculation methods can be found in the text.

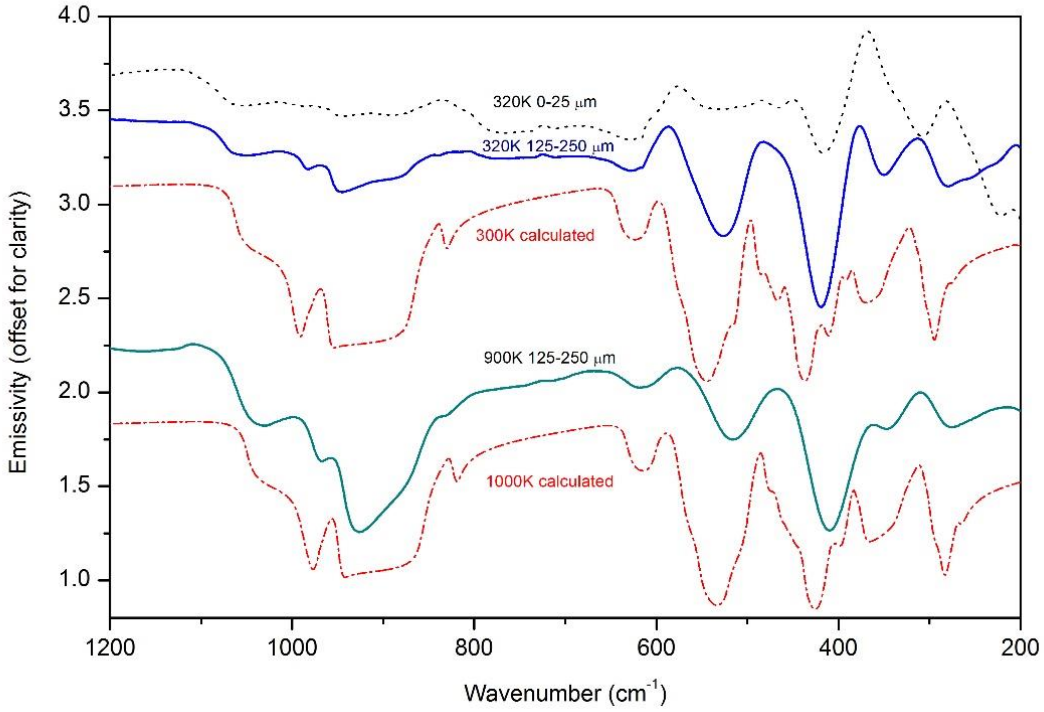

Figure 20: Comparison between calculated 1-R mid IR spectra and experimental emissivity measurements. Solid line: experimental thermal emissivity spectra of Fo89 measured at 320K and 900K (extreme situations). Dotted lines: calculated IR reflectance (inverted) bands of an Mg2SiO4 endmember. Spectra are offset for clarity.

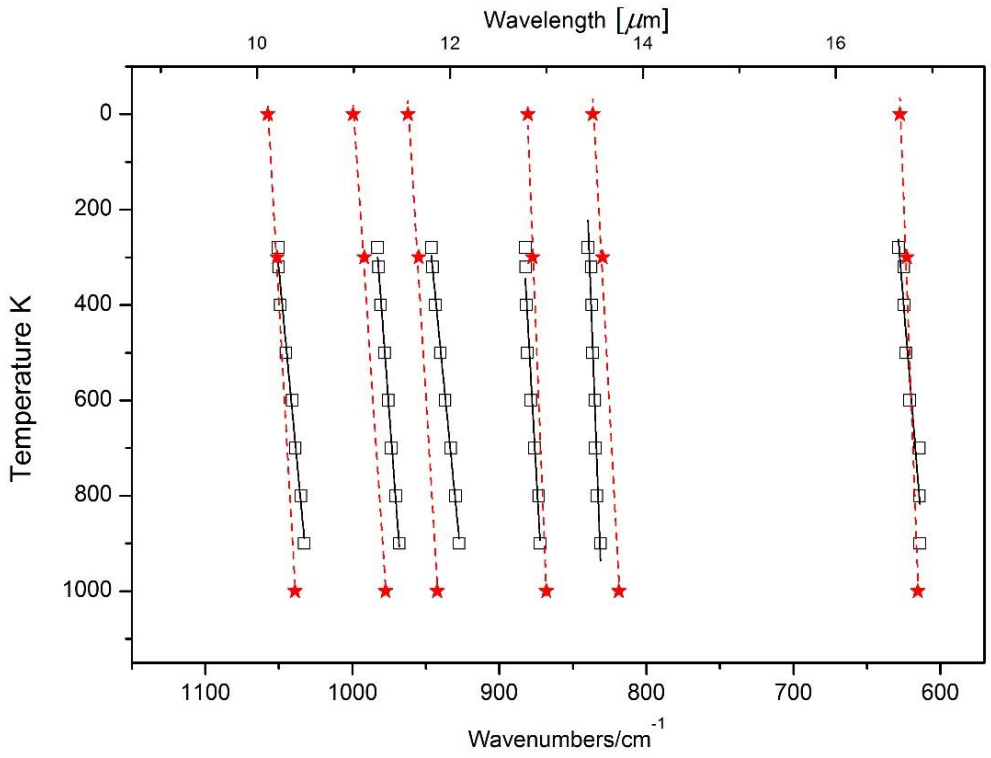

Figure 21: Comparison between calculated and experimental bands minima. Squares are emissivity bands minima measured at different T steps, lines are linear fits to the measured data. Stars are reflectance band positions calculated at 0K, 300K and 1000K, lines are linear fits to the calculated data

Bands	Experimental				Calculated	
	Intercept		Slope		Intercept	Slope
1	1060.5	(8)	-0.031	(1)	1056.4	-0.017
2	990.3	(4)	-0.025	(0)	998.1	-0.021
3	956.2	(5)	-0.032	(0)	960.3	-0.018
4	889	(11)	-0.018	(2)	881.6	-0.014
5	841.2	(7)	-0.01	(1)	834.5	-0.016
6	633.5	(22)	-0.023	(3)	626.1	-0.011
			<-0.023>			<-0.016>

Table 13: The slope and intercept of the bands shift trend calculated from a linear fit of the frequencies vs temperature of the experimental data, and compared with the slope of a line connecting the 300 and 1000 cm-1 data.

4.6. Orthoenstatite case study

Following the previous forsterite case of study, here are presented the results regarding the comparison between the calculated reflectance spectra of orthoenstatite and the thermal infrared spectra of a natural sample of orthopyroxene with the composition of $(Ca_{0.01}Mg_{1.73}Fe_{0.25})Si_2O_6$ are presented. The calculated vibrational frequencies and relative intensities are computed at volume cells corresponding to 300K and 1000K, including zero point effect. Measurements are performed from room temperature to 900K in order to simulate the thermal environment of planet Mercury and the comparisons are performed within the wavelength range that will be investigated by MERTIS (for more details check the previous paragraph).

Here the comparison seems to show less accuracy than the previous example. The calculated thermal expansion appears to be underestimated if compared with data from literature referred to pure othoenstatite samples and several reasons are formulated to justify it (comparisons in paragraph 2.6, Chapter 2). Nonetheless, the qualitative comparisons between the modelled IR spectra and the measured TIR spectra shows a reasonable good agreement within MERTIS wavelength range.

4.6.1. Results

Emissivity spectra measured at different steps of temperatures (from 320K to 900K) show critical absorptions band minima shifted to lower wavenumbers (higher wavelengths), as it shown in Figure 22.

According to the generic description of thermal emissivity spectra of orthopyroxenes, made by Hamilton, they may be broadly described as having Reststrahlen features in the 1200-800 cm^{-1} region, that have the overall appearance of a broad absorption with three separate minima (the central of these three minima has two or four additional superposed minima), and additional Reststrahlen features in the 600-400 cm^{-1} region, which have an overall V-shaped appearance.

In this study, the identifications of critical absorptions (CA) follow the parameters expressed as well in the study by Hamilton (Hamilton 2000). For the identifications of the CAs of the sample the range 1200-400 cm^{-1} has been considered. Within this range 7 characteristic CA have been found, comparable with those found by Hamilton 2000, shown in **Table 14**, where are also reported

the CAs of the sample WAR-2889 from Hamilton 2000, an orthopyroxene with the same composition of the sample here investigated ($Ca_{0.01}$ $Mg_{1.75}$ $Fe_{0.22}$) Si_2O_6. The 7 CAs can be also recognized at each step of the temperature considered.

CA1 is not extremely sensitive to the increase of temperature; in fact, it shows Δλ within the temperature range of 5 cm-1. Temperature effects is more pronounced for CA2 and CA3 where the Δλ is respectively of 12 and 14 cm^{-1}. CA4 follow a similar behaviour of CA1 with a Δλ of 5 cm^{-1}. CA6 is not found within the temperature range considered, but as it shown in Figure 22 band minima are recognizable at the first two steps of temperature 320K and 400K, then the band minima turns into a flat extension of the CA7. Moving towards lower wavenumbers, CA7 shows a Δλ of 10 cm^{-1} and CA8 a Δλ of 13 cm^{-1}.

Concerning the simulated spectra, as explained previously, due to the computational costs, only the two cases at 300K and 1000K have been performed. These spectra are the calculations of reflectance spectra turned into 1-Reflectance for comparisons purpose according to Kirchhoff's law. However, it is foreseen the same behaviour due to temperature: band minima shifts to lower wavenumbers. It is not surprising that the spectra plotted in **Figure 22**, within the mid infrared range considered (1200-200 cm^{-1}) show more detailed spectral features than the experimental spectra. As said before the simulations are the result of the calculations of reflectance spectra of a perfect virtually infinite crystal of orthoenstatite endmember. Nonetheless, it has been possible to recognize 6 of the 7CAs previously explained in this results paragraph.

In fact, the first CAs (from CA1 to CA4) can be easily compared with the experimental, in terms of wavenumbers and Δλ, as it shown at the bottom of **Table 14**

4.6.2. Discussion

A qualitative comparison can be found in **Figure 24** where are compared the calculated and the experimental spectra, taking into account the respectively extreme temperatures considered (300K and 1000K for calculations, 320K and 900K for measurements). According to the forsterite example (chapter 2.1), the best comparison of spectral feature between emissivity spectra and simulated 1-R spectra occurs within the range of 1200-600 cm^{-1}. In fact, within the wavenumbers range considered 1200-400 cm^{-1} a general good agreement can be claimed.

Taking into account the Δλ within the range of temperature considered, there is a comparable behaviour for the first four CAs. In both cases, calculated and experimental spectra, a less sensitive response to the temperature shift for CA1 and C4 as it is shown in table 3 (Δλ of 5 and 5 cm-1 respectively for experimental and a Δλ of 3 and 3 for calculated). On the other hand, CA2 and CA3 are more sensitive to temperature and the CAs have a higher shift in both cases.

At lower wavenumbers (up to 600 cm^{-1}), this agreement does not exist, as figure 3 can easily show. This trend is as well demonstrated by regression linear fit of band minima for each temperature plotted against wavenumbers, **Figure 25**. The first four trends from CA1 to CA4, can be compared also in terms of slope, as it is shown in **Table 15**, where the values of the slopes are within the same order of magnitude.

The reasons why the method here seems less accurate may be several. First of all the comparison has been performed between an orthoenstatite endmember and a sample with a different composition. This may be the reason for the disagreement especially at low wavenumbers, which are mainly due to the bending modes involving non-tetrahedral of cations .

For this reason the work published by Ziedler et al. 2015 was a breakthrough. There, the reflective spectra of a single crystal of pure orthoenstatite are measured at different steps of temperature (from10 K to 928 K, with steps of 100K for each measurement). These data allowed a direct comparisons between the calculated reflective spectra and the measurements of a synthetic sample of orthoenstatite. The comparison, shown in **Figure 26,** exhibits a good agreement, here again mainly within the range of 1200-600 cm^{-1} and at lower temperature (10K and 300K). The comparison at the higher temperature (928K measured versus 1000K calculated), show again considerable shifts between experimental and calculated spectra.

Since the problem has been localized at the higher temperature, the underestimated thermal expansion calculated for the orthoenstatite (results and comparisons of the calculated thermal expansions in table 2, paragraph 2.6, Chapter 2) may be the cause. Indeed the calculations performed for orthoenstatite do not take into account the acoustic branch, since supercell calculations has not been performed. In fact, due to their computational cost and the high number of atoms within the unit cell of orthoenstatite (80 atoms), the vibrational frequencies are calculated for the Γ point only. Therefore, the phonon contribution outside the Γ point is neglected and it has an impact on the estimated thermal expansion.

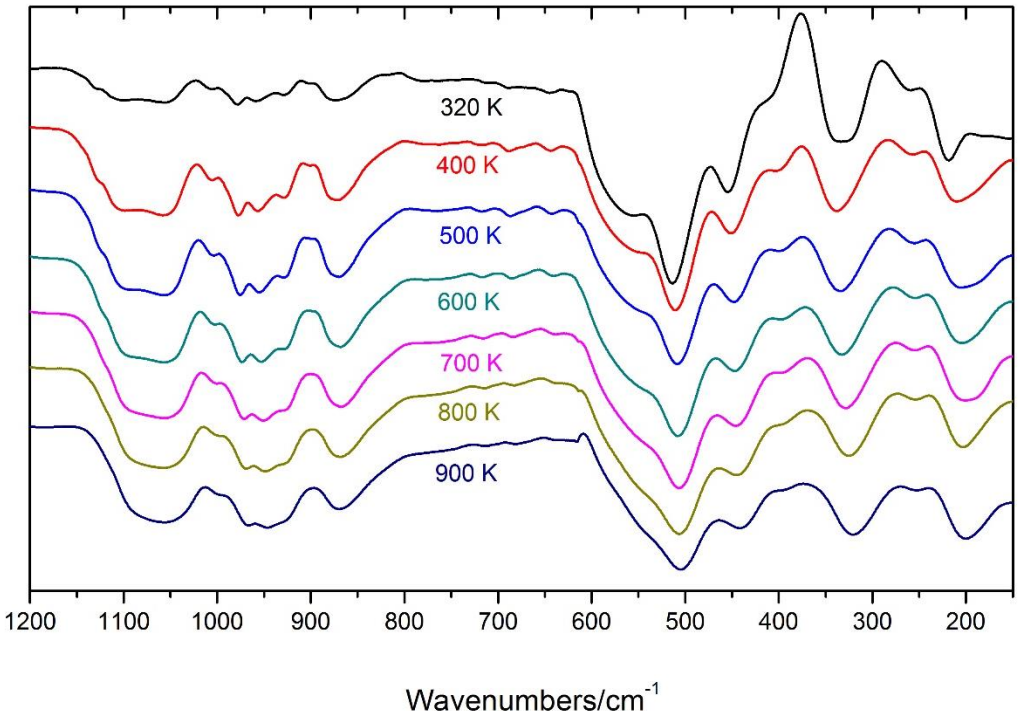

Figure 22: emissivity TIR spectra of orthoenstatite with composition $(Ca_{0.01}Mg_{1.75}Fe_{0.22})Si_2O_6$

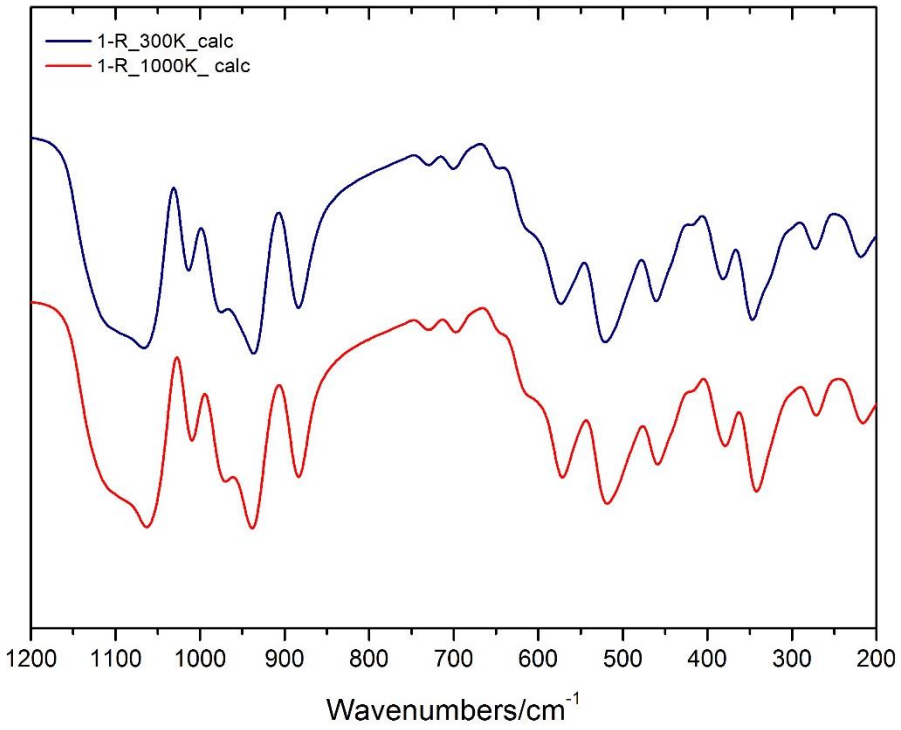

Figure 23: Simulated Reflectance spectra of orthopyroxenes calculated at different T (extreme situations). The spectra are the weighted mean average of the three direction x, y and z calculated. More details about calculation methods can be found in the text

Table 14: Wavenumbers of Critical Absorptions in orthopyroxens function of temperature; top: sample investigated; bottom: calculated. It is also reported a reference sample from Hamilton 2000 measured at room temperature.

T (K)	CA1	CA2	CA3	CA4	CA6	CA7	CA8
sample WAR-2889 from Hamilton (2000)							
RT	1053	979	958	874	547	514	451
This sample							
320	1057	978	961	873	559	514	454
400	1058	978	960	872	554	510	451
500	1057	976	954	870		508	448
600	1054	974	952	868		508	447
700	1053	972	951	868		506	446
800	1052	970	949	868		506	442
900	1052	966	947	868		504	442
Std. Dev	2.5	4.3	5.2	2.1		3.1	4.6
Δλ	5	12	14	5		10	13
Calculated							
300	1065	976	956	887		518	462
1000	1062	970	937	884		517	461
Std. Dev	2.1	4.2	13.4	2.1		0.7	0.7
Δλ	3	6	19	3		1	1

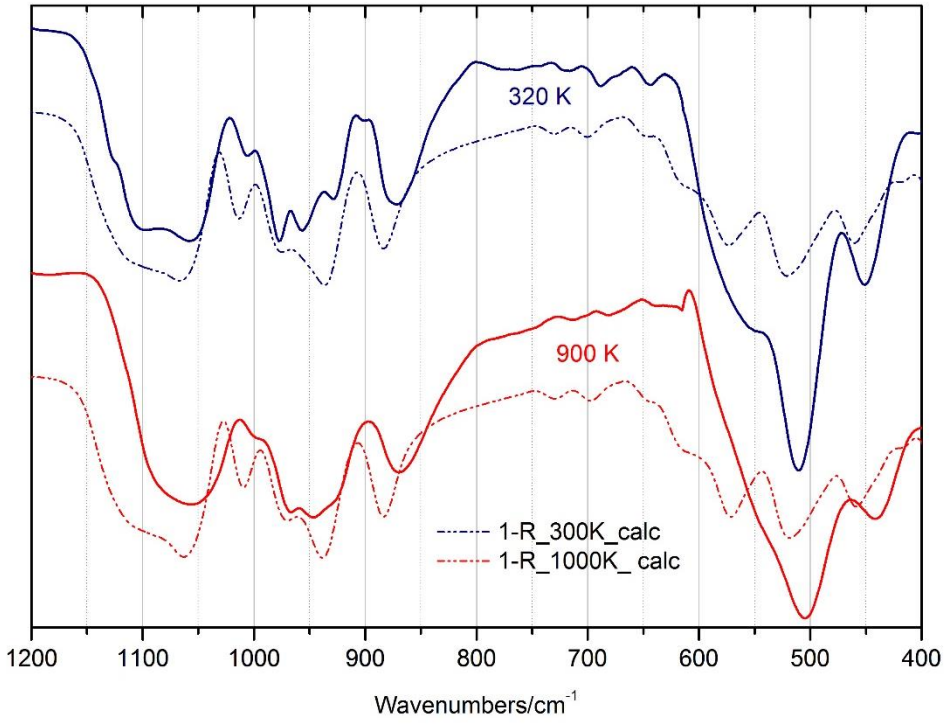

Figure 24: Comparison between calculated 1-R mid IR spectra and experimental emissivity measurements of orthopyroxenes. Solid line: experimental thermal emissivity spectra of Fo89 measured at 320K and 900K (extreme situations). Dotted lines: calculated IR reflectance (inverted) bands of an Mg2Si2O6 endmember. Spectra are in offset for clarity.

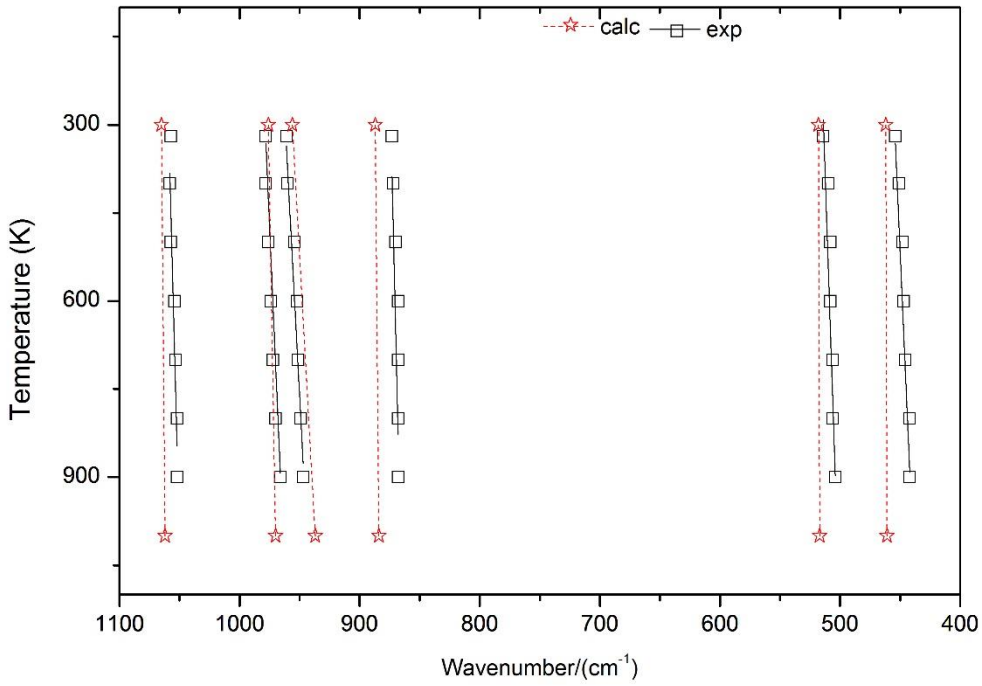

Figure 25: Comparison between calculated and experimental critical absorption. Squares are emissivity bands minima measured at different T steps, lines are linear fits to the measured data. Stars are reflectance band positions calculated at 300K and 1000K, lines are linear fits to the calculated data.

Table 15: The slope and intercept of the bands shift trend calculated from a linear fit of the frequencies vs temperature of the experimental data, and compared with the slope of a line connecting the 300 and 1000 cm^{-1} data.

	Experimental				Calculated	
	intercept		slope		intercept	slope
CA1	1062	(1)	-0.011	(2)	1066	-0.004
CA2	986	(1)	-0.021	(2)	979	-0.009
CA3	968	(2)	-0.024	(3)	964	-0.027
CA4	875	(1)	-0.009	(2)	888	-0.004
CA7	517	(2)	-0.014	(2)	518	-0.001
CA8	459	(1)	-0.020	(2)	462	-0.001
			<-0.017>			<-0.008>

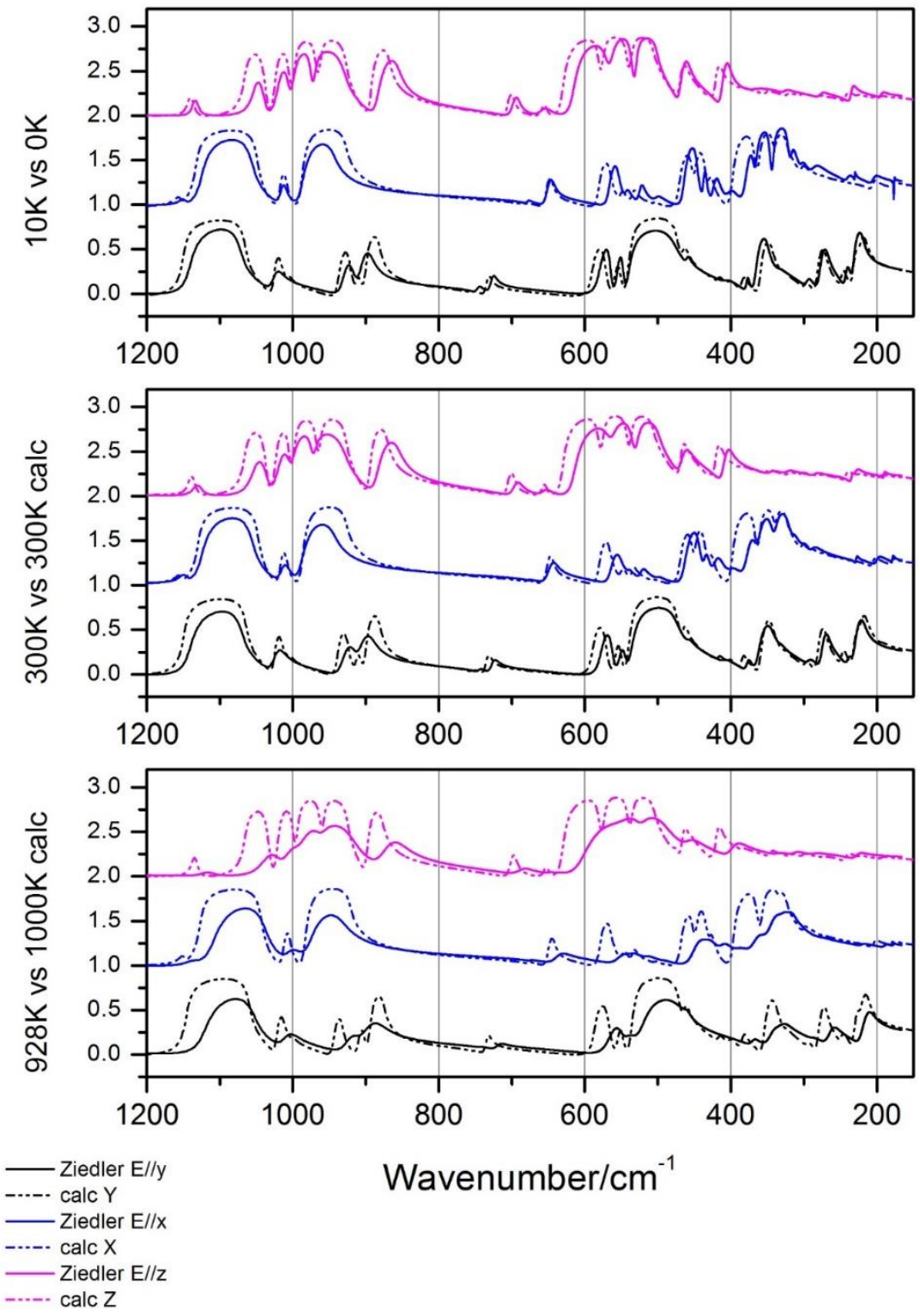

Figure 26: comparisons between the calculated reflective spectra (dotted line) along the three directrions x, y, z and the reflective spectra of a single crystal of synthetic orthoenstatite measured at different steps of temperature (from10 K to 928 K, with steps of 100K for each measurement) (solid line). Experimental measurements are taken from Ziedler et al. (2015).

4.7. Conclusions

The presented calculated data, in comparison with experimental measurements, may be considered as an innovative approach to study and interpret MID-IR spectroscopic data at high temperature. To the author's knowledge no other examples of this kind can be found in literature.

By means of this approach we calculate and foresee with a good level of accuracy band minima shift as a function of temperature and, consequently, it is possible to reliably predict which modes are particularly sensitive to temperature variations.

In both cases, the modelled HT-IR spectra of forsterite and orthoenstatite, show a good agreement with experimental emissivity measurements within the range of investigation of MERTIS (7-14 μm). The agreement with the experiments is found to be good not only from a qualitative point of view, but also at a quantitative level as critical absorptions (CA) and their shifts according to temperature are considered The agreement is of the same order of magnitude of the linear fits of the CAs and their trends of shifts due to temperature is well predicted.

However, some discrepancies between calculated and experimental spectra are evident in both casestudies. Those discrepancies may be due to several reasons that could be associated to the characteristic of the samples measured (compositions, grain sizes, preferential orientations) as well as to computational limitations, or the combinations of the two.

Concerning the latter possibility, one reason may be due to a compositional difference between the end members, which were modelled (forsterite, Mg_2SiO_4 and enstatite $Mg_2Si_2O_6$), and the measured samples ($Mg_{1.76}Fe_{0.22}$ SiO_4, ($Fo_{\#89}$) and ($Ca_{0.01}Mg_{1.73}Fe^{2+}_{0.25}$)$Si_2O_6$. In both cases, the main difference is in the iron content, that is not taken into account in calculations. As we know from literature, Fe^{2+} shifts the band minima to lower wavenumbers (Hamilton 2010, Lane et al. 2011). The same effect was found with the increase of temperature which have the same effects of iron, resulting as a shift of band minima to lower wavenumbers. This effect has been addressed in literature as "chameleon-like effect" (Helbert et al. 2013). In these studies, the two samples have some iron content and have been measured at high temperature; therefore it could be speculated that both effects could lead to additional discrepancies. However, the agreement between experimental and calculated spectrum, which is evident at higher wavenumbers, decreases at lower wavenumbers, both at room and higher temperature. It may be ascribed to the fact that modes at high wavenumbers (1400-600 cm^{-1}) are related to tetrahedral stretching and bending. Tetrahedra are centered in the measured and in calculated samples by Si, and the relevant vibration are less or not affected by non-

tetrahedral cations, like Fe^{2+}. Instead, just for the larger ionic radius of Fe^{2+} than Mg, we can expect that modes involving the M1 and M2 cations, broadly speaking below 600 cm^{-1}, will shift to lower wavenumbers.

To account for the difference between calculated and measured spectra, we must also consider that we did not calculate the phonon contribution outside the Γ point, i.e. the acoustic branch. The calculations of vibrational frequencies for forsterite and orthoenstatite are here calculated at the Γ point of the reciprocal space only.

To extend our calculation to mode having wave vectors off the Γ point , supercell calculations must be done, and the reason why such calculations have not been performed is due to computational cost. The high number of atoms within the unit cell (especially referring to orthoenstatite case, 80 atoms) lead to a high computational cost (which means long time of computations and high performance machines) that couldn't have been afforded during three years of PhD with the available computational sources. Therefore it was not possible to take into account the iron content for both cases or calculate the phonons contributions of the three acoustic branches.

Considering other possible reasons of discrepancies grain sizes and preferential orientations of the samples are issues that may be taken into account, in fact these sample characteristic, to our present knowledge, cannot be simulated with an complete ab initio approach. Emissivity measurements are performed on particulate, therefore, it can be assumed that preferential orientations of the samples can occur, especially within fine grain size ranges. Our simulations, as previously said, discussing experimental methodology, do not take into account any preferential orientations, but are the weighted mean average of three direction in which reflectance is calculated for a virtually infinite perfect single crystal.

As said before, the particulate mineral samples investigated the selected range of particle size and porosity can affect the observed emissivity spectral features, which are the result of both the absorption coefficient and the refractive index. This influence depends on the dominant scattering, which is just due to the dimensional relationship between the grain-size and the incident wave. Thus, coarse particulates are dominated by surface scattering, which leads to enhanced reststrahlen bands in the emissivity spectra. Fine particulate (<65 μm) materials, on the other hand, are dominated by volume scattering (waves are refracted into particle interiors and then scattered or refracted back out), which leads to a reduced contrast in the reststrahlen bands accompanied by the appearance of additional features (Maturilli et al. 2008). In literature is discussed by Emery et

al. (1998) that the size of the fine, loose rocks (regolith) that constitute the surface of Mercury most likely to range between 30 and 100 µm. Therefore, according to the results here presented, it can be assumed that the simulations, with their relative approximations, concerning the grain size issues, are reliable for coarse grain size (250-125 µm).

Moreover according to the range of wavelengths investigated by MERTIS (7-14 µm; 1400-700 cm^{-1}), the concluding remarks concerning the results just discussed show that the TIR modelling presented in this study may be representative for the range and therefore used as a tool to foresee and model the TIR spectra at high temperature within the framework of Mercury remote sensing.

Concluding remarks

In the following concluding remarks the strengths and weaknesses of our investigating approach are summarized as result from the present study. For the conclusions about the Raman and TIR spectroscopic investigations, the reader may have a look at the Conclusion paragraphs at the end of Chapters 3 and 4.

This thesis shows how a combination of *ab initio* methods and experimental measurements may lead to make the most of the accuracy of quantum mechanics, in order to interpret to a more fundamental level the experimental spectroscopic result. This study remarks the reliably of hybrid HF/DFT Hamiltonians to compute vibrational frequencies and shows the potential of CRYSTAL code in order to compare experimental data, accurately simulating a whole vibrational pattern.

We tested our approach to two different minerals, orthopyroxene and forsterite, and two different investigation topics, one focused on simulation and interpretation of Raman spectroscopic data (Chapter 3) and the other one on modelling of the emissivity spectra at high temperature (Chapter 4). If the former presents a rich literature with similar studies of lattice dynamics by means of ab initio studies and spectral modelling (an overview on literature is reported in Chapter 1), the latter represents a completely new approach of modelling with ab initio methods.

In fact, concerning the Raman mode assignment case of study, the simulations provide a theoretical framework in which it has been possible to unravel the observed spectra, especially in complex cases such as orthoenstatite and olivine, where the combinations of modes hinder a proper mode symmetry attribution. It has been shown how a correct mode assignment represents a preliminary step allowing to link the structural changes with pressure, temperature and composition, to the observed spectroscopic feature at the same conditions. These results have been carried out exploiting zero computational cost tools of the code (i.e. isotopic substitution or building units decomposition), permitting to assess the influence of bond distances and cation masses on a given observed mode.

In the second case of study the procedure studied for the modelling of high temperature mid-IR spectra is discussed and the results of compared modelled and measured emissivity spectra are presented. Calculations foresee, with a good level of accuracy, the band minima shift, as a

function of temperature. Therefore a reliable prediction of the spectral features sensitive to temperature variations was achieved. More remarks on results are discussed at the end of Chapter 4.

In our approach we found some discrepancy between calculated and experimental peak positions and intensities, which has to be addressed. These discrepancies are found in both case studies, but more in the modelling of TIR spectra at high temperature. The discrepancies may occur for several reasons that could be associated to the characteristics of the samples measured (compositions, grain sizes, preferential orientations) as well as to computational limitations, or the combinations of the two.

A major computational approximation, which affects the calculated results for some mode, is that we did not calculate the phonon contribution outside the Γ point, i.e. the acoustic branch, as it has been discussed in Chapter 2. The calculations of vibrational frequencies for forsterite and orthoenstatite in this study are calculated at the first Brillouin zone, in both case of studies. To extend our calculation outside the first Brillouin zone, supercell calculations must have been performed; these calculations require high computational efforts. In fact, a high number of atoms within the unit cell has a high computational cost. Referring to orthoenstatite case, for example, which has 80 atoms in the unit cell, 30 independent coordinates, and, according to the factor group analysis, 240 active modes, supercell calculations mean longer computational cost. This could not have been afforded during three years of PhD with the available computational sources.

For the same reason, it was not possible to take into accounts compositional variables besides endmember for both cases.

Nonetheless, a reasonable agreement is shown within the wavelength range of MERTIS (7-14 μm, 1400-700 cm^{-1}), considering not only a qualitative comparison between the calculated and experimental data, but also the linear fits between the experimental and calculated critical absorptions (CA); they are of the same order of magnitude. The above agreement is in part due to compositional details. Reference experimental samples contain a significant amount of Fe for Mg, which has not obviously been included in the quantum mechanical modelling. Instead, from the chemical point of view the tetrahedra of the experimental samples have the same composition ascribed to the modelled structure, i.e. only Si is present in the tetrahedron. As an effect, high wavenumbers (1400-600 cm^{-1}), almost completely related to tetrahedral stretching and bending, are less or not affected by non-tetrahedral cations, like Fe^{2+}, i.e. are less or not affected by the

chemical difference between experiment and modelled phases. Instead, we can expect that modes involving the M1 and M2 cations, below 600 cm^{-1}, are influenced by the larger size of the ionic radius of Fe^{2+}, which shifts the spectral features to lower wavenumbers.

Among other possible reasons of discrepancies, grain sizes and preferential orientations of the samples are topics to take into account. Emissivity measurements are performed on particulate samples and therefore, preferential orientations within the samples can occur, especially for fine grain size. Our simulated spectra, as discussed in Chapter 4, do not take into account any preferential orientations; they are the weighted mean average of three direction in which reflectance is calculated for a virtually infinite perfect single crystal.

As concerns grain size, we have found considerable differences between calculated and experimental spectra for a grain size below 125 μm. On the other side, the results presented in Chapter 4, show that the simulations are reliable for coarser grain size. In fact, according to Maturilli et al., (2008), coarse particulates are dominated by surface scattering, which leads to enhanced Reststrahlen bands in the emissivity spectra. On the other hand, fine particulate (<65 μm) materials, are dominated by volume scattering (waves are refracted into particle interiors and then scattered or refracted back out), which leads to a reduced contrast in the Reststrahlen bands accompanied by the appearance of additional features. This is confirmed by the poor agreement between simulations and the finest grain size (< 25 μm) of the sample measured.

Appendix

Orthoenstatite

Table 16: calculated IR frequencies for orthoenstatite, at static equilibrium, 0 K, 300 K, 1000 K.

static equilibrium		0 K		300 K		1000 K	
cm^{-1}	symmetry	cm^{-1}	symmetry	cm^{-1}	symmetry	cm^{-1}	symmetry
0	B_{1u}	0	B_{1u}	0	B_{1u}	0	B_{1u}
138.18	B_{1u}	136.57	B_{1u}	136.52	B_{1u}	132.96	B_{1u}
141.70	B_{1u}	140.59	B_{1u}	140.16	B_{1u}	138.43	B_{1u}
175.03	B_{1u}	173.40	B_{1u}	172.60	B_{1u}	169.56	B_{1u}
196.17	B_{1u}	195.37	B_{1u}	194.93	B_{1u}	193.13	B_{1u}
228.04	B_{1u}	226.73	B_{1u}	226.28	B_{1u}	222.67	B_{1u}
241.63	B_{1u}	241.12	B_{1u}	241.05	B_{1u}	240.77	B_{1u}
280.69	B_{1u}	278.94	B_{1u}	278.64	B_{1u}	275.33	B_{1u}
293.74	B_{1u}	291.84	B_{1u}	291.17	B_{1u}	287.41	B_{1u}
305.55	B_{1u}	303.98	B_{1u}	303.68	B_{1u}	300.73	B_{1u}
324.06	B_{1u}	321.95	B_{1u}	321.09	B_{1u}	316.71	B_{1u}
349.41	B_{1u}	348.22	B_{1u}	348.00	B_{1u}	344.83	B_{1u}
352.98	B_{1u}	351.73	B_{1u}	351.17	B_{1u}	349.81	B_{1u}
388.78	B_{1u}	387.01	B_{1u}	386.53	B_{1u}	383.49	B_{1u}
414.50	B_{1u}	414.37	B_{1u}	414.73	B_{1u}	414.49	B_{1u}
430.98	B_{1u}	429.91	B_{1u}	429.56	B_{1u}	427.64	B_{1u}
459.67	B_{1u}	458.22	B_{1u}	457.50	B_{1u}	454.53	B_{1u}
462.99	B_{1u}	462.55	B_{1u}	462.37	B_{1u}	461.26	B_{1u}
478.93	B_{1u}	478.53	B_{1u}	478.61	B_{1u}	478.15	B_{1u}
507.57	B_{1u}	506.85	B_{1u}	506.90	B_{1u}	505.55	B_{1u}
542.86	B_{1u}	542.16	B_{1u}	542.02	B_{1u}	540.84	B_{1u}
580.71	B_{1u}	580.04	B_{1u}	580.13	B_{1u}	579.03	B_{1u}
654.35	B_{1u}	653.08	B_{1u}	652.95	B_{1u}	650.23	B_{1u}
699.55	B_{1u}	698.11	B_{1u}	697.77	B_{1u}	694.78	B_{1u}
865.30	B_{1u}	868.01	B_{1u}	870.96	B_{1u}	877.79	B_{1u}
928.90	B_{1u}	927.81	B_{1u}	927.34	B_{1u}	925.35	B_{1u}
969.86	B_{1u}	967.32	B_{1u}	966.90	B_{1u}	961.79	B_{1u}
1006.55	B_{1u}	1003.86	B_{1u}	1003.69	B_{1u}	998.57	B_{1u}
1038.43	B_{1u}	1036.34	B_{1u}	1035.60	B_{1u}	1031.54	B_{1u}
1137.14	B_{1u}	1135.03	B_{1u}	1133.72	B_{1u}	1129.70	B_{1u}
0	B_{2u}	0	B_{2u}	0	B_{2u}	0	B_{2u}
87.48	B_{2u}	86.92	B_{2u}	86.96	B_{2u}	85.81	B_{2u}
150.53	B_{2u}	150.13	B_{2u}	149.94	B_{2u}	148.92	B_{2u}
182.97	B_{2u}	180.44	B_{2u}	179.84	B_{2u}	175.55	B_{2u}
204.95	B_{2u}	204.65	B_{2u}	204.06	B_{2u}	203.26	B_{2u}

233.82	B_{2u}	232.13	B_{2u}	231.53	B_{2u}	228.01	B_{2u}
262.68	B_{2u}	261.29	B_{2u}	260.86	B_{2u}	257.56	B_{2u}
278.85	B_{2u}	276.90	B_{2u}	276.36	B_{2u}	272.88	B_{2u}
293.44	B_{2u}	292.51	B_{2u}	292.11	B_{2u}	290.18	B_{2u}
302.67	B_{2u}	301.67	B_{2u}	301.28	B_{2u}	299.24	B_{2u}
320.63	B_{2u}	319.46	B_{2u}	319.16	B_{2u}	316.62	B_{2u}
324.86	B_{2u}	324.59	B_{2u}	324.41	B_{2u}	324.63	B_{2u}
344.81	B_{2u}	342.02	B_{2u}	341.33	B_{2u}	335.43	B_{2u}
369.10	B_{2u}	367.36	B_{2u}	366.88	B_{2u}	363.60	B_{2u}
407.43	B_{2u}	406.30	B_{2u}	406.14	B_{2u}	403.92	B_{2u}
426.94	B_{2u}	426.27	B_{2u}	426.35	B_{2u}	425.46	B_{2u}
436.98	B_{2u}	435.90	B_{2u}	435.87	B_{2u}	433.96	B_{2u}
453.67	B_{2u}	452.79	B_{2u}	452.86	B_{2u}	451.49	B_{2u}
506.16	B_{2u}	505.37	B_{2u}	505.11	B_{2u}	503.66	B_{2u}
532.84	B_{2u}	532.55	B_{2u}	532.80	B_{2u}	532.26	B_{2u}
549.38	B_{2u}	548.34	B_{2u}	547.84	B_{2u}	546.17	B_{2u}
565.56	B_{2u}	564.91	B_{2u}	565.18	B_{2u}	564.21	B_{2u}
645.60	B_{2u}	644.68	B_{2u}	644.24	B_{2u}	642.31	B_{2u}
681.49	B_{2u}	679.83	B_{2u}	679.53	B_{2u}	675.98	B_{2u}
865.25	B_{2u}	867.96	B_{2u}	870.96	B_{2u}	877.75	B_{2u}
930.89	B_{2u}	928.27	B_{2u}	927.75	B_{2u}	922.78	B_{2u}
934.28	B_{2u}	933.05	B_{2u}	932.60	B_{2u}	930.46	B_{2u}
1011.36	B_{2u}	1008.85	B_{2u}	1008.63	B_{2u}	1003.62	B_{2u}
1050.77	B_{2u}	1048.63	B_{2u}	1047.58	B_{2u}	1043.34	B_{2u}
1156.04	B_{2u}	1153.86	B_{2u}	1153.09	B_{2u}	1148.52	B_{2u}
0	B_{3u}	0	B_{3u}	0	B_{3u}	0	B_{3u}
111.58	B_{3u}	110.38	B_{3u}	109.99	B_{3u}	107.77	B_{3u}
195.57	B_{3u}	193.54	B_{3u}	193.32	B_{3u}	189.22	B_{3u}
216.71	B_{3u}	215.46	B_{3u}	214.34	B_{3u}	211.95	B_{3u}
226.44	B_{3u}	225.93	B_{3u}	225.73	B_{3u}	224.65	B_{3u}
245.59	B_{3u}	245.50	B_{3u}	245.49	B_{3u}	245.92	B_{3u}
272.27	B_{3u}	271.13	B_{3u}	270.59	B_{3u}	268.98	B_{3u}
297.37	B_{3u}	296.75	B_{3u}	296.48	B_{3u}	295.27	B_{3u}
330.55	B_{3u}	328.72	B_{3u}	327.93	B_{3u}	324.23	B_{3u}
344.61	B_{3u}	342.58	B_{3u}	341.77	B_{3u}	336.90	B_{3u}
347.05	B_{3u}	344.53	B_{3u}	343.63	B_{3u}	339.84	B_{3u}
382.88	B_{3u}	382.41	B_{3u}	382.67	B_{3u}	381.82	B_{3u}
402.95	B_{3u}	402.40	B_{3u}	402.29	B_{3u}	401.43	B_{3u}
417.18	B_{3u}	416.91	B_{3u}	416.67	B_{3u}	416.27	B_{3u}
435.92	B_{3u}	434.94	B_{3u}	434.80	B_{3u}	432.74	B_{3u}
463.94	B_{3u}	462.72	B_{3u}	462.53	B_{3u}	460.36	B_{3u}
475.96	B_{3u}	474.75	B_{3u}	474.93	B_{3u}	472.76	B_{3u}
482.80	B_{3u}	482.06	B_{3u}	482.09	B_{3u}	480.59	B_{3u}

492.12	B_{3u}	491.43	B_{3u}	491.55	B_{3u}	490.50	B_{3u}
511.25	B_{3u}	510.38	B_{3u}	510.55	B_{3u}	509.05	B_{3u}
552.03	B_{3u}	550.81	B_{3u}	550.29	B_{3u}	547.96	B_{3u}
572.43	B_{3u}	570.46	B_{3u}	569.80	B_{3u}	565.99	B_{3u}
730.44	B_{3u}	730.47	B_{3u}	731.12	B_{3u}	731.46	B_{3u}
752.58	B_{3u}	752.10	B_{3u}	751.79	B_{3u}	750.99	B_{3u}
884.52	B_{3u}	881.61	B_{3u}	881.20	B_{3u}	875.53	B_{3u}
911.69	B_{3u}	909.06	B_{3u}	908.92	B_{3u}	903.49	B_{3u}
918.66	B_{3u}	921.58	B_{3u}	924.44	B_{3u}	932.10	B_{3u}
1008.76	B_{3u}	1006.45	B_{3u}	1005.56	B_{3u}	1000.87	B_{3u}
1018.50	B_{3u}	1016.90	B_{3u}	1016.05	B_{3u}	1013.06	B_{3u}
1068.17	B_{3u}	1065.94	B_{3u}	1065.17	B_{3u}	1060.50	B_{3u}

Table 17: calculated Raman frequencies for orthoenstatite, at static equilibrium, 0 K, 300 K, 1000 K.

static equilibrium		0 K		300 K		1000 K	
cm^{-1}	symmetry	cm^{-1}	symmetry	cm^{-1}	symmetry	cm^{-1}	symmetry
78.5908	A_g	76.9055	A_g	76.6969	A_g	74.5068	A_g
127.0379	A_g	125.4546	A_g	125.0183	A_g	122.9215	A_g
159.437	A_g	159.163	A_g	159.074	A_g	157.9602	A_g
193.367	A_g	192.1747	A_g	191.5284	A_g	188.4317	A_g
201.3122	A_g	200.7496	A_g	200.2717	A_g	199.0226	A_g
205.9245	A_g	204.6564	A_g	203.8586	A_g	201.4691	A_g
236.3159	A_g	234.4483	A_g	233.7983	A_g	229.5638	A_g
269.7005	A_g	269.0004	A_g	269.0902	A_g	267.2797	A_g
277.3484	A_g	276.2536	A_g	276.0231	A_g	275.1552	A_g
304.7703	A_g	303.6929	A_g	303.5367	A_g	301.353	A_g
325.0564	A_g	322.7527	A_g	321.935	A_g	316.7754	A_g
335.5632	A_g	334.7792	A_g	334.4557	A_g	333.5264	A_g
343.3557	A_g	341.2855	A_g	340.4876	A_g	336.9386	A_g
387.061	A_g	385.6432	A_g	385.1839	A_g	382.2411	A_g
406.3254	A_g	404.8956	A_g	404.6772	A_g	402.1669	A_g
425.6442	A_g	424.247	A_g	423.7386	A_g	421.2049	A_g
451.3577	A_g	450.7421	A_g	450.4757	A_g	448.4574	A_g
458.4233	A_g	456.9685	A_g	456.3985	A_g	453.8723	A_g
481.2028	A_g	481.1615	A_g	481.6103	A_g	481.7433	A_g
535.5918	A_g	535.1494	A_g	534.9486	A_g	534.4005	A_g
551.9881	A_g	551.4922	A_g	551.6265	A_g	551.0541	A_g
561.4939	A_g	560.6668	A_g	560.552	A_g	559.2689	A_g
668.4115	A_g	667.476	A_g	667.3616	A_g	665.535	A_g
692.7886	A_g	691.3214	A_g	690.8348	A_g	687.8577	A_g

865.7518	A_g	868.4282	A_g	871.4367	A_g	878.1395	A_g
924.4853	A_g	922.5896	A_g	922.1417	A_g	918.4682	A_g
933.3501	A_g	931.6135	A_g	931.1353	A_g	928.1324	A_g
1011.591	A_g	1008.596	A_g	1008.337	A_g	1002.303	A_g
1026.741	A_g	1024.36	A_g	1023.423	A_g	1018.383	A_g
1039.37	A_g	1037.291	A_g	1036.493	A_g	1032.485	A_g
152.7809	B_{1g}	152.2709	B_{1g}	151.8701	B_{1g}	150.6525	B_{1g}
160.6904	B_{1g}	160.1357	B_{1g}	159.5582	B_{1g}	158.0604	B_{1g}
184.2973	B_{1g}	183.5625	B_{1g}	183.3934	B_{1g}	183.4756	B_{1g}
194.9237	B_{1g}	193.8136	B_{1g}	193.0695	B_{1g}	191.2319	B_{1g}
224.0843	B_{1g}	222.2321	B_{1g}	221.1956	B_{1g}	217.4576	B_{1g}
245.219	B_{1g}	244.3663	B_{1g}	243.9622	B_{1g}	242.4687	B_{1g}
282.9322	B_{1g}	281.595	B_{1g}	281.2245	B_{1g}	278.5236	B_{1g}
299.0692	B_{1g}	298.1747	B_{1g}	297.4895	B_{1g}	295.3031	B_{1g}
310.677	B_{1g}	309.2775	B_{1g}	308.7086	B_{1g}	305.8259	B_{1g}
340.9021	B_{1g}	339.2388	B_{1g}	338.7767	B_{1g}	335.8307	B_{1g}
347.7378	B_{1g}	344.9072	B_{1g}	344.1022	B_{1g}	338.8319	B_{1g}
379.0255	B_{1g}	378.8468	B_{1g}	378.8217	B_{1g}	378.4795	B_{1g}
394.5259	B_{1g}	394.0165	B_{1g}	394.0224	B_{1g}	393.3109	B_{1g}
406.4226	B_{1g}	404.8225	B_{1g}	404.343	B_{1g}	401.1512	B_{1g}
422.2013	B_{1g}	421.3022	B_{1g}	421.3141	B_{1g}	419.7026	B_{1g}
457.5383	B_{1g}	457.2355	B_{1g}	457.382	B_{1g}	456.6745	B_{1g}
467.9948	B_{1g}	467.6527	B_{1g}	468.23	B_{1g}	467.9813	B_{1g}
488.6367	B_{1g}	487.4596	B_{1g}	487.2732	B_{1g}	484.9317	B_{1g}
522.2612	B_{1g}	520.7509	B_{1g}	520.6486	B_{1g}	517.8987	B_{1g}
531.3133	B_{1g}	529.8594	B_{1g}	529.4628	B_{1g}	526.8889	B_{1g}
593.9672	B_{1g}	593.4108	B_{1g}	593.2268	B_{1g}	592.1481	B_{1g}
610.1687	B_{1g}	608.9003	B_{1g}	608.4069	B_{1g}	606.4759	B_{1g}
735.2504	B_{1g}	735.0407	B_{1g}	734.8728	B_{1g}	734.5434	B_{1g}
758.7428	B_{1g}	758.4638	B_{1g}	758.5559	B_{1g}	758.756	B_{1g}
885.9462	B_{1g}	883.0239	B_{1g}	882.5948	B_{1g}	876.9759	B_{1g}
918.7414	B_{1g}	916.3457	B_{1g}	916.2971	B_{1g}	911.1676	B_{1g}
944.9521	B_{1g}	947.2128	B_{1g}	949.3944	B_{1g}	955.5179	B_{1g}
1023.292	B_{1g}	1021.403	B_{1g}	1020.353	B_{1g}	1016.615	B_{1g}
1043.414	B_{1g}	1041.054	B_{1g}	1040.25	B_{1g}	1035.329	B_{1g}
1066.609	B_{1g}	1064.581	B_{1g}	1064.16	B_{1g}	1060.587	B_{1g}
81.2055	B_{2g}	80.5832	B_{2g}	80.2942	B_{2g}	79.2929	B_{2g}
159.9586	B_{2g}	159.0145	B_{2g}	158.2295	B_{2g}	156.1551	B_{2g}
163.8794	B_{2g}	163.0255	B_{2g}	162.6365	B_{2g}	160.9058	B_{2g}
212.0096	B_{2g}	210.4215	B_{2g}	210.0646	B_{2g}	207.8464	B_{2g}
237.5043	B_{2g}	236.3339	B_{2g}	235.7067	B_{2g}	233.1079	B_{2g}
248.1932	B_{2g}	247.1891	B_{2g}	246.6668	B_{2g}	245.1644	B_{2g}
285.0361	B_{2g}	283.3893	B_{2g}	282.8628	B_{2g}	279.717	B_{2g}

303.5344	B_{2g}	302.7512	B_{2g}	302.2454	B_{2g}	300.2796	B_{2g}
311.232	B_{2g}	309.9047	B_{2g}	309.3412	B_{2g}	306.9405	B_{2g}
340.8161	B_{2g}	338.8698	B_{2g}	338.3251	B_{2g}	334.8924	B_{2g}
358.9512	B_{2g}	357.2732	B_{2g}	356.5018	B_{2g}	353.255	B_{2g}
388.6013	B_{2g}	388.1086	B_{2g}	388.0329	B_{2g}	387.1882	B_{2g}
401.0826	B_{2g}	400.0607	B_{2g}	399.833	B_{2g}	397.8501	B_{2g}
414.691	B_{2g}	413.6237	B_{2g}	413.4972	B_{2g}	411.5038	B_{2g}
426.4928	B_{2g}	426.3323	B_{2g}	426.5057	B_{2g}	426.0937	B_{2g}
448.8069	B_{2g}	447.8045	B_{2g}	447.7676	B_{2g}	446.204	B_{2g}
473.8679	B_{2g}	472.8843	B_{2g}	472.8461	B_{2g}	470.9414	B_{2g}
477.4242	B_{2g}	476.5406	B_{2g}	476.7734	B_{2g}	475.1879	B_{2g}
498.4	B_{2g}	497.5383	B_{2g}	497.641	B_{2g}	496.1204	B_{2g}
527.2213	B_{2g}	526.0244	B_{2g}	526.1915	B_{2g}	524.0686	B_{2g}
553.2052	B_{2g}	551.9016	B_{2g}	551.3921	B_{2g}	548.92	B_{2g}
609.8186	B_{2g}	608.5504	B_{2g}	608.0592	B_{2g}	606.1027	B_{2g}
748.7977	B_{2g}	748.9576	B_{2g}	748.9344	B_{2g}	749.3788	B_{2g}
759.9625	B_{2g}	759.415	B_{2g}	759.3336	B_{2g}	758.9228	B_{2g}
893.9311	B_{2g}	890.8987	B_{2g}	890.4142	B_{2g}	884.6617	B_{2g}
906.1208	B_{2g}	903.4506	B_{2g}	903.244	B_{2g}	897.7932	B_{2g}
942.8293	B_{2g}	945.3811	B_{2g}	947.7338	B_{2g}	954.2348	B_{2g}
1016.749	B_{2g}	1015.301	B_{2g}	1014.616	B_{2g}	1011.976	B_{2g}
1025.117	B_{2g}	1022.632	B_{2g}	1021.601	B_{2g}	1016.611	B_{2g}
1062.614	B_{2g}	1060.591	B_{2g}	1059.967	B_{2g}	1055.691	B_{2g}
107.6763	B_{3g}	105.195	B_{3g}	104.7205	B_{3g}	101.338	B_{3g}
145.0848	B_{3g}	144.3133	B_{3g}	144.083	B_{3g}	142.2852	B_{3g}
158.0604	B_{3g}	157.303	B_{3g}	157.0516	B_{3g}	154.9464	B_{3g}
166.0586	B_{3g}	165.2787	B_{3g}	165.1263	B_{3g}	163.3333	B_{3g}
195.5745	B_{3g}	194.6434	B_{3g}	193.8969	B_{3g}	192.287	B_{3g}
224.7435	B_{3g}	223.8006	B_{3g}	223.5475	B_{3g}	221.5276	B_{3g}
233.3558	B_{3g}	232.2862	B_{3g}	231.699	B_{3g}	229.3739	B_{3g}
262.9816	B_{3g}	262.5535	B_{3g}	262.1782	B_{3g}	261.5111	B_{3g}
296.163	B_{3g}	295.5978	B_{3g}	295.2283	B_{3g}	292.5408	B_{3g}
298.7543	B_{3g}	296.8556	B_{3g}	296.4797	B_{3g}	294.1458	B_{3g}
318.2518	B_{3g}	316.294	B_{3g}	315.6854	B_{3g}	311.3205	B_{3g}
326.6478	B_{3g}	324.2387	B_{3g}	323.7573	B_{3g}	320.0672	B_{3g}
364.0179	B_{3g}	363.0175	B_{3g}	362.9484	B_{3g}	360.9626	B_{3g}
386.3968	B_{3g}	385.5866	B_{3g}	385.3221	B_{3g}	383.7943	B_{3g}
412.1386	B_{3g}	411.2563	B_{3g}	411.2835	B_{3g}	409.5608	B_{3g}
421.7272	B_{3g}	419.4701	B_{3g}	418.8482	B_{3g}	414.3388	B_{3g}
450.2447	B_{3g}	449.1548	B_{3g}	449.2214	B_{3g}	447.5146	B_{3g}
469.5874	B_{3g}	468.5426	B_{3g}	468.1921	B_{3g}	465.5322	B_{3g}
523.4262	B_{3g}	523.2108	B_{3g}	523.5553	B_{3g}	523.0712	B_{3g}
541.7032	B_{3g}	541.2761	B_{3g}	541.0605	B_{3g}	540.4982	B_{3g}

549.6704	B_{3g}	548.8623	B_{3g}	548.575	B_{3g}	547.1249	B_{3g}
566.3458	B_{3g}	565.7055	B_{3g}	565.744	B_{3g}	564.6044	B_{3g}
658.8216	B_{3g}	657.6316	B_{3g}	657.39	B_{3g}	655.1203	B_{3g}
687.9965	B_{3g}	686.6088	B_{3g}	686.5309	B_{3g}	683.6904	B_{3g}
865.7409	B_{3g}	868.4115	B_{3g}	871.3691	B_{3g}	878.1265	B_{3g}
931.7446	B_{3g}	930.414	B_{3g}	929.9202	B_{3g}	927.4222	B_{3g}
957.1966	B_{3g}	954.5791	B_{3g}	954.0061	B_{3g}	949.493	B_{3g}
1023.845	B_{3g}	1021.483	B_{3g}	1021.286	B_{3g}	1016.381	B_{3g}
1026.391	B_{3g}	1023.921	B_{3g}	1022.846	B_{3g}	1017.608	B_{3g}
1152.516	B_{3g}	1150.394	B_{3g}	1149.924	B_{3g}	1145.022	B_{3g}

Forsterite

Table 18: calculated IR frequencies for forsterite, at static equilibrium, 0 K, 300 K, 1000 K.

static equilibrium		0 K		300 K		1000 K	
cm^{-1}	symmetry	cm^{-1}	symmetry	cm^{-1}	symmetry	cm^{-1}	symmetry
0	B_{1u}	0	B_{1u}	0	B_{1u}	0	B_{1u}
205.41	B_{1u}	205.44	B_{1u}	204.89	B_{1u}	203.68	B_{1u}
282.83	B_{1u}	282.80	B_{1u}	277.15	B_{1u}	265.14	B_{1u}
297.67	B_{1u}	297.66	B_{1u}	290.73	B_{1u}	277.02	B_{1u}
320.26	B_{1u}	320.31	B_{1u}	311.41	B_{1u}	297.86	B_{1u}
427.06	B_{1u}	426.76	B_{1u}	417.37	B_{1u}	401.92	B_{1u}
434.60	B_{1u}	434.43	B_{1u}	426.40	B_{1u}	412.72	B_{1u}
489.66	B_{1u}	489.61	B_{1u}	485.21	B_{1u}	476.96	B_{1u}
513.62	B_{1u}	513.59	B_{1u}	508.53	B_{1u}	501.48	B_{1u}
876.75	B_{1u}	877.06	B_{1u}	870.74	B_{1u}	859.95	B_{1u}
0	B_{2u}	0	B_{2u}	0	B_{2u}	0	B_{2u}
208.82	B_{2u}	208.81	B_{2u}	203.56	B_{2u}	194.90	B_{2u}
280.00	B_{2u}	279.85	B_{2u}	275.23	B_{2u}	265.90	B_{2u}
299.28	B_{2u}	299.07	B_{2u}	293.21	B_{2u}	280.72	B_{2u}
324.43	B_{2u}	324.07	B_{2u}	320.19	B_{2u}	314.17	B_{2u}
397.79	B_{2u}	397.68	B_{2u}	387.32	B_{2u}	370.34	B_{2u}
415.88	B_{2u}	415.90	B_{2u}	409.21	B_{2u}	398.40	B_{2u}
481.78	B_{2u}	481.85	B_{2u}	473.62	B_{2u}	460.05	B_{2u}
515.97	B_{2u}	515.91	B_{2u}	509.16	B_{2u}	497.35	B_{2u}
541.85	B_{2u}	541.79	B_{2u}	535.14	B_{2u}	525.12	B_{2u}
611.98	B_{2u}	611.83	B_{2u}	607.61	B_{2u}	600.87	B_{2u}
838.38	B_{2u}	838.35	B_{2u}	831.89	B_{2u}	821.10	B_{2u}

963.73	B_{2u}	963.58	B_{2u}	956.05	B_{2u}	943.11	B_{2u}
986.31	B_{2u}	986.23	B_{2u}	977.96	B_{2u}	964.27	B_{2u}
0	B_{3u}	0	B_{3u}	0	B_{3u}	0	B_{3u}
146.07	B_{3u}	145.99	B_{3u}	142.71	B_{3u}	136.58	B_{3u}
282.90	B_{3u}	282.74	B_{3u}	276.90	B_{3u}	265.93	B_{3u}
297.22	B_{3u}	297.11	B_{3u}	290.83	B_{3u}	280.43	B_{3u}
359.43	B_{3u}	359.32	B_{3u}	349.61	B_{3u}	333.33	B_{3u}
407.54	B_{3u}	407.43	B_{3u}	401.34	B_{3u}	390.44	B_{3u}
437.22	B_{3u}	437.08	B_{3u}	429.33	B_{3u}	416.94	B_{3u}
469.95	B_{3u}	469.87	B_{3u}	461.96	B_{3u}	449.11	B_{3u}
517.41	B_{3u}	517.39	B_{3u}	512.38	B_{3u}	501.67	B_{3u}
537.18	B_{3u}	536.98	B_{3u}	530.51	B_{3u}	521.80	B_{3u}
637.33	B_{3u}	637.03	B_{3u}	631.76	B_{3u}	622.95	B_{3u}
834.74	B_{3u}	834.79	B_{3u}	828.13	B_{3u}	817.00	B_{3u}
871.04	B_{3u}	871.10	B_{3u}	864.90	B_{3u}	854.08	B_{3u}
995.00	B_{3u}	994.51	B_{3u}	985.51	B_{3u}	970.45	B_{3u}

Table 19: calculated Raman frequencies for forsterite, at static equilibrium, 0 K, 300 K, 1000 K.

static equilibrium		0 K		300 K		1000 K	
cm^{-1}	symmetry	cm^{-1}	symmetry	cm^{-1}	symmetry	cm^{-1}	symmetry
191.02	A_g	190.76	A_g	187.50	A_g	181.12	A_g
234.19	A_g	234.22	A_g	232.32	A_g	228.62	A_g
314.92	A_g	314.76	A_g	306.73	A_g	292.32	A_g
335.51	A_g	335.45	A_g	328.12	A_g	313.23	A_g
351.46	A_g	351.24	A_g	343.87	A_g	333.28	A_g
432.27	A_g	432.19	A_g	423.19	A_g	408.71	A_g
556.12	A_g	556.02	A_g	552.89	A_g	547.57	A_g
616.45	A_g	616.39	A_g	611.18	A_g	602.55	A_g
818.83	A_g	819.03	A_g	812.11	A_g	800.57	A_g
857.10	A_g	857.30	A_g	851.21	A_g	840.92	A_g
973.95	A_g	973.60	A_g	964.40	A_g	949.14	A_g
228.05	B_{1g}	227.94	B_{1g}	224.24	B_{1g}	217.32	B_{1g}
263.25	B_{1g}	262.79	B_{1g}	258.60	B_{1g}	249.99	B_{1g}
323.69	B_{1g}	323.34	B_{1g}	315.86	B_{1g}	303.12	B_{1g}
371.93	B_{1g}	371.85	B_{1g}	365.10	B_{1g}	353.75	B_{1g}
392.44	B_{1g}	392.54	B_{1g}	389.17	B_{1g}	383.24	B_{1g}
447.57	B_{1g}	447.32	B_{1g}	439.85	B_{1g}	427.24	B_{1g}
593.74	B_{1g}	593.37	B_{1g}	588.47	B_{1g}	579.85	B_{1g}
644.12	B_{1g}	643.75	B_{1g}	637.87	B_{1g}	628.10	B_{1g}

834.34	B_{1g}	834.41	B_{1g}	827.47	B_{1g}	815.76	B_{1g}
866.69	B_{1g}	866.81	B_{1g}	860.59	B_{1g}	849.77	B_{1g}
985.81	B_{1g}	985.30	B_{1g}	976.30	B_{1g}	961.23	B_{1g}
194.49	B_{2g}	194.85	B_{2g}	189.11	B_{2g}	179.32	B_{2g}
303.54	B_{2g}	303.62	B_{2g}	300.73	B_{2g}	296.05	B_{2g}
326.64	B_{2g}	326.55	B_{2g}	320.11	B_{2g}	308.41	B_{2g}
388.40	B_{2g}	388.30	B_{2g}	380.28	B_{2g}	365.37	B_{2g}
423.78	B_{2g}	423.53	B_{2g}	417.32	B_{2g}	408.08	B_{2g}
604.94	B_{2g}	604.83	B_{2g}	600.83	B_{2g}	593.85	B_{2g}
928.85	B_{2g}	929.25	B_{2g}	923.29	B_{2g}	913.28	B_{2g}
182.39	B_{3g}	182.56	B_{3g}	180.86	B_{3g}	177.70	B_{3g}
256.59	B_{3g}	256.65	B_{3g}	251.11	B_{3g}	241.52	B_{3g}
331.06	B_{3g}	331.05	B_{3g}	322.93	B_{3g}	307.72	B_{3g}
377.85	B_{3g}	377.84	B_{3g}	372.91	B_{3g}	363.61	B_{3g}
455.47	B_{3g}	454.98	B_{3g}	446.55	B_{3g}	434.01	B_{3g}
602.90	B_{3g}	602.80	B_{3g}	599.43	B_{3g}	593.44	B_{3g}
886.04	B_{3g}	886.34	B_{3g}	880.07	B_{3g}	869.46	B_{3g}

Table 20 experimental bond distances in orthoenstatite and orthoferrosilite from literature

	(Yang & Ghose) $Mg_2Si_2O_6$ (Å)	(Sasaki et al. 1992) $Fe_2Si_2O_6$ (Å)
M1-O1A	2.025	2.086
-O1A	2.153	2.193
-O2A	2.005	2.128
-O1B	2.065	2.195
-O1B	2.172	2.085
-O2B	2.042	2.122
mean	2.077	2.135
M2-O1A	2.09	2.09
-O2A	2.037	2.037
-O3A	2.287	2.287
-O1B	2.056	2.056
-O2B	1.994	1.994
-O3B	2.448	2.448
mean	2.152	2.152
SiA-O1A	1.614	1.612
-O2A	1.59	1.604
-O3A	1.646	1.636
-O3A	1.667	1.652

mean	1.629	1.626
SiB-O1B	1.623	1.619
-O2B	1.589	1.603
-O3B	1.674	1.663
-O3B	1.679	1.667
mean	1.641	1.638

			Reyand (1991)				Hofmeister (1987)				Iishi (1978)				Servion and Piriou (1973)			
	TO	LO	TO		LO		TO		LO		TO		LO		TO		LO	
symmetry	cm^{-1}	cm^{-1}	ν cm^{-1}	Δν	ν cm^{-1}	Δν	ν cm^{-1}	Δν	ν cm^{-1}	Δν	ν cm^{-1}	Δν	ν cm^{-1}	Δν	ν cm^{-1}	Δν	ν cm^{-1}	Δν
B_{1u}	205	205	–	-	–	-	–	-	–	-	–	-	–	-	–	-	–	-
B_{1u}	283	284	274	9	277	7	276	7	276	8	274	9	278	6	274	9	276	8
B_{1u}	298	325	282	16	307	18	293	5	299	26	296	2	318	7	289	9	316	9
B_{1u}	320	318	–	–	–	-	309	11	313	5	–	-	–	-	–	-	–	-
B_{1u}	–	–	370	–	380	-	365	-	371	-	365	-	371	-	–	-	–	-
B_{1u}	427	462	403	24	410	52	–	-	–	-	–	-	–	-	–	-	–	-
B_{1u}	434	433	411	23	451	-18	412	22	450	-17	423	11	459	-26	415	19	454	-21
B_{1u}	490	501	472	18	482	19	463	27	482	19	483	7	489	12	474	16	483	18
B_{1u}	514	593	501	13	580	13	502	12	573	20	502	12	585	8	501	13	574	19
B_{1u}	–	–	–	-	–	-	543	-	538	-	–	-	–	-	531	-	528	-
B_{1u}	877	1006	869	8	1008	-2	865	12	-957	-	885	-8	994	12	871	6	-960	-
B_{2u}	146	147	140	6	143	4	142	4	144	3	–	-	–	-	–	-	–	-
B_{2u}	283	283	275	8	278	5	268	15	276	7	280	3	283	0	276	7	277	6
B_{2u}	297	315	283	14	305	10	290	7	308	7	294	3	313	2	290	7	310	5
B_{2u}	–	–	–	-	–	-	300	-	298	-	–	-	–	-	–	-	–	-
B_{2u}	359	388	341	18	371	17	345	14	375	13	352	7	376	12	350	9	375	13
B_{2u}	407	425	390	17	406	19	398	9	408	17	400	7	412	13	394	13	408	17
B_{2u}	437	456	415	22	439	17	418	19	438	18	421	16	446	10	416	21	442	14
B_{2u}	470	498	456	14	484	14	452	18	488	10	465	5	493	5	456	14	488	10
B_{2u}	517	525	503	14	511	14	504	13	511	14	510	7	516	9	506	11	514	11
B_{2u}	537	588	526	11	572	16	520	17	572	16	537	0	597	-9	527	10	573	15
B_{2u}	637	637	–	-	–	-	–	-	–	-	–	-	–	-	–	-	–	-
B_{2u}	835	843	830	5	841	2	828	7	844	-1	838	-3	843	0	838	-3	845	-2

B_{2u}	871	968	867	4	970	-2	865	6	961	7	882	-11	979	-11	875	-4	962	6
B_{2u}	995	1003	987	8	1001	2	983	12	996	7	987	8	993	10	983	12	992	11
B_{3u}	209	209	199	10	201	8	201	8	201	8	–	-	–	-	–	-	–	-
B_{3u}	280	280	274	6	276	4	275	5	276	4	274	6	276	4	274	6	276	4
B_{3u}	299	304	–	-	–	-	293	6	298	6	293	6	298	6	–	-	–	-
B_{3u}	–	–	–	-	–	-	309	-	313	-	–	-	–	-	–	-	–	-
B_{3u}	324	326	316	8	320	6	319	5	321	5	320	4	323	3	318	6	321	5
B_{3u}	398	404	374	24	384	20	377	21	388	16	378	20	386	18	378	20	–	-
B_{3u}	416	485	397	19	463	22	405	11	463	22	403	13	469	16	404	12	469	16
B_{3u}	–	–	420	-	420	-	434	-	430	-	–	-	–	-	438	-	438	-
B_{3u}	482	480	–	-	–	-	–	-	–	-	–	-	–	-	–	-	–	-
B_{3u}	516	569	498	18	544	25	505	11	511	58	498	18	544	25	498	18	548	21
B_{3u}	542	540	–	-	–	-	–	-	–	-	–	-	–	-	–	-	–	-
B_{3u}	612	649	601	11	650	-1	601	11	644	5	601	11	645	4	601	11	645	4
B_{3u}	838	839	833	5	839	0	841	-3	842	-3	838	0	845	-6	838	0	840	-1
B_{3u}	964	970	952	12	961	9	950	14	961	9	957	7	963	7	957	7	964	6
B_{3u}	986	1068	971	15	1089	-21	988	-2	-991	-	980	6	1086	-18	978	8	1081	-13
			N	29	N	29	N	30	N	28	N	27	N	27	N	26	N	24
			<Δν>	13	<Δν>	10	<Δν>	11	<Δν>	11	<Δν>	6	<Δν>	4	<Δν>	10	<Δν>	8
			<|Δν|>	13	<|Δν|>	13	<|Δν|>	11	<|Δν|>	13	<|Δν|>	8	<|Δν|>	10	<|Δν|>	10	<|Δν|>	11
			|Δν|max	24	|Δν|max	52	|Δν|max	27	|Δν|max	58	|Δν|max	20	|Δν|max	26	|Δν|max	21	|Δν|max	21

Bibliography

Angel, R.J., chopelas, Ross, N.L., 1992. stability of high density clinoenstatite at upper mantle pressures. *Nature* 358, 322.

Angel, R.J., Jackson, J.M., 2002. Elasticity and equation of state of orthoenstatite, $MgSiO_3$. *American Mineralogist* 87, 558–561. doi:10.2138/am-2002-0419

Belmonte, D., Ottonello, G., Zuccolini, M. V., 2014. Ab initio thermodynamic and thermophysical properties of sapphirine end-members in the join Mg4Al8Si2O20-Mg3Al10SiO20. *American Mineralogist* 99, 1449–1461. doi:10.2138/am.2014.4833

Bouhifd, M. a, Andrault, D., Fiquet, G., Richet, P., 1996. Thermal expansion of forsterite up to the melting point . *Geophysical Research Letters* 23, 1143–1146. doi:10.1029/96GL01118

Bowey, J.E., Lee, C., Tucker, C., Hofmeister, A.M., Ade, P.A.R., Barlow, M.J., 2001. Temperature effects on the 15 85 mm spectra of olivines and pyroxenes. *Monthly Notices of the Royal Astronomical Society* 325, 886–896.

Braithwaite, J.S., Wright, K., Catlow, C.R.A., 2003. A theoretical study of the energetics and IR frequencies of hydroxyl defects in forsterite. *Journal of Geophysical Research: Solid Earth* 108. doi:10.1029/2002JB002126

Brown, S., Elkins-Tanton, L., 2009. Compositions of Mercury's earliest crust from magma ocean models. *Earth and Planetary Science Letters*.

Cameron, M., Sueno, S., Prewitt, C.T., Papike, J.J., 1973. High-Temperature crystal chemistry of acmite, diopside, hedenbergite, jadeite, spodumene, and Ureyite. *American Mineralogist* 58, 594–618.

Caracas, R., Bobocioiu, E., 2011. The WURM project--a freely available web-based repository of computed physical data for minerals. *American Mineralogist* 96, 437–443. doi:10.2138/am.2011.3532

Causa, M., Dovesi, R., Orlando, R., Pisani, C., Saunders, V.R., 1988. Treatment of the exchange interactions in Hartree-Fock LCAO calculations of periodic systems. *The Journal of Physical Chemistry* 92, 909–913. doi:10.1021/j100315a010

Chopelas, A., 1990. Thermal properties of forsterite at mantle pressures derived from vibrational spectroscopy. *Physics and Chemistry of Minerals* 17, 149–156. doi:10.1007/BF00199666

Chopelas, A., 1991. Single crystal Raman spectra of forsterite, fayalite, and monticellite. *American Mineralogist* 76, 1101–1109.

Chopelas, A., 1999. Estimates of mantle relevant Clapeyron slopes in the $MgSiO_3$ system from high-pressure spectroscopic data. *American Mineralogist* 84, 233–244. doi:10.2138/am-1999-0304

Choudhury, N., Ghose, S., Chowdhury, C.P., Loong, C.K., Chaplot, S.L., 1998. Lattice dynamics, Raman spectroscopy, and inelastic neutron scattering of orthoenstatite Mg2 Si2O6. *Physical Review B* 58, 756–765. doi:10.1103/PhysRevB.58.756

Christensen, P.R., Bandfield, J.L., Hamilton, V.E., Howard, D.A., Lane, M.D., Piatek, J.L., Ruff, S.W., Stefanov, W.L., 2000. A thermal emission spectral library of rock-forming minerals. *Journal of Geophysical Research: Planets* 105, 9735–9739. doi:10.1029/1998JE000624

Civalleri, B., D'Arco, P., Orlando, R., Saunders, V.R., Dovesi, R., 2001. Hartree–Fock geometry optimisation of periodic systems with the Crystal code, Chemical Physics Letters. doi:10.1016/S0009-2614(01)01081-8

Cooper, B., Potter, A., Killen, R., 2001. Midinfrared spectra of Mercury. *Journal of Geophysical*.

Daniel, I., Guyot, F., Gillet, P., 1997. Anharmonic properties of Mg2SiO4-forsterite measured from the volume dependence of the Raman spectrum. *European Journal Of Mineralogy* 9, 255–262.

Demichelis, R., Suto, H., Noël, Y., Sogawa, H., Naoi, T., Koike, C., Chihara, H., Shimobayashi, N., Ferrabone, M., Dovesi, R., 2012. The infrared spectrum of ortho-enstatite from reflectance experiments and first-principle simulations. *Monthly Notices of the Royal Astronomical Society* 420, 147–154. doi:10.1111/j.1365-2966.2011.20018.x

Doll, K., Saunders, V.R., Harrison, N.M., 2001. Analytical Hartree-Fock gradients for periodic systems. *International Journal of Quantum Chemistry* 82, 1–31.

Domeneghetti, M.C., Molin, G.M., Stimpfl, M., Tribaudino, M., 1995. Orthopyroxene from the Serra de Mage Meteorite; structure refinement and estimation of C2/c pyroxene contributions to apparent Pbca diffraction violations. *American Mineralogist* 80, 923–929. doi:10.2138/am-1995-9-1007

Domeneghetti, M.C., Molin, G.M., Tazzoli, V., 1985. Crystal-chemical implications of the Mg (super 2+) -Fe (super 2+) distribution in orthopyroxenes. *American Mineralogist* 70.

Dove, M.T., 2011. Introduction to the theory of lattice dynamics. *Collection SFN* 12, 123–159. doi:10.1051/sfn/201112007

Dovesi, R., Pisani, C., Roetti, C., Saunders, V.R., 1983. Treatment of Coulomb interactions in Hartree-Fock calculations of periodic systems. *Physical Review B* 28, 5781–5792. doi:10.1103/PhysRevB.28.5781

Dovesi, R., Saunders, V.R., Roetti, C., Orlando, R., Zicovich-Wilson, C.M., Pascale, F., Civalleri, B., Doll, K., Harrison, N.M., Bush, I.J., D'Arco, P., Llunell, M., Causa, M., Noël, Y., 2013. Crystal14.

Emery, J., Sprague, A., Witteborn, F., Colwell, J., 1998. Mercury: Thermal modeling and mid-infrared (5–12 μm) observations. *Icarus*.

Ferrari, S., Nestola, F., Massironi, M., Maturilli, A., Helbert, J., Alvaro, M., Domeneghetti, M.C., Zorzi, F., 2014. In-situ high-temperature emissivity spectra and thermal expansion of C2/c pyroxenes: Implications for the surface of Mercury. *American Mineralogist* 99, 786–792. doi:10.2138/am.2014.4698

Ferrero, M., Rérat, M., Orlando, R., Dovesi, R., Bush, I.J., 2008. Coupled perturbed Kohn-Sham calculation of static polarizabilities of periodic compounds. Journal of Physics: Conference Series 117, 12016. doi:10.1088/1742-6596/117/1/012016

Finkelstein, G.J., Dera, P.K., Jahn, S., Oganov, A.R., Holl, C.M., Meng, Y., Duffy, T.S., 2014. Phase transitions and equation of state of forsterite to 90 GPa from single-crystal X-ray diffraction and molecular modeling. *American Mineralogist* 99, 35–43. doi:10.2138/am.2014.4526

Ghose, S., Hastings, J.M., Choudhury, N., Chaplot, S.L., Rao, K.R., 1991. Phonon dispersion relation in fayalite, Fe2SiO4. *Physica B: Condensed Matter* 174, 83–86. doi:10.1016/0921-4526(91)90582-Y

Gillet, P.F.T., 1991. High-Temperature Thermodynamic Properties of Forsterite. *JOURNAL OF GEOPHYSICAL RESEARCH* 96816, 805–11.

Gori, C., Tribaudino, M., Mantovani, L., Delmonte, D., Mezzadri, F., Gilioli, E., Calestani, G., 2015. Ca-Zn solid solutions in *C* 2/ *c* pyroxenes: Synthesis, crystal structure, and implications for Zn geochemistry. *American Mineralogist* 100, 2209–2218. doi:10.2138/am-2015-5243

Hamilton, V.E., 2000. Thermal infrared emission spectroscopy of the pyroxene mineral series. *Journal of Geophysical Research* 105, 9701. doi:10.1029/1999JE001112

Hamilton, V.E., 2010. Thermal infrared (vibrational) spectroscopy of Mg-Fe olivines: A review and applications to determining the composition of planetary surfaces. *Chemie der Erde - Geochemistry* 70, 7–33. doi:10.1016/j.chemer.2009.12.005

Hapke, B., 1993. Theory of reflectance and emittance spectroscopy. Cambridge University Press.

Hazen, R.M., 1976. Effects of temperature and pressure on the crystal structure of forsterite. *American Mineralogist* 61, 1280–1293.

Helbert, J., Maturilli, A., 2009. The emissivity of a fine-grained labradorite sample at typical Mercury dayside temperatures, Earth and Planetary Science Letters. doi:10.1016/j.epsl.2009.02.031

Helbert, J., Nestola, F., Ferrari, S., Maturilli, A., Massironi, M., Redhammer, G.J., Capria, M.T., Carli, C., Capaccioni, F., Bruno, M., 2013. Olivine thermal emissivity under extreme temperature ranges: Implication for Mercury surface. *Earth and Planetary Science Letters* 371–372, 252–257. doi:10.1016/j.epsl.2013.03.038

Hiesinger, H., Helbert, J., 2010. The Mercury Radiometer and Thermal Infrared Spectrometer (MERTIS) for the BepiColombo mission. *Planetary and Space Science* 58, 144–165. doi:10.1016/j.pss.2008.09.019

Hofmeister, A.M., 1987. Single-crystal absorption and reflection infrared spectroscopy of forsterite and fayalite. *Physics and Chemistry of Minerals* 14, 499–513. doi:10.1007/BF00308285

Hofmeister, A.M., 1997. Infrared reflectance spectra of fayalite, and absorption datafrom assorted olivines, including pressure and isotope effects. *Physics and Chemistry of Minerals* 24, 535–546. doi:10.1007/s002690050069

Hohler, V., Funck, E., 1973. Schwingungsspektren von Kristallen mit Olivin-Struktur / Vibrational Spectra of Crystals with Olivine Structure. *Zeitschrift für Naturforschung B* 28, 125–139. doi:10.1515/znb-1973-3-406

Huang, E., Chen, C.H., Huang, T., Lin, E.H., Xu, J., 2000. Raman spectroscopic characteristics of Mg-Fe-Ca pyroxenes. *American Mineralogist* 85, 473–479. doi:10.2138/am-2000-0408

Huang, E., Chen, C.H., Huang, T., Lin, E.H., Xu, J.A., 2000. Raman spectroscopic characteristics of Mg-Fe-Ca pyroxenes. *American Mineralogist* 85, 473–479.

Iishi, K., 1978. Lattice dynamics of forsterite. *American Mineralogist*.

Jackson, J.M., Palko, J.W., Andrault, D., Sinogeikin, S.V., Lakshtanov, D.L., Wang, J., Bass, J.D., Zha, C.-S., 2003. Thermal expansion of natural orthoenstatite to 1473 K. *European Journal of Mineralogy* 15, 469–473. doi:10.1127/0935-1221/2003/0015-0469

Jäger, C., Molster, F. J., Dorschner, J., Henning, T., Mutschke, H., & Waters, L. B. F. M. (1998). Steps toward interstellar silicate mineralogy. IV. The crystalline revolution. *Astronomy and Astrophysics*, *339*, 904-916.

Kieffer, S.W., 1979. Thermodynamics and lattice vibrations of minerals: 1. Mineral heat capacities and their relationships to simple lattice vibrational models. *Reviews of Geophysics* 17, 1. doi:10.1029/RG017i001p00001

Koike, C., Chihara, H., Tsuchiyama, A., Suto, H., Sogawa, H., Okuda, H., 2003. Compositional dependence of infrared absorption spectra of crystalline silicate. *Astronomy and Astrophysics* 399, 1101–1107. doi:10.1051/0004-6361:20021831

Koike, C., Mutschke, H., Suto, H., Naoi, T., Chihara, H., Henning, T., Jäger, C., Tsuchiyama, A., Dorschner, J., Okuda, H., 2006. Temperature effects on the mid-and far-infrared spectra of olivine particles. *Astronomy and Astrophysics* 449, 583–596. doi:10.1051/0004-6361:20053256

Kolesov, B.A., Geiger, C.A., 2004. A Raman spectroscopic study of Fe-Mg olivines. *Physics and Chemistry of Minerals* 31, 142–154. doi:10.1007/s00269-003-0370-y

Kudoh, Y., Takéuchi, Y., 1985. The crystal structure of forsterite Mg_2SiO_4 under high pressure up to 149 kb. *Zeitschrift für Kristallographie*.

Lane, M.D., Glotch, T.D., Dyar, M.D., Pieters, C.M., Klima, R., Hiroi, T., Bishop, J.L., Sunshine, J., 2011. Midinfrared spectroscopy of synthetic olivines: Thermal emission, specular and diffuse reflectance, and attenuated total reflectance studies of forsterite to fayalite. *Journal of Geophysical Research E: Planets* 116, 1–20. doi:10.1029/2010JE003588

Lee, C.T., Yang, W.T., Parr, R.G., 1988. DEVELOPMENT OF THE COLLE-SALVETTI CORRELATION-ENERGY FORMULA INTO A FUNCTIONAL OF THE ELECTRON-DENSITY. *Physical Review B* 37, 785–789. doi:10.1103/PhysRevB.37.785

Li, L., Wentzcovitch, R.M., Weidner, D.J., Da Silva, C.R.S., 2007. Vibrational and thermodynamic properties of forsterite at mantle conditions. *Journal of Geophysical Research: Solid Earth* 112, 6–13. doi:10.1029/2006JB004546

Lin, C.-C., 2004. Pressure-induced polymorphism in enstatite (MgSiO3) at room temperature: clinoenstatite and orthoenstatite. *Journal of Physics and Chemistry of Solids* 65, 913–921. doi:10.1016/j.jpcs.2003.09.028

Liu, L.-G., Mernagh, T.P., 1993. Raman spectra of forsterite and fayalite at high pressures and room temperature. *High Pressure Research* 11, 241–256. doi:10.1080/08957959308203152

Mantovani, L., Tribaudino, M., Aliatis, I., Lambruschi, E., Lottici, P.P., Bersani, D., 2015. Raman spectroscopy of CaCoSi2O6–Co2Si2O6 clinopyroxenes. *Physics and Chemistry of Minerals* 42, 179–189. doi:10.1007/s00269-014-0707-8

Mantovani, L., Tribaudino, M., Bertoni, G., 2014. Solid solutions and phase transitions in (Ca, M2+) M2+ Si2O6 pyroxenes (M2+= Co, Fe, Mg). *American* 99, 704–711. doi:10.2138/am.2014.4684

Mantovani, L., Tribaudino, M., Mezzadri, F., Calestani, G., Bromiley, G., 2013. The structure of (Ca,Co)CoSi2O6 pyroxenes and the Ca-M2+ substitution in (Ca,M2+)M2+Si2O6 pyroxenes (M2+ = Co, Fe, Mg). *American Mineralogist* 98, 1241–1252. doi:10.2138/am.2013.4373

Maturilli, A., Helbert, J., D'amore, M., Ferrari, S., 2015. Experimental Verification of Validity for Kirchhoff's Law (E= 1-R) in Vacuum and Purged Air. *Lunar and Planetary Science*.

Maturilli, A., Helbert, J., Ferrari, S., 2016. Characterization of asteroid analogues by means of emission and reflectance spectroscopy in the 1-to 100-µm spectral range. *Earth, Planets*.

Maturilli, A., Helbert, J., Moroz, L., 2008. The Berlin emissivity database (BED). *Planetary and Space Science* 56, 420–425. doi:10.1016/j.pss.2007.11.015

Maturilli, A., Helbert, J., Witzke, A., Moroz, L., 2006. Emissivity measurements of analogue materials for the interpretation of data from PFS on Mars Express and MERTIS on Bepi-Colombo. *Planetary and Space Science* 54, 1057–1064. doi:10.1016/j.pss.2005.12.021

McKeown, D.A., Bell, M.I., Caracas, R., 2010. Theoretical determination of the Raman spectra of single-crystal forsterite (Mg2SiO4). *American Mineralogist* 95.

McMillan, P., Piriou, B., 1983. Raman spectroscopy of calcium aluminate glasses and crystals. *Journal of Non-Crystalline Solids* 55, 221–242. doi:10.1016/0022-3093(83)90672-5

Ngel, R.O.S.S.J.A., Ackson, J.E.M.J., 2002. Elasticity and equation of state of orthoenstatite , MgSiO 3. *American Mineralogist* 87, 558–561.

Nicodemus, F., 1965. Directional reflectance and emissivity of an opaque surface. *Applied optics*.

Noel, Y., Catti, M., D'Arco, P., Dovesi, R., 2006. The vibrational frequencies of forsterite Mg2SiO4: An all-electron ab initio study with the CRYSTAL code. *Physics and Chemistry of Minerals* 33, 383–393. doi:10.1007/s00269-006-0085-y

Oganov, A.R., Dorogokupets, P.I., 2004. Intrinsic anharmonicity in equations of state and thermodynamics of solids. *Journal of Physics: Condensed Matter* 16, 1351–1360. doi:10.1088/0953-8984/16/8/018

Ottonello, G., Civalleri, B., Ganguly, J., Perger, W.F., Belmonte, D., Vetuschi Zuccolini, M., 2010. Thermo-chemical and thermo-physical properties of the high-pressure phase anhydrous B (Mg14Si5O24): An ab-initio all-electron investigation. *American Mineralogist* 95, 563–573. doi:10.2138/am.2010.3368

Ottonello, G., Civalleri, B., Ganguly, J., Vetuschi Zuccolini, M., Noel, Y., 2009. Thermophysical properties of the α-β-γ polymorphs of Mg2SiO4: A computational study. *Physics and Chemistry of Minerals* 36, 87–106. doi:10.1007/s00269-008-0260-4

Ottonello, G., Vetuschi Zuccolini, M., 2008. The iron-isotope fractionation dictated by the carboxylic functional: An ab-initio investigation. *Geochimica et Cosmochimica Acta* 72, 5920–5934. doi:10.1016/j.gca.2008.09.027

Paques-Ledent, M.T., Tarte, P., 1973. Vibrational studies of olivine-type compounds—I. The i.r. and Raman spectra of the isotopic species of Mg2SiO4. *Spectrochimica Acta Part A: Molecular Spectroscopy* 29, 1007–1016. doi:10.1016/0584-8539(73)80140-0

Pascale, F., Zicovich-Wilson, C.M., López Gejo, F., Civalleri, B., Orlando, R., Dovesi, R., 2004. The calculation of the vibrational frequencies of crystalline compounds and its implementation in the CRYSTAL code. *Journal of Computational Chemistry* 25, 888–897. doi:10.1002/jcc.20019

Pierre, M.D.E.L.A., Orlando, R., Maschio, L., Doll, K., Ugliengo, P., Dovesi, R., 2011. Performance of Six Functionals in the Simulation of Vibrational and Dielectric Properties of Crystalline Compounds . The Case of Forsterite Mg 2 SiO 4. *Journal of Computational Chemistry* 7–11. doi:10.1002/jcc

Piriou, B., McMillan, P., 1983. The high-frequency vibrational spectra of vitreous and crystalline orthosilicates. *American Mineralogist* 68.

Prencipe, M., 2012. Simulation of vibrational spectra of crystals by ab initio calculations: An invaluable aid in the assignment and interpretation of the Raman signals. the case of jadeite (NaAlSi 2O 6). *Journal of Raman Spectroscopy* 43, 1567–1569. doi:10.1002/jrs.4040

Prencipe, M., Mantovani, L., Tribaudino, M., Bersani, D., Lottici, P.P., 2012. The Raman spectrum of diopside: a comparison between ab initio calculated and experimentally measured frequencies. *European Journal of Mineralogy* 24, 457–464. doi:10.1127/0935-1221/2012/0024-2178

Prencipe, M., Maschio, L., Kirtman, B., Salustro, S., Erba, A., Dovesi, R., 2014. Raman spectrum of NaAlSi2O6 jadeite. A quantum mechanical simulation. *Journal of Raman Spectroscopy* 45, 703–709. doi:10.1002/jrs.4519

Prencipe, M., Scanavino, I., Nestola, F., Merlini, M., 2011. High-pressure thermo-elastic properties of beryl (Al4Be6Si12O36) from ab initio calculations, and observations about the source of thermal expansion. *Physics and Chemistry*.

Price, G.D., Gillet, P., Reynard, B., 1992. Thermodynamic And Anharmonic Properties Of Forsterite, Alpha-Mg2Sio4 - Computer Modeling Versus High-Pressure And High-Temperature Measurements. *Journal Of Geophysical Research-Solid Earth* 97, 19791–19801.

Prosandeev, S.A., Waghmare, U., Levin, I., Maslar, J., 2005. First-order Raman spectra of A B 1 ⁄ 2 ′ B 1 ⁄ 2 ″ O 3 double perovskites. *Physical Review B* 71, 214307. doi:10.1103/PhysRevB.71.214307

Rao, K., Chaplot, S., Choudhury, N., Ghose, S., 1988. Lattice dynamics and inelastic neutron scattering from forsterite, Mg2SiO4: Phonon dispersion relation, density of states and specific heat. *Physics and chemistry of*.

Reynard, B., Bass, J.D., Jackson, J.M., 2008. Rapid identification of steatite–enstatite polymorphs at various temperatures. *Journal of the European Ceramic Society* 28, 2459–2462. doi:10.1016/j.jeurceramsoc.2008.03.009

ROSSM, N., Reynard, B., 1999. The effect of iron on the Plxlc to Cllc transition in (Mg, Fe) Si03 clinopyroxenes. *Eur. J. Mineral*.

Salisbury, J., D'Aria, D., Jarosewich, E., 1991. Midinfrared (2.5–13.5 μm) reflectance spectra of powdered stony meteorites. *Icarus*.

Salisbury, J.W., Walter, L.S., Vergo, N., 1987. Mid-infrared (2.1-25 um) spectra of minerals; first edition. *Open-File Report*.

Scanavino, I., Prencipe, M., 2013. Ab-initio determination of high-pressure and high-temperature thermoelastic and thermodynamic properties of low-spin (Mg1–xFex) O ferropericlase with x in the. *American Mineralogist* 98, 1270–1278.

Schmidt, W., Brotzeller, C., Geick, R., Schweiss, P., Treutmann, W., 1992. Magnon-phonon coupling in Fe2SiO4. *Journal of Magnetism and Magnetic Materials* 104, 1049–1050. doi:10.1016/0304-8853(92)90484-6

Servoin, J.L., Piriou, B., 1973. Infrared Reflectivity and Raman Scattering of Mg2SiO4 Single Crystal. *Physica Status Solidi B* 55, 677–686. doi:10.1002/pssb.2220550224

Shaw, D.M., Tse, J.S., 2007. Vibrational dynamics in H+-substituted forsterite: A first-principles molecular dynamics study. *American Mineralogist* 92, 1593–1600. doi:10.2138/am.2007.2433

Sprague, A., Hanna, K., Kozlowski, R., 2009. Spectral emissivity measurements of Mercury's surface indicate Mg-and Ca-rich mineralogy, K-spar, Na-rich plagioclase, rutile, with possible perovskite, and garnet. *Planetary and Space*.

Sprague, A., Hanna, K.D., 2008. Mercury: Mg-rich mineralogy with K-spar and garnet. *Lunar and Planetary*.

Sprague, A., Kozlowski, R., Witteborn, F., 1994. Mercury: Evidence for Anorthosite and Basalt from Mid-infrared (7.3-13.5 μm) Spectroscopy. *Icarus*.

Sprague, A., Roush, T., 1998. Comparison of laboratory emission spectra with Mercury telescopic data. *Icarus*.

Stalder, R., Kronz, A., Schmidt, B.C., 2009. Raman spectroscopy of synthetic (Mg,Fe)SiO3 single crystals. An analytical tool for natural orthopyroxenes. *European Journal of Mineralogy* 21, 27–32. doi:1

Stangarone, C., Tribaudino, M., Prencipe, M., Lottici, P.P., 2016. Raman modes in Pbca enstatite (Mg 2 Si 2 O 6): an assignment by quantum mechanical calculation to interpret experimental results. *Journal of Raman Spectroscopy* 47, 1247–1258. doi:10.1002/jrs.4942

Stidham, H.D., Bates, J.B., Finch, C.B., 1976. Vibrational spectra of synthetic single crystal tephroite, Mn2SiO4. *The Journal of Physical Chemistry* 80, 1226–1234. doi:10.1021/j100552a023

Stimpfl, M., Ganguly, J., Molin, G., 2005. Kinetics of Fe2+–Mg order–disorder in orthopyroxene: experimental studies and applications to cooling rates of rocks. *Contributions to Mineralogy and Petrology*.

Strom, R., Sprague, A., 2003. Book Review: EXPLORING MERCURY: THE IRON PLANET/Springer, 2003/2004. *Astronomy and Geophysics*.

TARANTINO, S.C., BALLARAN, T.B., CARPENTER, M.A., DOMENEGHETTI, M.C., TAZZOLI, V., 2002. Mixing properties of the enstatite-ferrosilite solid solution. *European Journal of Mineralogy* 14.

Tarantino, S.C., Domeneghetti, M.C., Carpenter, M.A., Shaw, C.J.S., Tazzoli, V., 2002. Mixing properties of the enstatite-ferrosilite solid solution: I. A macroscopic perspective. *European Journal of Mineralogy* 14, 525–536. doi:10.1127/0935-1221/2002/0014-0525

Tribaudino, M., Talarico, F., 1992. Orthopyroxenes from granulite rocks of the Wilson Terrane (Victoria Land, Antarctica): crystal chemistry and cooling history. *European Journal of Mineralogy*.

Ulmer, P., Stalder, R., 2001. The Mg (Fe) SiO3 orthoenstatite-clinoenstatite transitions at high pressures and temperatures determined by Raman-spectroscopy on quenched samples. *American Mineralogist* 86, 1267–1274.

Ungureanu, C.G., Prencipe, M., Cossio, R., 2010. Ab initio quantum-mechanical calculation of CaCO3 aragonite at high pressure: thermodynamic properties and comparison with experimental data. *European Journal of Mineralogy* 22.

Veithen, M., Gonze, X., Ghosez, P., 2005. Nonlinear optical susceptibilities, Raman efficiencies, and electro-optic tensors from first-principles density functional perturbation theory. *Physical Review B* 71, 125107. doi:10.1103/PhysRevB.71.125107

WALKER, A.M., DEMOUCHY, S., WRIGHT, K., 2007. Computer modelling of the energies and vibrational properties of hydroxyl groups in α- and β-Mg2SiO4. *European Journal of Mineralogy* 18.

Wang, A., Jolliff, B.L., Haskin, L.A., Kuebler, K.E., Viskupic, K.M., 2001. Characterization and comparison of structural and compositional features of planetary quadrilateral pyroxenes by Raman spectroscopy

Wang, A., Jolliff, B.L., Haskin, L.A., Kuebler, K.E., Viskupic, K.M., 2001. Characterization and comparison of structural and compositional features of planetary quadrilateral pyroxenes by Raman spectroscopy. *American Mineralogist* 86, 790–806. doi:10.2138/am-2001-0703

Wang, A., Kuebler, K., Jolliff, B., Haskin, L.A., 2004. Mineralogy of a Martian meteorite as determined by Raman spectroscopy. *Journal of Raman Spectroscopy* 35, 504–514. doi:10.1002/jrs.1175

Wang, L., Moon, N., Zhang, Y., Dunham, W.R., Essene, E.J., 2005. Fe-Mg order-disorder in orthopyroxenes. *Geochimica et Cosmochimica Acta* 69, 5777–5788. doi:10.1016/j.gca.2005.08.011

Warell, J., Sprague, A., Kozlowski, R., Rothery, D.A., Lewis, N., Helbert, J., Cloutis, E., 2010. Constraints on Mercury's surface composition from MESSENGER and ground-based spectroscopy. *Icarus* 209, 138–163. doi:10.1016/j.icarus.2010.04.008

Weber, I., Böttger, U., Pavlov, S.G., Jessberger, E.K., Hübers, H.W., 2014. Mineralogical and Raman spectroscopy studies of natural olivines exposed to different planetary environments. *Planetary and Space Science* 104, 163–172. doi:10.1016/j.pss.2014.08.016

Wu, Z., Cohen, R.E., 2005. Generalized Gradient Approximation Made More Accurate for Solids. *Phys. Rev. B* 73, 235116. doi:10.1103/PhysRevB.73.235116

Yang, H., Ghose, S., 1995. High Temperature Single Crystal X-ray Diffraction Studies of the Ortho-Proto Phase Transition in Enstatite, Mg2Si206 at 1360 K. *Physics and Chemistry of Minerals* 22, 300–310

Yu, Y.G., Wentzcovitch, R.M., 2006. Density functional study of vibrational and thermodynamic properties of ringwoodite. *Journal of Geophysical Research: Solid Earth* 111, n/a-n/a. doi:10.1029/2006JB004282

Zeidler, S., Mutschke, H., Posch, T., 2015. Temperature-Dependent Infrared Optical Constants of Olivine and Enstatite. *The Astrophysical Journal* 798, 125. doi:10.1088/0004-637X/798/2/125

Zhang, J.S., Reynard, B., Montagnac, G., Bass, J.D., 2014. Pressure-induced Pbca–P21/c phase transition of natural orthoenstatite: The effect of high temperature and its geophysical implications. *Physics of the Earth and Planetary Interiors* 228, 150–159. doi:10.1016/j.pepi.2013.09.008

Zhang, J.S., Reynard, B., Montagnac, G., Wang, R.C., Bass, J.D., 2013. Pressure-induced Pbca-P21/c phase transition of natural orthoenstatite: Compositional effect and its geophysical implications. *American Mineralogist* 98, 986–992. doi:10.2138/am.2013.4345

Zhang, L., Ahsbahs, H., Hafner, S.S., Kutoglu, A., 1997. Single-crystal compression and crystal structure of clinopyroxene up to 10 GPa. *American Mineralogist* 82, 245–258. doi:10.2138/am-1997-3-402

Zicovich-Wilson, C.M., Torres, F.J., Pascale, F., Valenzano, L., Orlando, R., Dovesi, R., 2008. *Ab initio* simulation of the IR spectra of pyrope, grossular, and andradite. *Journal of Computational Chemistry* 29, 2268–2278. doi:10.1002/jcc.20993

Zucker, R., Shim, S.-H., 2009. In situ Raman spectroscopy of MgSiO3 enstatite up to 1550 K. *American Mineralogist* 94, 1638–1646. doi:10.2138/am.2009.3210